Mauro António Moreira Guerra

M. Sc. in Physics Engineering

Electron Impact Ionization Cross Sections and Analysis of X-ray Spectra

A thesis submitted for the degree of
Ph. D. in Physics

Supervisor: Professor José Paulo Moreira dos Santos,
Associate Professor with Aggregation,
Physics Department

Examining Committee:

Chair: Dean of the New University of Lisbon
External Examiner: Professor José Manuel Pires Marques
Internal Examiner: Professor Maria Adelaide de Almeida Pedro de Jesus

Other Members: Professor Fernando António de Freitas Costa Parente
Doctor Paul Indelicato
Professor Joaquim Marques Ferreira dos Santos
Professor Ana Maria Almeida e Costa

FACULDADE DE
CIÊNCIAS E TECNOLOGIA
UNIVERSIDADE NOVA DE LISBOA

December 2012

Electron Impact ionization Cross Sections and Analysis of X-ray Spectra

Mauro António Moreira Guerra

December 2012

Acknowledgements

This work could not have been done without the greatly appreciated effort of several people, the first of which is my supervisor Prof. José Paulo dos Santos, who constantly encouraged and challenged me throughout my academic program, never accepting less than my best efforts. Thank you.

To Doctor Paul Indelicato I express my sincere gratitude for welcoming me at is group of the LKB in Paris. His scientific skills as well as his human qualities will forever be an example. I would also like to acknowledge Doctor Csilla Szabo for the immense help in reviewing my thesis and for making my stay in Paris as enjoyable as possible. To Dr. Alexandre Vallette and Dr. Martino Trassinelli for, not only, the great physics discussions but also for being my rock climbing partners in France. To the rest of the LKB group with whom I had the pleasure of doing science, Dr. Alexandre Gumberidze, Dr. Eric Olivier Le-Bigot and Dr. Stephane Boucard.

Aos meus colegas de curso que se tornaram em grandes amigos, Doutor Rui Pinto pela sua maneira de ver o mundo e pelos excelentes conselhos, Doutora Diana Guimarães por me mostrar que a força de vontade supera qualquer obstáculo, ao Doutor Pedro Amaro pelas excelentes discussões científicas e pela ajuda ao longo deste trabalho. Ao Doutor Rodrigo Antunes pela maneira feliz como me faz olhar para a vida e ao Diogo pelas excelentes discussões filosóficas que me fazem muitas vezes rever as minhas prioridades.

Por último, embora não com menos peso, as pessoas mais importantes na minha vida pessoal, aos meus pais, sem os quais nunca teria conhecido o doce sabor da vida e de tudo o que contém. Ao António e à Graça por me terem sempre tratado como um filho e aos meus irmãos por todo o carinho que me dão. Principalmente a ti, Mafalda, por todos os momentos felizes que já passámos e pelos que ainda virão.

To everyone who directly or indirectly contributed to the conclusion of this thesis, I give a heartfelt "thank you".

Abstract

Knowledge of ionization and excitation cross sections is of fundamental importance for understanding collision-dynamics and electron-atom interactions, as well as in several applied fields such as radiation science, astrophysics and plasma physics. These areas of study need enormous and continuous quantities of data, within a certain accuracy level, for different targets over a wide range of energy values. Plasma diagnosis is a particular field in which analytical expressions for electron impact ionization cross sections are welcome.

In the first part of this thesis, we have derived new expressions for the analytical calculation of ionization cross sections by electron impact based on the binary encounter Bethe (BEB) model, valid from ionization threshold up to relativistic energies. The new modified binary-encounter Bethe model (MBEB), and its relativistic counterpart (MRBEB) expressions are simpler than the BEB (nonrelativistic and relativistic) expressions because they require only one atomic parameter, namely the binding energy of the electrons to be ionized, and use only one scaling term for the ionization of all sub-shells of neutral atoms and ions.

The new models are used to calculate the K-, L- and M-shell ionization cross sections by electron impact for several atoms with Z from 6 to 83, as well as direct electron impact ionization cross sections for several ionization stages of Kr, Ar and Fe. Excitation-autoionization cross sections were evaluated using the First Order Many Body Theory (FOMBT) for Kr^+, Kr^{5+}, Kr^{6+}, Kr^{10+}, Kr^{15+} and Kr^{17+}. Our results were compared to configuration-averaged distorted-wave (CADW) calculations, the widely used Lotz formula and available experimental results. Direct ionization cross sections for the Ar and Fe isonuclear series were also calculated with the goal of assessing the versatility of the MRBEB model for computing electron impact ionization cross sections of species that are usually present in plasmas of any type.

In the second part of this thesis, Ar plasmas, generated in electron-cyclotron-resonance ion-sources (ECRIS), are used to perform *state-of-the-art* highly charged ions X-ray transition energy measurements with a double-crystal-spectrometer (DCS). Such a spectrometer, used for the first time on a highly charged ion transition, provides absolute (reference-free) measurements in the X-ray domain. From this measurements we were able to extract useful information about the plasma conditions inside the ECRIS chamber, such as the ionic temperatures, charge-state-distribution and electronic densities.

The measurement of the relativistic magnetic dipole transition, $1s2s\ ^3S_1 \rightarrow 1s^2\ ^1S_0$, in He-like Ar has been performed and a transition energy of 3104.1605(78) eV was found, which corresponds to an accuracy of 2.5 ppm. This value is the most accurate, reference-free measurement done for such a transition and is in good agreement with recent QED predictions. From the DCS measurements, we were also able to probe the natural width of several lines. The natural width of the diagram line $1s2p\ ^1P_1 \rightarrow 1s^2\ ^1S_0$ is found to be 79.08 ± 10.40 meV which corroborates the theoretical value of 70.4 meV.

The charge state distribution of the Ar ions inside the plasma has been calculated with the use of the electron impact ionization cross sections calculated in the first part of the thesis

with our MRBEB model. For this purpose, a wide scan containing several transitions of the highly charged Ar ions has been done, and an iterative process using balance equations of the plasma species was used to obtain the charge-state-distribution.

Resumo

O conhecimento dos valores das secções eficazes de ionização e excitação é de uma importância fundamental no estudo de colisões atómicas e interacções electrão-átomo, bem como em diversos campos de física aplicada tal como ciência da radiação, astrofísica e física dos plasmas. Estas áreas de estudo necessitam de quantidades enormes e num espectro contínuo de dados de secções eficazes, dentro de um certo nível de precisão, para diversos alvos dentro de uma gama de energias bastante alargada. O diagnóstico de plasmas é um campo particular em que expressões analíticas para o cálculo de secções eficazes de ionização por impacto electrónico são bem recebidas.

Na primeira parte desta tese, foram derivadas novas expressões para o cálculo analítico de secções eficazes de ionização por impacto electrónico, baseadas no modelo do encontro binário de Bethe (BEB), que são válidas desde o limiar de ionização até energias relativistas. O novo modelo do encontro binário de Bethe modificado (MBEB) e a sua versão relativista (MRBEB) utiliza expressões que são mais simples do que as do modelo BEB (relativista e não-relativista), porque requerem apenas um parâmetro atómico, nomeadamente a energia de ligação dos electrões que serão ionizados, e utilizam apenas um factor de escala para a ionização de qualquer camada electrónica de átomos neutros ou iões.

Os novos modelos foram usados para calcular secções eficazes de ionização para as camadas K, L e M para diversos átomos com número atómico Z entre 6 e 83, bem como secções eficazes de ionização directa para diversos estados de carga de iões de Kr, Ar e Fe. Secções eficazes de excitação-autoionização foram calculadas usando a teoria de muitos corpos em primeira ordem (FOMBT) para os iões Kr^+, Kr^{5+}, Kr^{6+}, Kr^{10+}, $Kr^{15}+$ e Kr^{17+}. Os nossos resultados foram comparados com cálculos de configuração média de ondas distorcidas (CADW), com a recorrentemente utilizada fórmula de Lotz e resultados experimentais disponíveis. Secções eficazes de ionização directa para as séries isonucleares de Ar e Fe também foram calculadas com o objectivo de estudar a versatilidade do modelo MRBEB no cálculo de secções eficazes de ionização de espécies que usualmente estão presentes em plasmas de todos os tipos.

Na segunda parte desta tese, plasmas de argon gerados em fontes de iões de ressonância de electrões em ciclotrão (ECRIS), foram usados para medir energias de transição em iões altamente carregados com um espectrómetro *estado-da-arte* de duplo cristal (DCS). Este espectrómetro, usado pela primeira vez numa transição de um ião altamente carregado, providencia medidas absolutas (sem referência a outras linhas) no domínio da radiação X. Destas medições conseguímos extrair informação útil acerca das condições do plasma no interior da câmara do ECRIS, tal como a temperatura dos iões, a distribuição de estados de carga e a densidade electrónica.

A medição da transição dipolar magnética relativista, $1s2s\ ^3S_1 \rightarrow 1s^2\ ^1S_0$, em iões de argon heliumóides foi efectuada e uma energia de transição de 3104.1605(78) eV foi obtida, o que corresponde a uma precisão de 2.5 ppm. Este valor é o mais preciso, sem referência a outras linhas, para uma transição deste tipo e está de acordo com cálculos de electrodinâmica quântica (QED) recentes. Das medições com o DCS conseguímos também sondar a largura

intrínseca de várias linhas. A largura intrínseca da linha $1s2p\ ^1S_1 \to 1s^2\ ^1S_0$ obtida foi de 79.08±10.40 meV o que está de acordo com o valor teórico de 70.4 meV.

A distribuição de estados de carga dos iões de Ar dentro do plasma foi calculada com o uso das secções eficazes de ionização obtidas na primeira parte da tese com o modelo MRBEB. Para este propósito, um espectro largo, contendo várias transições dos iões de argon altamente carregados, foi obtido experimentalmente, e através de um processo iterativo, usando equações de balanço de espécies no plasma, a distribuição de estados de carga do plasma foi obtida.

Palavras-chave: *impacto electrónico*; *ionização*; *secções eficazes*; *raios-x*; *transições*; *iões altamente carregados*.

List of Publications and Manuscripts

The work performed in this thesis gave origin to the following list of published articles and manuscripts for publication.

- M. Guerra, F. Parente and J. P. Santos, *Electron impact ionization of atomic target inner-shells*, Journal of Physics: Conference Series, Volume **194**, Number 4, p.042047, (2009),

- J. P. Santos, M. Guerra and F. Parente, *New expression for the K-shell ionization*, Journal of Physics: Conference Series, **388**, 042047, (2012),

- P. Amaro, S. Schlesser, M. Guerra, E. O. Le Bigot, J. M. Isac, P. Travers, J. P. Santos, C. I. Szabo, A. Gumberidze and P. Indelicato, *Absolute measurement of the "relativistic M1" transition energy in heliumlike argon.* Physical Review Letters **109**, 043005, (2012).

- M. Guerra, F. Parente, P. Indelicato and J. P. Santos, *Modified binary encounter Bethe model for electron-impact ionization*, International Journal of Mass Spectrometry, Volume **313**, Number 1, p.1-7, (2012)

- C. I. Szabo, P. Indelicato, E.-O. LeBigot, A. Vallette, P. Amaro, M. Guerra and A. Gumberidze, *Progress on Precision Measurements of Inner Shell Transitions in Highly Charged Ions at an ECR Ion Source*, Proceedings of the 17th International Conference on Atomic Processes in Plasmas, 19-22 July 2011, Queen's University, Belfast, AIP Conference Proceedings **1438**, 236-239 (2012)

- P. Amaro, C. I. Szabo, S. Schlesser, A. Gumberidze, E. G. Kessler, Jr, A. Henins, E.O. Le Bigot, M. Trassinelli, Jean-Michel Isac, Pascal Travers, M. Guerra, J. P. Santos and Paul Indelicato, *A vacuum double-crystal spectrometer for reference-free highly charged ions X-ray spectroscopy*, Rad. Phys. Chem., *Accepted* (2012) arXiv:1205.4520v1 [physics.atom-ph]

- M. Guerra, F. Parente and J. P. Santos, *Electron impact ionization cross sections of several ionization stages of Kr, Ar and Fe*, International Journal of Mass Spectrometry, *Submitted* (2012).

- C. I. Szabo, S. Schlesser, P. Amaro, M. Guerra, E.-O.L. Bigot, J.-P. Santos, A. Gumberidze and P. Indelicato, *Measurement of the Natural Width of Transitions in He-like and Be-like Argon*, Phys. Rev. A., *In Preparation*, (2012).

- M. Guerra, P. Amaro, C. I. Szabo, A. Gumberidze, P. Indelicato and J. P. Santos, *Analysis of the charge state distribution in an ECRIS Ar plasma using high-resolution x-ray spectra*, Journal of Physics B, *In Press*, (2012).

Contents

Contents

List of Figures

List of Tables

List of Tables

List of Acronyms

CSD Charge State Distribution.

ECRIS Electron-Cyclotron-Resonance Ion-Source.

EIICS Electron-Impact Ionization Cross Sections.

BEB Binary-Encounter Bethe Model.

RBEB Relativistic Binary-Encounter Bethe Model.

XRF X-ray Fluorescence.

AES Auger Electron Spectroscopy.

EELS Electron Energy Loss Spectroscopy.

EPMA Electron Probe Microanalysis.

PWBA Plane-Wave Born Approximation.

CCC Convergent Close-Coupling Method.

BA Born Approximation.

BeA Bethe Approximation.

CBA Coulomb-Born Approximation.

BAE Born Approximation with Exchange.

SA Sudden Approximation.

DWA Distorted Wave Approximation.

CCA Close-Coupling Approximation.

PsA Pseudostate Approximation.

DCS Double Crystal Spectrometer.

QED Quantum Electrodynamics.

SDCS Singly Differential Cross Section

TICS Total Ionization Cross Section

BE Binary-Encounter Model.

BED Binary-Encounter Dipole Model.

BEQ Binary-Encounter Q Model.

BEBV Binary-Encounter Bethe-Vriens Model.

RPWBA Relativistic Plane-Wave Born Approximation.

MCDFGME Multiconfiguration Dirac-Fock General Matrix Elements.

MBEB Modified Binary-Encounter Bethe Model.

MRBEB Modified Relativistic Binary-Encounter Bethe Model.

DWBA Distorted Wave Born Approximation.

CADW Configuration-Averaged Distorted Wave.

FOMBT First Order Many-Body Theory.

HS Hydrogenic Scaling Model.

DI Direct Ionization.

EA Excitation-Autoionization.

SIMPA Source d'Ions Multichargés de Paris.

BSQED Bound-State Quantum Electrodynamics.

EBIT Electron Beam Ion Trap.

HCI Highly Charged Ions.

INSP Institut des NanoSciences de Paris.

PSI Paul Scherrer Institute.

FWHM Full Width at Half Maximum.

NIST National Institute of Standards and Technology.

XOP X-ray Oriented Program.

Part I
Introduction and Theory

Introduction

1.1 Goals and Motivation

In the last decades, with the onset of fusion plasma physics, x-ray spectroscopy for plasma diagnostics has been a trendy topic, being thoroughly studied by several groups. One of the main problems in plasma diagnostics is the determination of the ion charge-state distribution (CSD) inside the plasma. The most used method for inferring the CSD is through extracted ion beam currents, but it is not very reliable because the extraction is optimized for a particular charge state and also because the ions are extracted from the plasma edges, so it does not fully represents the CSD inside the plasma. Alternatively, the CSD could be obtained through the analysis of high-resolution x-ray spectra emitted from the plasma [1–4]. Similar processes for optical plasma diagnostics were reviewed in the work of Boffard *et al.* [5].

Theoretical methods for estimating the CSD inside the plasma have been developed by our group in the last decade, based on the work of Douysset *et al.* [6] and Küchler *et al.* [7]. In 2001, a detailed analysis of K x-ray spectra emitted by Ar ions in an electron-cyclotron-resonance ion-source (ECRIS) plasma [8] was performed. That work showed that a correct analysis of these spectra calls for a detailed and careful examination of all excitation and ionization processes that could lead to the detected lines. In 2009 and 2010, an improved method was used to estimate the ion CSD in ECRIS through the analysis of x-ray emitted by Sulphur plasmas, and it was concluded that the role of single and multiple electron impact ionization is very important to reproduce all the features in the experimental x-ray spectra [9]. Also, a more realistic electron energy distribution was used. Since electrons in a ECRIS plasma are far from thermodynamical equilibrium, their energy distribution is highly non-Maxwellian and can be represented by two populations with different temperatures, instead of only one.

The main goal of the first part of this thesis is to obtain an analytical expression, free of adjustable parameters, that can calculate the electron-impact ionization cross sections (EIICS) for all the sub-shells of a wide range of elements of the periodic table in any charge state. Being one of the fundamental ingredients in the analysis of x-ray spectra, it is very important that the accuracy over a wide range of targets, such as inner- and outer-shells of neutral atoms and ions in all of the periodic table, is maintained within a reasonable accuracy range.

The choice for our starting point is a widely used expression, developed by Kim and Rudd [10] in 1994, that successfully combines the binary-encounter theory with the dipole interaction of the Bethe theory for fast incident electrons [11], and meets some of the above mentioned requirements.

The binary encounter Bethe model (BEB) and its relativistic counterpart RBEB; that can be obtained as analytical formulae which require only the incident particle energy (T),

the target particle's binding energy (B) and the target particle's kinetic energy (U); generate direct ionization cross section curves for neutral atoms, which are reliable in intensity ($\pm$ 20%) and shape, for many atomic systems, from the ionization threshold to a few keV in the incident energy [12, 13]. If its relativistic version (RBEB) [14] is considered the energy range stretches to thousands of keV [15] .

1.2   Electron Impact Cross Sections

Knowledge of ionization and excitation cross sections is of fundamental importance for understanding collision-dynamics and electron-atom interactions, as well as in several applied fields such as radiation science, astrophysics, elemental analysis using x-ray fluorescence (XRF), Auger electron spectroscopy (AES), electron energy loss spectroscopy (EELS) and electron probe microanalysis (EPMA), and, as has been explained before, in plasma diagnostics. These areas of study need enormous and continuous quantities of data, within a certain accuracy level, for different targets over a wide range of energy values.

Electron impact ionization and excitation have been actively studied by many research groups since the 1920's. Most of the work produced was based on classical collision theory, and several first principle theories were developed [11, 16–20]. The most important work in the field of electron-atom collision was made by Bethe (1930) who derived the correct form of the ionization cross section shape for high-energy collisions [11] using the plane-wave Born approximation (PWBA). Since then, several empirical and semi-empirical models have been proposed to describe electron impact ionization of atoms and molecules [21–26], and several reviews on them were published [27, 28].

All works can be divided into three types: those based on quantum mechanics, which have a far superior accuracy than their classical counterparts but at the cost of complexity; those based on classical mechanics, which give rise to much simpler expressions at the cost of accuracy; and semi-empirical ones, that are often based in the classical formulations. The simpler quantum mechanical models for electron impact ionization tend to fair better than the classical models for high energies, essentially because of the use of the Born approximation, although for collisions where the momentum transfer is large, the classical expressions seem to be better at describing the ionization. Empirical and semi-empirical models can be very simple to use, but the fact that the experimental cross sections are scarce for some elements and sub-shells does not make it easy to pinpoint the accuracy of such models for the entire range of targets. They are, however, a very good way to get an estimate of the cross sections for a fairly wide range of elements and sub-shells.

With the advance of quantum mechanical computational methods, some very sophisticated *ab initio* theories became available such as the convergent close coupling (CCC) [29, 30], the R-matrix method [31] and exterior complex scaling [32]. These calculations, however, are very time-consuming, limiting the domain of applicability of such models [29, 30, 33, 34].

In the last years, many analytical formulas have been developed to overcome these difficulties, some of them empirical [35–37] and others derived from first principles [10, 14, 38, 39]. Analytical expressions, derived from first principle are still widely used in all the fields of physics described above, even in a era where the large and steady increment in computational power seem to consistently elevate numerical computations.

1.2.1   Overview of the approximations used in atomic collisions

In the last one hundred years, the atomic physics community devoted a lot of effort into the study of particle collisions. Many methods and approximations derived throughout the times are still used in the interpretation of particle interactions. Below we attempt to make a brief overview of the main approximations and methods that are widely used and try establish a

starting point for the work developed in this thesis.

1.2.1.1 The Born approximation

The Born approximation (BA) usually refers to the first Born approximation. In this approximation, the incident and scattered particles are described as plane waves that remain undistorted by the interaction. Only direct ionization is treated, and for electron impact, electron exchange and spin are not taken into account. No coupled equations are involved since the solution to the scattered amplitude is unique. The validity of the first Born approximation remains essentially for high velocity projectiles, but accurate cross sections can only be obtained if good quality wave functions for the stationary states of the of the colliding structures are available.

At low energies, the first Born approximation usually overestimates the scattering cross sections, however it may be used at very low impact energies provided that the interaction energy is too shallow to accommodate a bound state of the interacting system [40].

1.2.1.2 The Bethe approximation (BeA)

In the Bethe theory for the stopping power of fast projectiles [11], a slight modification of the Born approximation was performed, in which Bethe made an additional assumption that the product of the momentum transfer and the range of the interaction is small. In this way, the exponential term in the Born approximation for the scattered amplitude can be expanded, and the following integration carried out term by term.

Doing this leads to a series of terms that can be related to atomic transition moments (electric dipole, quadrupole, etc.). Bethe has shown that the soft collisions take place essentially through the dipole interaction between the incident particle and the target electron [10], so only the first term after integration can be used to account for soft collisions. This method is also called Bethe-Born approximation.

1.2.1.3 The Coulomb-Born approximation (CBA)

The Coulomb-Born approximation (CBA) is useful in describing collisions of electrons and ions with target ions, in which the Coulomb interaction of the projectile with the target nucleus can be important. The Born plane wave are replaced by Coulomb wave functions corresponding to the nuclear charge. For highly charged ions, the long range Coulomb interaction is dominant, and all other interactions may be treated as small perturbations. In this way, it is not expected to hold for collisions between electrons and neutral atoms. Comparing to the Born approximation, we usually get better results in electron-ion scattering with the Coulomb theory than in the Born approximation for electron-neutral scattering.

1.2.1.4 Born approximation with exchange (BAE)

In 1928, the first attempt to include exchange in the Born formalism was made by none other than J. R. Oppenheimer. He made the same basic assumptions as used in the Born approximation, but his method of calculating the exchange amplitude is less satisfactory than the Born method for direct scattering, in the sense that it sometimes leads to incorrect results, mainly because in the Born-Oppenheimer approximation [41] the initial and final states are not orthogonal. This results in the fact that the addition of any constant to the interaction potential gives a non-zero change in the exchange amplitude. The Born approximation tends to excessively overestimate the scattering cross sections.

Later, Bates *et al.*, were able to develop a formulation that was correct to first order and that included the orthogonality between the initial and final states [41].

Another improvement was made by V. I. Ochkur, who suggested that the exchange amplitude should be regarded as an expansion in inverse powers of the impact energy, with the result of only the first term being retained since higher terms would cause the result to diverge at low impact energies. The Ochkur approximation to the exchange integral is a good approximation only at impact energies that are high enough for the integral to be small.

1.2.1.5   The sudden approximation (SA)

The sudden approximation (SA) was introduced by Enrico Fermi in 1936, and describes a many-body scattering problem in terms of two-body amplitudes, that are well known. This method rests on the assumption that, apart from having to determine a velocity distribution of the target electron, it plays no part in the scattering calculation. Another statement of the basic assumption is that the interaction occurs at a much shorter time than the orbital motion period of the target electron, or, in other words, the interaction is sudden. One would, therefore, expect the approximation to hold at energies much higher than the binding energy of the target particle being considered and/or the reduced wavelength of the relative motion of the projectile and target system is much smaller than the mean separation of the constituents of the target atom.

1.2.1.6   The Binary Encounter Approximation (BEA)

In the Binary Encounter Approximation (BEA), the incident and target electron's interaction is treated as a billiard ball-like collision. A straightforward analytical expression for the scattering amplitude in this formalism can be easily derived from first principles. Exchange is included as in the Mott formalism [40, 42] and a velocity distribution for the target electron is assigned, unlike the Mott and Rutherford theories, which are only valid for collisions with free electrons at rest. The close or hard collisions are very well described by this theory as is expected, but the lack of a long range interaction results in soft or distant collisions that deviates from the expected Bethe-Born approximations. The predictions of near threshold cross sections are thus very good but the asymptotic behaviour does not have the correct form. The binary encounter approximation matches most of requirements in our goals, and thus will be our starting point for the construction of a reliable, analytical, parameter-free electron impact ionization model.

1.2.1.7   The distorted wave approximation (DWA)

The distorted wave approximation takes into account the distortion of the incident and scattered waves by the static field of the target. From the calculation of the excitation of an electron in the hydrogen atom, in a time-independent quantum mechanical calculation, one eventually arrives at an asymptotic solution that corresponds to a distorted wave with the asymptotic form of a plane wave and an outgoing spherical wave. The incoming wave is described by a plane wave and the scattered wave is represented by a distorted wave with the asymptotic behaviour of a spherical wave [43]. This approximation provides a very good compromise between computation time and accuracy, although for very high incident energies the size of the matrices involved result in a overcharge of computational resources even for *state of the art* machines.

1.2.1.8   Close-Coupling approximation (CCA)

In the close-coupling approximation, the wave function for the projectile and target system is expanded in terms of a complete set of eigenfunctions ψ_0 of the target Hamiltonian. We assume that the eigenfunctions are known. For a structureless projectile colliding with an

N-electron atom, we write

$$\psi\left(\mathbf{r}_1, \mathbf{r}_2\right) = \sum_{\gamma} F_{\gamma}\left(\mathbf{r}_1\right) \psi_0\left(\gamma, \mathbf{r}_2\right), \tag{1.1}$$

where $\mathbf{r}_1$ represents the spatial and spin coordinates of the the projectile and $\mathbf{r}_2$ the coordinates of the atomic electrons. Any possible combination of the good quantum numbers is represented by γ.

The overall wave function must be antisymmetric, and the functions $F_{\gamma}\left(\mathbf{r}_1\right)$ describe the radial motion of the projectile relative to the target in its various quantum states. The close-coupling approximation allows us to retain only a small number of terms in the wave function expansion [Eq. (1.1)]. The number of terms retained depends on the number of allowed scattering channels. These channels are a function of the number of possible outcomes in a collision: elastic scattering, excitation, dissociation, charge transfer, and so on. The channels are said to be open if they are allowed by conservation laws, otherwise they are considered closed.

The radial part of the scattering wave functions satisfy a set of M (M being the number of channels) integrodifferential equations of the form

$$\left[\frac{d^2}{dr^2} + k_i^2 - \frac{l_i\left(l_i + 1\right)}{r^2} \frac{\hbar^2}{2m_e}\right] F_i\left(r\right) = \sum_{j=1}^{M} V_{ij}\left(r\right) F_j\left(r\right) + \int_0^{\infty} W_{ij}\left(r, r'\right) F_j\left(r'\right) dr',$$

where $V_{ij}\left(r\right)$ is a direct electron-electron plus electron-nucleus potential, and $W_{ij}\left(r, r'\right)$ is the exchange term. The r' refers to the exchanged electron.

These closed-coupling equations can provide accurate cross sections if all of the target states lying close to the initial and final states are included in the expansion [Eq. (1.1)]. The slow convergence of the truncated expansions makes this method intractable at high impact energies, at which more states are available and more angular momenta become important. Also, if we try to use close-coupling to calculate scattering from excited states, the close spacing of the energy levels makes the procedure much more time-consuming. This method is, however, effectively exact in the prediction of the positions and shapes of threshold effects and resonances in low-energy collisions of electrons with ground-state atoms, contrary to the other methods mentioned above. This method is one of the most accurate way of calculating electron impact ionization cross sections, but only very simple systems can be completely studied with this formalism.

1.2.1.9 The Pseudo-state approximation (PsA)

As we have seen, computational difficulties increase rapidly with the number of target eigenfunctions used in the close-coupling expansion; in practice, only a few of bound-states and continuum states are included. One method to overcome this difficult is to include in the wave function expansion some function $\phi_n F_n\left(\mathbf{r}_1\right)$ where ϕ_n is not a target eigenfunction but a function representing an appropriate average of bound and continuum states. These states are thus not real, and for this reason they are called pseudo-states. Although there is no unique way to choose which pseudo-states to be used, some questions of normalization and orthogonality must be addressed. This pseudo-states can in turn introduce fictitious thresholds and resonances, and this artefacts can lead to inaccuracies in computed cross sections.

1.2.1.10 The R-Matrix method

The $\mathbf{R}$ matrix was introduced in nuclear physics by Wigner in 1946 [44, 45] and since has been developed by Burke, Noble and Schneider and subsequently widely used in atomic physics. A very good review can be seen in Ref. [46].

The reactance $\mathbf{R}$ matrix is related to the scattering $\mathbf{S}$ matrix by the equation

$$\mathbf{S} = (1 + i\mathbf{R})\,(1 - i\mathbf{R})^{-1}\,.$$

As expected, the R matrix is Hermitian, and if the potential describing the scattering is real, the elements R_{ij} are real and the matrix is symmetric. This is why it is frequently advantageous to work with $\mathbf{R}$ instead of the $\mathbf{S}$ matrix. Furthermore, any approximation to $\mathbf{R}$ that preserves the symmetry of the matrix ensures that $\mathbf{S}$ is unitary and hence that the total number of particles in the system is conserved.

In this method, the configuration space is divided into two regions. For the scattering of electrons from an atom, one can exclude exchange outside some radius r_0. Hence, if $r > r_0$, the collision is described by coupled differential instead of integrodifferential equations that often have analytic solutions easily obtained. The basic problem is, then, to calculate the $\mathbf{R}$ matrix elements in the internal region $r > r_0$. The $\mathbf{S}$ matrix and cross section can then be obtained from the $\mathbf{R}$ matrix trough the solution of the external region. The computational time required for such calculations compete with those of the DWA.

1.3   Thesis Outlook

After describing the main goals and motivations behind this thesis, a brief outlook of the organization of this work is in order. This thesis is comprised of two parts,

- Part I is entirely devoted to the formulation and subsequent testing of an analytical expression for the calculation of electron impact ionization cross sections. The derivation of the key ingredients of the theory are presented and the role of the scaling laws for binary encounter theories is analysed. The modified expression is then compared to inner-shell ionization experimental and theoretical results as well as total ionization of highly charged ions.

- Part II describes the experimental work performed on a double crystal spectrometer (DCS) coupled to an electron-cyclotron-resonance ion-source (ECRIS) in order to obtain absolute measurements in the X-ray domain. This instrument provides accurate and absolute measurements of X-ray energies and widths, thus allowing a reference-free comparison with *state of art* QED and many-body theory calculations reported in the literature. An overview of the experimental apparatus is given, and the improvements made are highlighted. An absolute measurement of the "Relativistic $M1$" transition energy in helium-like argon is presented and the response function of the instrument is probed. Finally an X-ray spectrum of an argon plasma is analysed, using some tools developed in Part I, in order to obtain an external reference of the charge state distribution inside the ECRIS plasma.

Scattering Cross Sections

2.1 Rutherford scattering

The scattering of charged particles has been under the scope of scientists since the beginning of last century. One of the first puzzling phenomena observed was the Geiger-Mardsen experiment, which lead to the development of the Rutherford model for scattering.

Scattering in a coulomb field is of particular interest for physicists that study charged particles interactions. In the case of a elastic colision we can use quantum mechanics to describe the scattering cross section and it will yield the same result as if we use classical physics.

When there is a fixed direction (in this case, the direction of the incident particle), Schroedinger's equation can be solved by using a set of parabolic coordinates (ξ, η, ϕ).

The Schroedinger equation, with μ as the reduced mass between the two colliding particles,

$$\left[-\frac{\hbar^2}{2\mu} \Delta + V(r) \right] \psi = E\psi, \tag{2.1}$$

becomes, if we set the potential as being of a Coulomb nature, $V = -\frac{1}{r} = -\frac{2}{\xi+\eta}$

$$\frac{4}{\xi+\eta} \left[\frac{\partial}{\partial \xi} \left(\xi \frac{\partial \psi}{\partial \xi} \right) + \frac{\partial}{\partial \eta} \left(\eta \frac{\partial \psi}{\partial \eta} \right) \right] + \frac{1}{\xi\eta} \frac{\partial^2 \psi}{\partial \phi^2} + 2 \left(E + \frac{2}{\xi+\eta} \right) \psi = 0. \tag{2.2}$$

Since the problem of the scattering of a particle in a central field is axially symmetric, and hence independent of the coordinate ϕ, we can write the particular solution of the Schroedinger's equation as

$$\psi = \psi_1(\xi) \psi_2(\eta). \tag{2.3}$$

Substituting Eq. (2.3) in (2.2), we obtain, after separation of variables

$$\frac{\partial}{\partial \xi} \left(\xi \frac{\partial \psi_1(\xi)}{\partial \xi} \right) + \left(\frac{1}{4} k^2 \xi - a \right) \psi_1(\xi) = 0, \tag{2.4}$$

$$\frac{\partial}{\partial \eta} \left(\eta \frac{\partial \psi}{\partial \eta} \right) + \left(\frac{1}{4} k^2 \eta - b \right) \psi_2(\eta) = 0,$$

with the separation variables obeying the following relation

$$a + b = 1.$$

Here we have put the energy (in atomic units) $E = \frac{1}{2}k^2$, where k is the momentum of the projectile. The signs in Eqs. (2.4) are for the case of a repulsive field, but the final result

will be the same for attractive fields, hence the scattering of positrons by electrons will have the same cross sections, in Rutherford's theory, as the electron-electron case.

Now we shall find the solution of Schroedinger's equation which, for large r (and negative z, since we are saying that the incident particle travels with the direction of the positive z), has the form of a plane wave

$$\psi \approx e^{ikz}, \quad -\infty < z < 0, \quad r \to \infty,$$

corresponding to a particle travelling in the positive z-axis direction and very far away from the scattering center. In parabolic coordinates, this takes the form

$$\psi \approx e^{ik(\xi-\eta)/2}, \quad \eta \to \infty, \quad \xi \in \mathbb{R}.$$

One easy way to satisfy this condition will be to set

$$\psi_1(\xi) = e^{ik\xi/2}, \tag{2.5}$$

and

$$\psi_2(\eta) \approx e^{-ik\eta/2}. \tag{2.6}$$

Substituting Eq. (2.5) in the first equation of the system (2.4), we observe that this function does indeed satisfy the equation, provided that $a = \frac{1}{2}ik$. The second equation, with $b = 1 - a$, will then become

$$\frac{\partial}{\partial \eta}\left(\eta \frac{\partial \psi}{\partial \eta}\right) + \left(\frac{1}{4}k^2\eta - 1 + \frac{1}{2}ik\right)\psi_2(\eta) = 0.$$

Given the guess we made earlier for $\psi_2(\eta)$, we shall seek the above equation's solution in the form

$$\psi_2(\eta) = e^{-ik\eta/2}w(\eta),$$

were the function $w(\eta)$ must tend to a constant as $\eta \to \infty$. The resulting differential equation will be

$$\eta w'' + (1 - ik\eta)w' - w = 0, \tag{2.7}$$

which, introducing the new variable $\eta_1 = ik\eta$, can be reduced to the equation for a confluent hypergeometric function with parameters $\alpha = -i/k$, and $\gamma = 1$. We must choose the right solution of Eq. (2.7), so that the product of it by $\psi_1(\xi)$ will only contain an outgoing spherical wave. It can be written as (A being an arbitrary constant)

$$w = A \times F(-1/k, 1, ik\eta).$$

Assembling the functions obtained and choosing a normalization constant such that the incident wave will have unit amplitude, we get the wavefunction [Eq. (2.3)], describing the scattering, as

$$\psi = e^{-\pi/2k}\Gamma\left(1 + \frac{i}{k}\right)e^{ik(\xi-\eta)/2}F\left(-\frac{1}{k}, 1, ik\eta\right). \tag{2.8}$$

For simplicity in calculating the cross section from the wave equation, we need to obtain the asymptotic behaviour of Eq. (2.8), and after changing to spherical polar coordinates, and some straightforward algebraic calculation, we have the final asymptotic expression for the wavefunction

$$\psi = \left[1 + \frac{1}{2k^3r(1 - \cos\theta)}\right]e^{ikz+(i/k)\log(kr-kr\cos\theta)} + \frac{f(\theta)}{r}e^{ikr-(i/k)\log(2kr)}, \tag{2.9}$$

with

$$f(\theta) = -\frac{1}{2k^2\sin^2\frac{1}{2}\theta}e^{(2i/k)\log\sin\theta/2}\frac{\Gamma(1 + i/k)}{\Gamma(1 - i/k)}. \tag{2.10}$$

The first term in Eq. (2.9) represents the incident wave, and we can see that even at large distances, the wave is somewhat distorted, mainly because of the logarithmic term in the phase and the presence of the $1/r$ dependence in the amplitude.

Thus, bearing in mind that the effective scattering cross section can be calculated as $d\sigma = |f(\theta)|^2 d\Omega$, we get for the Rutherford cross section

$$d\sigma = \frac{d\Omega}{4k^4 \sin^4 \frac{1}{2}\theta},$$

or in ordinary units,

$$d\sigma = \left(\frac{\alpha}{2mv^2}\right)^2 \frac{d\Omega}{\sin^4 \frac{1}{2}\theta}, \tag{2.11}$$

where we have set the relative velocity of the particles $v = k\hbar/m$, and α is the fine-structure constant. Expression (2.11) is the familiar Rutherford's formula given by classical mechanics, as can be seen in the references [43] and [40].

Expressing Eq. (2.11) in a coordinate system in which one of the particles is at rest is very easy, since we know that for a collision between particles with the same mass, changing from the center of mass frame to the laboratory frame corresponds to changing from $\theta \rightarrow 2\vartheta$. The element of solid angle $d\Omega$ must be replaced by $4\cos\vartheta d\Omega$ in the new coordinate system. After algebraic manipulation, Eq. (2.11) becomes

$$d\sigma = \left(\frac{\alpha}{mv^2}\right)^2 \frac{1}{\sin^4 \vartheta,} \cos\vartheta d\Omega, \tag{2.12}$$

where v is the relative velocity between the two electrons and m is the electron rest mass. At this point it is convenient to express the scattering angle ϑ in terms of the energy which the ejected electron has after the collision. As is well known, when a particle of kinetic energy $T = \frac{1}{2}mv^2$ collides with another of the same mass at rest, the energy with which the particles are left is

$$W = T\sin^2\vartheta, \qquad T - W = T\cos^2\vartheta, \tag{2.13}$$

where W stands for kinetic energy of the ejected electron. In order to solve Eq. (2.12) with respect to the energy of the ejected electron, we express $d\Omega$ in terms of dW by the relation $\cos\vartheta d\Omega = 2\pi \sin\vartheta \cos\vartheta d\vartheta = (\frac{\pi}{T})dW$. Substituting in Eq. (2.12) and writing the fine-structure constant α as a function of the Bohr radius, we get the energy distribution of the ejected electron

$$\frac{d\sigma(W,T)}{dW} = \frac{4\pi a_0^2 R^2}{T} \frac{1}{W^2}. \tag{2.14}$$

In Eq. (2.14), T is the non-relativistic relative kinetic energy of the incident electron, W is the kinetic energy of the ejected electron, a_0 is the Bohr radius ($a_0 = 5.29 \times 10^{-11}$ m) and R is the Rydberg energy ($R = 13.6$ eV). After inspection, we see that Eq. (2.14) diverges for $W \rightarrow 0$, although we know that for a real atom, the cross section for ejecting an electron with $W = 0$ is finite. To overcome this difficulty we can replace W by the energy transfer

$$E = W + B, \tag{2.15}$$

where B is the binding energy of the ejected electron. With this substitution, the Rutherford cross section becomes

$$\frac{d\sigma(W,T)}{dW} = \frac{d\sigma}{dE} = \frac{4\pi a_0^2 N R^2}{T} \frac{1}{E^2}, \tag{2.16}$$

where we have inserted the number of bound electrons, N, in the sub-shell.

2.2 Scattering of like-particles

In the case of electron-electron collision, which is the main subject in this part, the indistinguishability of the colliding particles raise special considerations. As we know, this identity leads, in quantum mechanics, to the appearance of a peculiar exchange interaction between them. This has an important effect on scattering as described by Mott [42]. The orbital wavefunction of a system with two like-particles must be symmetric or antisymmetric with respect to coordinate change, according to whether their total spin is even or odd [40]. The wavefunction that describes the scattering, and which is obtained by solving the usual Schroedinger's equation [Eq. (2.1)], must then be symmetrized or anti-symmetrized with respect to the particles. In this case, an interchange of the particles, corresponds to reversing the direction of the radius vector joining them, and in the coordinate system in which the center of mass is at rest, this is equivalent to changing the scattering angle θ to $\pi - \theta$ (and hence $z = r\cos\theta$ becomes $-z$). So, instead of the asymptotic expression, [Eq. (2.9)] we have

$$\psi \approx e^{ikz} \pm e^{-ikz} + \frac{e^{ikr}}{r} \left[f\left(\theta\right) \pm f\left(\pi - \theta\right) \right]. \tag{2.17}$$

It is impossible to distinguish the two electrons apart, so we can't say which of them scatters and which is scattered, thus we now have two incident plane waves that propagate in opposite directions, and the outgoing spherical wave must take into account the scattering of both particles. The probability current calculated from it, must then result in the probability that either one of the particles will be scattered into the element $d\Omega$ of solid angle considered. The effective cross section will be the ratio between this current and the current density of either of the incident plane waves. This results, as before, in the squared modulus of the $\frac{e^{ikr}}{r}$ term's coefficient in the wave function [Eq. (2.17)].

If the total spin of the colliding particles is even (symmetric form), the effective cross section must take the form

$$d\sigma^+ = \left| f\left(\theta\right) + f\left(\pi - \theta\right) \right|^2 d\Omega, \tag{2.18}$$

and if the spin is odd (antisymmetric form) it is

$$d\sigma^- = \left| f\left(\theta\right) - f\left(\pi - \theta\right) \right|^2 d\Omega. \tag{2.19}$$

In classical mechanics, the probability that either particle would be scattered through a given solid angle $d\Omega$ would be just the sum of probabilities that one of them is deviated by an angle θ and the other by an angle $\pi - \theta$. In other words, the effective cross section would be

$$d\sigma = \left(\left| f\left(\theta\right) \right|^2 + \left| f\left(\pi - \theta\right) \right|^2 \right) d\Omega.$$

The appearance of the interference term, $f\left(\theta\right) f^*\left(\pi - \theta\right) + f^*\left(\theta\right) f\left(\pi - \theta\right)$ characterizes the exchange interaction, and its nature is purely quantum mechanical.

In the symmetric [Eq. (2.18)] and antisymmetric [Eq. (2.19)] cross sections, one needs to know the definite value of the total spin but, usually, such information is not available. We must, then, average over all possible spin states to calculate the effective cross section assuming that all spin states are equally probable. It is well known that of the total number of spin states of a system with two particles with spin s (s being half-integral), $s\left(s+1\right)$ states correspond to an even total spin, and $\left(s+1\right)\left(2s+1\right)$ to an odd total spin (if s is integral the inverse applies). So, using the Lagrange definition of probability [40], we get that the probability that the system of two colliding, half-integral spin, particles will have an even total spin S is $s/\left(2s+1\right)$ and the probability of odd S is $\left(s+1\right)/\left(2s+1\right)$. Hence, the effective cross section will be

$$d\sigma^\pm = \frac{s}{2s+1} d\sigma^+ + \frac{s+1}{2s+1} d\sigma^-. \tag{2.20}$$

Substituting Eqs. (2.19) and (2.18) on Eq. (2.20), we obtain

$$d\sigma^\pm = \left(|f(\theta)|^2 + |f(\pi - \theta)|^2 - \frac{1}{2s+1} [f(\theta) f^*(\pi - \theta) + f^*(\theta) f(\pi - \theta)] \right) d\Omega. \quad (2.21)$$

2.2.1 Coulomb scattering of like-particles

As an example we will obtain the formulas for electron-electron scattering. We know that the interaction between the two electrons is of a Coulomb nature, so if we insert the scattering amplitude, obtained for the Rutherford expression, [Eq. (2.10)],

$$f(\theta) = -\frac{1}{2k^2 \sin^2 \frac{1}{2}\theta} e^{-(2i/k)\log \sin \theta/2} \frac{\Gamma(1 + i/k)}{\Gamma(1 - i/k)}, \quad (2.22)$$

in Eq. (2.21), and set $s = \frac{1}{2}$ we obtain

$$d\sigma^\pm = \left(\frac{e^2}{mv^2} \right)^2 \left[\frac{1}{\sin^4 \frac{1}{2}\theta} + \frac{1}{\cos^4 \frac{1}{2}\theta} - \frac{\cos \left(\frac{e^2}{\hbar v} \log \tan^2 \frac{1}{2}\theta \right)}{\sin^2 \frac{1}{2}\theta \cos^2 \frac{1}{2}\theta} \right] d\Omega \quad (2.23)$$

where, m and e is the electron's mass and charge respectively, v is the electron's velocity on the center of mass coordinate system and $\hbar$ is Plank's constant divided by 2π. If we transform the formula to a coordinate system in which one of the electrons is at rest, we obtain [40]

$$d\sigma^\pm = \left(\frac{2e^2}{mv^2} \right)^2 \left[\frac{1}{\sin^4 \vartheta} + \frac{1}{\cos^4 \vartheta} - \frac{\cos \left(\frac{e^2}{\hbar v} \log \tan^2 \vartheta \right)}{\sin^2 \vartheta \cos^2 \vartheta} \right] \cos \vartheta d\Omega \quad (2.24)$$

where the element of solid angle, $d\Omega = \sin \theta \, d\theta d\phi$ was replaced by $4 \cos \vartheta \sin \vartheta \, d\vartheta d\phi = 4 \cos \vartheta d\Omega$.

2.3 Mott cross section

Based on the derivation above, Mott has generalized the Rutherford cross section for the collision between two electrons, by taking exchange into account [40, 42]. As in the Rutherford expression [Eq. (2.14)], by solving the singly differential cross section (SDCS) to obtain the energy distribution of the ejected electron, W, we get

$$\frac{d\sigma(W, T)}{dW} = \frac{4\pi a_0^2 R^2}{T} \left[\frac{1}{W^2} - \frac{\Phi}{W(T - W)} + \frac{1}{(T - W)^2} \right], \quad (2.25)$$

where Φ is a function of E and T that lies is the $[0, 1]$ interval and approaches 1 for large values of T, and is given by

$$\Phi = \cos \left[\sqrt{\left(\frac{R}{T + B} \right)} \ln \left(\frac{T}{B} \right) \right]. \quad (2.26)$$

As before, T is the non-relativistic kinetic energy of the incident electron and $T - W$ is the kinetic energy of the scattered electron. The first term of Eq. (2.25) is the direct collision term as in the Rutherford formula, while the third term represents the exchange. The second term is the interference between the direct and exchange terms. Note that the Mott expression is symmetric in respect to the kinetic energies of the ejected electron W and the scattered electron $T - W$, as it was expected to be. Similarly to the Rutherford expression, the Mott SDCS diverges when $W \to 0$ and $W \to T$, which is not true for a real atom because the

binding energy must be overcome for a bound electron to be ejected. Hence, by substituting W for the energy transfer, E [Eq. (2.15)], we get

$$\frac{d\sigma\,(W,T)}{dW} = \frac{d\sigma}{dE} = \frac{4\pi a_0^2 NR^2}{T} \left[\frac{1}{E^2} - \frac{\Phi}{E\,(T-W)} + \frac{1}{(T-W)^2} \right], \qquad (2.27)$$

where we have included the occupation number, N, of the sub-shell undergoing ionization. Note that while the original Mott cross section, Eq. (2.25), is an exact solution for two unbound electrons, [Eq. (2.27)] is an approximation for a bound target electron, which becomes a very good approximation for $W \gg B$.

2.4 Binary encounter (BE) theory

Up to now the cross sections derived report to an electron with kinetic energy T colliding with another electron at rest. To better describe the ionization of an atom by an electron, Vriens, following the work of Gryzinski, proposed that the target electron should be assigned a velocity or momentum distribution to represent its orbital motion [21, 47]. Such momentum distribution is usually derived from the bound electron wave function.

Deriving the binary encounter cross section for the collision between two electrons we can, from first principles, arrive at an exact solution for a collision between an incident electron with kinetic energy T and a target electron with an average kinetic energy U. The average kinetic energy is obtained through

$$U \equiv \frac{\langle \mathbf{p}^2 \rangle}{2m},$$

where $\mathbf{p}$ is the momentum operator in a given sub-shell. The quantum mechanical solution for this problem can be calculated analytically and the symmetrical binary encounter model of Thomas, Burgess and Vriens can be presented as [47]

$$d\sigma(E,T) = \frac{4\pi a_0^2 NR^2}{T} \left[\frac{1}{E^2} + \frac{4U}{3E^3} + \frac{1}{(T-U-E)^2} \right.$$
$$\left. + \frac{4U}{3\,(T-U-E)^3} - \frac{\Phi}{E\,(T-U-E)} \right] dE. \qquad (2.28)$$

Due to the Coulomb interaction between the elements involved in the process, we should note that the incident and ejected electrons energies are not constant throughout the collision, and must be changed if we want to better describe the ionization of multi-electronic atoms. Burgess and Vriens have proposed a change in the binary encounter cross section to describe this effect. As can be seen in Fig. 2.1, the changes are due to the Coulomb interaction between the incident and ejected electron with the nucleus and other bound electrons.

For hydrogen, the potential energy of an electron in the lowest bound state corresponds to 1 a.u. because it is the sum of the binding energy B and the kinetic energy U. Vriens proposed that this change in energy should be inserted in the binary encounter theory, Eq. (2.28), although it is only correct for Hydrogen. Hence, if we change $T \rightarrow T + U + B$, which should be referred from now on as the "'Burgess-Vriens"' term or denominator, and taking into account Eq. (2.15), we can simplify the binary encounter expression to

$$d\sigma(E,T) = \frac{4\pi a_0^2 NR^2}{T+U+B} \left[\frac{1}{E^2} - \frac{\Phi}{E\,(T-W)} + \frac{1}{(T-W)^2} \right.$$
$$\left. + \frac{4U}{3} \left(\frac{1}{E^3} + \frac{1}{(T-W)^3} \right) \right] dW. \qquad (2.29)$$

This expression is the same obtained by Kim *et al* [10] if we set $\Phi = 1$. In L. Vriens 1966 paper [24], a detailed description of the Φ function, is given. In most of the binary
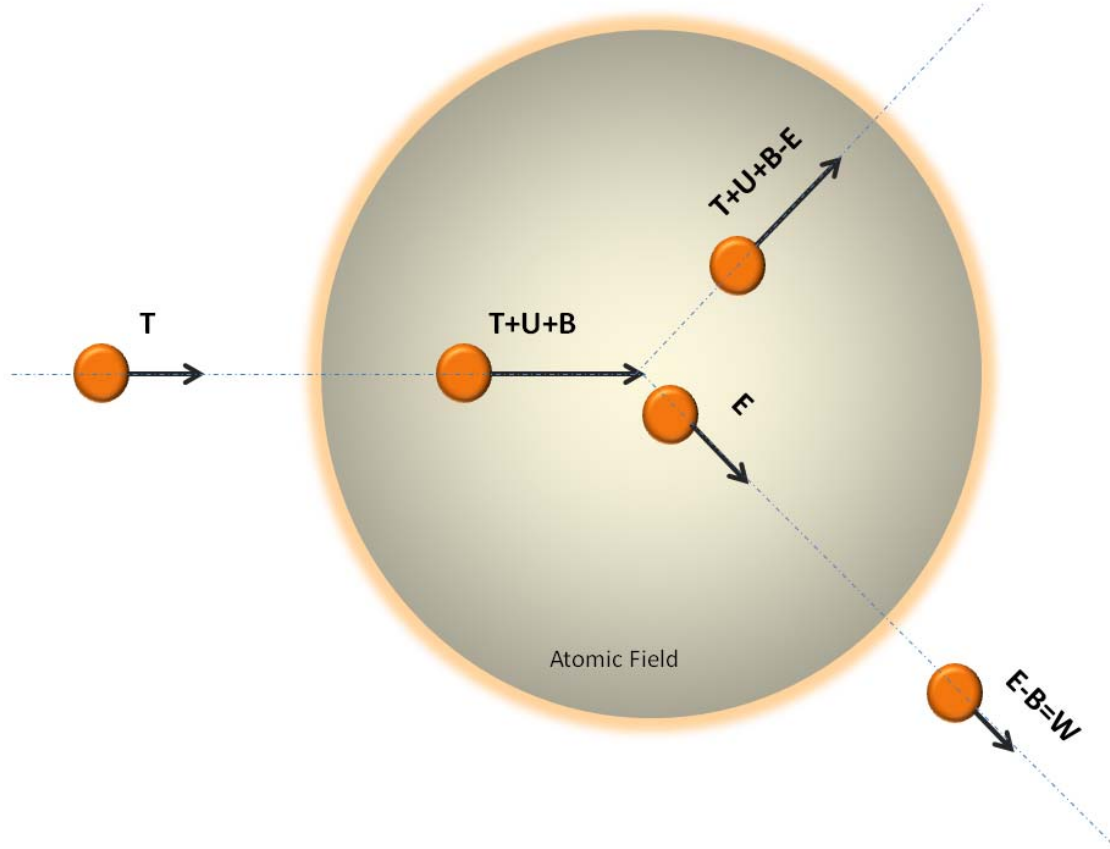
Figure 2.1: Kinetic energies of the primary and secondary electrons before and after the binary collision as proposed by Vriens.

encounter-derived models, the Vriens Φ function is set to unity, although this approximation is only valid if the binding energy of the atomic electron is much higher than the Rydberg energy, and we can get differences of as much as 15% in the cross section values for binding energies of few eV. This may be of some importance for molecules and outer shell ionization of atoms and lowly charged ions. In Fig. 2.2 we can see the behaviour of the Φ function for several B/R ratios.

At this point it is convenient to express the energy variables in units of the binding energy B of the electrons in a sub-shell;

$$
\begin{aligned}
t &= T/B, \\
w &= W/B, \\
u &= U/B, \\
S &= 4\pi a_0^2 N(R/B)^2.
\end{aligned}
\tag{2.30}
$$

Performing this variable substitution, we get

$$
\begin{aligned}
\frac{d\sigma\,(W,T)}{dW} &= \frac{d\sigma\,(w,t)}{B dw} \\
&= \frac{S}{B\,(t+u+1)} \left[\frac{1}{(w+1)^2} + \frac{1}{(t-w)^2} - \frac{\phi}{(w+1)\,(t-w)} \right. \\
&\quad \left. + \frac{4u}{3} \left(\frac{1}{(w+1)^3} + \frac{1}{(t-w)^3} \right) \right],
\end{aligned}
\tag{2.31}
$$
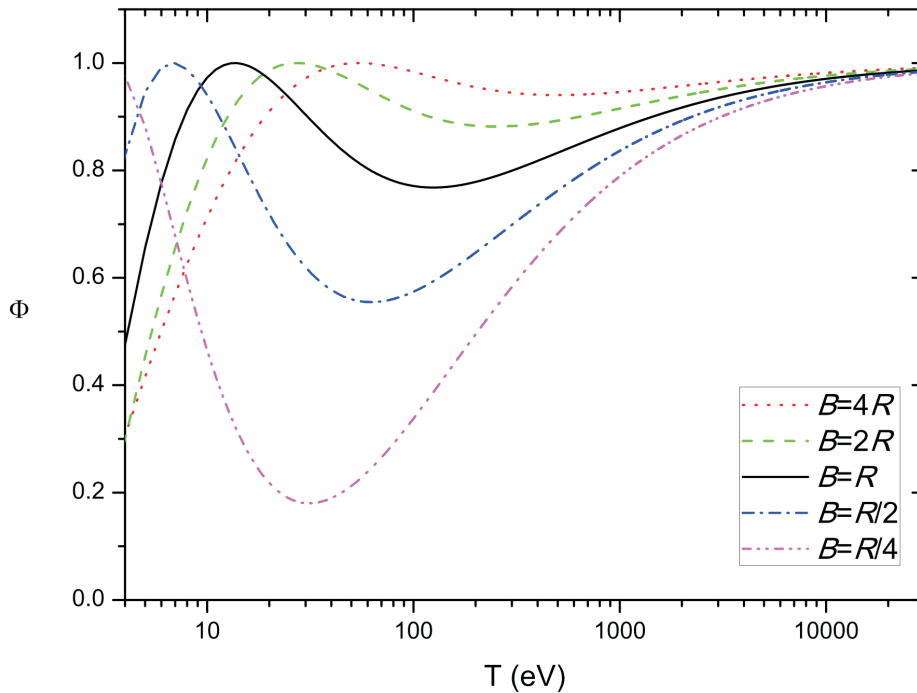
Figure 2.2: Plot of the Vriens Φ function for several B/R ratios.

with

$$\phi = \cos\left(\sqrt{\frac{R}{B(t+1)}} \ln t\right).$$ (2.32)

2.5 Binary encounter dipole (BED) model

The following derivation was originally proposed by Kim and Rudd [10], and is transcribed here to better understand the origin of each term of the final expression. The binary encounter singly differential cross section, Eq. (2.31), can be recast as a series

$$\frac{d\sigma(W,T)}{dW} = \frac{S}{B} \sum_{n=1}^{3} F_n(t) \left[\frac{1}{(w+1)^n} + \frac{1}{(t-w)^n}\right],$$ (2.33)

where the terms containing $w+1$ represent the secondary electron, which is ejected from the target after the collision, and the terms containing $t-w$ represent the primary or scattered electron which has lost energy in the collision. As was mentioned before, the $n=1$ terms represents the interference between the direct and exchange collisions, the $n=2$ terms is due to the close or hard collisions, in which the momentum transfer from the primary to the secondary electrons is large. The terms corresponding to $n=3$ accounts for the broadening of the energy distribution due to the intrinsic momentum of the bound electron in the atom. The binary encounter cross section, Eq. (2.31), can be reproduced by the following choice of $F_n(t)$

$$F_1 = -\frac{F_2\phi}{t+1}, \quad F_2 = \frac{1}{t+u+1}, \quad F_3 = \frac{4u}{3(t+u+1)}.$$ (2.34)

The total ionization cross section (TICS) can be obtained by integrating Eq. (2.33) from $w = 0$ to $w = (t-1)/2$, with the choice of functions of Eq. (2.34). Hence, we get

$$\sigma_{\mathrm{BE}} = \int_0^{(t-1)/2} \frac{d\sigma(w,t)}{dw} dw \tag{2.35}$$

$$= S\left[F_1 \ln t + F_2(1 - t^{-1}) + \frac{1}{2}F_3(1 - t^{-2})\right]. \tag{2.36}$$

Analysing the asymptotic $(t \gg 1)$ behaviour of Eq. (2.36), we conclude that the obtained trend $(\sigma_{BE} \to t^{-1})$ is in disagreement with the prediction of Bethe's "Theory of the Passage of Fast Corpuscular Rays Through Matter" [11] and with experimental results. A more realistic asymptotic t dependence is predicted by Bethe's theory, namely $t^{-1}\ln t$, which arises from the dipole interaction of soft or far collisions. In order to correct such deficiency, one must consider that at high energies $(t \gg w)$, the terms $(t-w)^{-n}$ may be ignored, i.e.

$$\frac{d\sigma(W,T)}{dW} = \frac{S}{B}\sum_{n=1}^{3} F_n(t) f_n(w), \tag{2.37}$$

with

$$f_n(w) = \frac{1}{(w+1)^n}, \qquad \text{for } n = 1, 2, \tag{2.38}$$

while $F_n(t)$ and $f_3(w)$ are to be determined. In order to derive an expression that combines the classical binary encounter theory with the leading dipole part of Bethe's theory, we need to introduce the stopping cross section for ionization, σ_{SP}, which is defined by

$$\sigma_{\mathrm{SP}} \equiv \frac{B}{R}\int_0^{(t-1)/2} (w+1)\frac{d\sigma(w,t)}{dw} dw. \tag{2.39}$$

The asymptotic limits of σ_{BE} and σ_{SP} are obtained by substituting Eq. (2.37) on Eqs. (2.35) and (2.39):

$$\sigma_{\mathrm{BE}} = S(F_1 \ln t + F_2 + F_3 G), \tag{2.40}$$

where

$$G = \int_0^\infty f_3(w)\,dw, \tag{2.41}$$

and

$$\sigma_{\mathrm{SP}} = \frac{SB}{R}((\ln 2)F_1 t + F_2 \ln t + F_3 H), \tag{2.42}$$

where

$$H = \int_0^\infty (w+1)f_3(w)\,dw. \tag{2.43}$$

The upper limits for the integration of G and H have been extended to ∞ in the anticipation that $f_3(w)$ diminishes rapidly enough as $w \to \infty$. This way, the asymptotic part of $f_3(w)$ does not contribute to the asymptotic t dependence in Eqs. (2.40) and (2.42) hence, it is a requirement that $f_3(w) \to w^{-m}$ with $m > 2$ for $w \gg 1$.

The asymptotic ionization and stopping cross sections, σ_B and σ_{BSP} respectively, derived by Bethe in the first Born approximation [11, 28] are,

$$\sigma_{\mathrm{B}} = \frac{SQ}{2}\frac{\ln t}{t}, \tag{2.44}$$

where

$$Q = \frac{2BM_i^2}{NR}, \qquad\qquad M_i^2 = \frac{R}{B}\int_0^\infty \frac{1}{w+1}\frac{df(w)}{dw} dw, \tag{2.45}$$

and

$$\sigma_{BSP} = \frac{2SB}{R}\frac{\ln t}{t}. \tag{2.46}$$

In the derivation of Eq. (2.46), excitations to both discrete and continuum states were included, because the coefficient of the $t^{-1}\ln t$ term for ionization alone, not only is very hard to calculate but will also be different from one atom to another. Nevertheless, at high incident energies, ionization processes account for more than 80% of the cross section [48], hence using both excitations and ionization is a simple yet effective way of obtaining the asymptotic stopping power in the Bethe's formalism. Matching the asymptotic expressions for ionization and stopping cross sections of the binary encounter theory, Eqs. (2.40) and (2.42) with those obtained by Bethe, Eqs. (2.44) and (2.46), respectively we get

$$F_1\ln t + F_2 + F_3 G = \frac{Q}{2}\frac{\ln t}{t}, \tag{2.47}$$

$$(\ln 2)\, F_1 t + F_2\ln t + F_3 H = 2\frac{\ln t}{t}. \tag{2.48}$$

There is no function $F_1\,(t)$ that will yield a $t^{-1}\ln t$ dependence on both Eqs. (2.47) and (2.48), so we choose F_1 in such a way that it will fall off faster than $t^{-1}\ln t$ so as to become asymptotically negligible in both equations. The simplest way to accomplish this is to make $F_1 \propto t^{-2}$. This is consistent with the t dependence of the F_1 term in the binary encounter cross section, Eq. (2.34), as long as we make it negative. If we choose $F_2 \propto t^{-1}$, as in the binary encounter expression, the second term of Eq. (2.47) becomes asymptotically negligible, but the second term in Eq. (2.48) yields the expected $t^{-1}\ln t$ dependence. With this choices for the first two coefficients, F_3 dominates the asymptotic equation for ionization, while for the stopping cross section Eq. (2.48), the second and third terms dominate.

The asymptotic SDCS expression in the Bethe theory is given by [49]

$$\frac{d\sigma}{dw} = \frac{S\ln t}{Nt}\frac{1}{w+1}\frac{df\,(w)}{dw}, \tag{2.49}$$

where $df\,(w)\,/dw$ is the differential oscillator strength. Since the asymptotic limit of Eq. (2.37) is

$$\frac{d\sigma}{dw} = SF_3\,(t)\, f_3\,(w)\,, \tag{2.50}$$

we can conclude from Eqs. (2.49) and (2.50) that

$$F_3\,(t)\, f_3\,(w) = \frac{\ln t}{Nt}\frac{1}{w+1}\frac{df\,(w)}{dw}. \tag{2.51}$$

An obvious choice is to set

$$F_3\,(t) = \frac{\ln t}{t} \qquad \text{and} \qquad f_3\,(w) = \frac{1}{N\,(w+1)}\frac{df\,(w)}{dw}. \tag{2.52}$$

From this choice of $f_3\,(w)$, the definition of M_i^2 [Eq.(2.45)] and Eqs. (2.41) and (2.43) respectively, we get

$$
\begin{aligned}
G &= \frac{1}{N}\int_0^\infty \frac{1}{w+1}\frac{df\,(w)}{dw}dw \\
&= \frac{BM_i^2}{RN},
\end{aligned}
\tag{2.53}
$$

and

$$
\begin{aligned}
H &= \frac{1}{N}\int_0^\infty \frac{df\,(w)}{dw}dw, \\
&= \frac{N_i}{N},
\end{aligned}
\tag{2.54}
$$

where

$$N_i \equiv \int_0^\infty \frac{df(w)}{dw} dw. \tag{2.55}$$

This choice of $f_3(w)$ satisfies the requirement made above which led to the extension of the integral limits in Eqs. (2.41) and (2.43) to ∞, since the differential oscillator strength [28] diminishes in the asymptotic region faster than $w^{-3.5}$.

To find $F_2(t)$ and $F_3(t)$ we start by writing $F_2 = at^{-1}$, then from the second and third terms of Eq. (2.48) we get

$$\frac{a \ln t}{t} + \frac{N_i \ln t}{Nt} = 2\frac{\ln t}{t}, \tag{2.56}$$

which leads to $a = 2 - (N_i/N)$, or

$$F_2(t) = \frac{2 - (N_i/N)}{t} \qquad \text{and} \qquad F_3(t) = \frac{\ln t}{t} \qquad \text{for} \qquad t \gg 1. \tag{2.57}$$

What we have done so far was basically to let the $F_3 f_3$ term in Eq. (2.33) represent the dipole interaction. The Bethe theory is not usually used in the symmetric form, i.e., it does not have the exchange and interference terms as in the Mott cross section. It is not clear what the appropriate symmetric form of the dipole interaction should be, so we simply omit the exchange term $(t-w)^{-3}$ in Eq. (2.33). Besides, the exchange interaction becomes negligible at high incident energies where the dipole interaction is important.

Finally, the choice for F_3 and f_3 is combined with the symmetric binary encounter cross section, Eq. (2.34), and result in

$$F_1 = -\frac{F_2 \phi}{t+1}, \qquad F_2 = \frac{2 - (N_i/N)}{t+u+1}, \qquad F_3 = \frac{\ln t}{t+u+1}. \tag{2.58}$$

We can now write the SDCS of a sub-shell, based on the BED model, by combining the definition of $f_3(w)$ defined in Eq. (2.52), the $F_n(t)$ coefficients defined in Eq. (2.58) on Eq. (2.33)

$$\frac{d\sigma(W,T)}{dW} = \frac{S}{B(t+u+1)} \left[\phi \frac{(N_i/N) - 2}{t+1} \left(\frac{1}{(w+1)} + \frac{1}{(t-w)} \right) \right.$$
$$\left. + [2 - (N_i/N)] \left(\frac{1}{(w+1)^2} + \frac{1}{(t-w)^2} \right) + \frac{\ln t}{N(w+1)} \frac{df(w)}{dw} \right]. \tag{2.59}$$

In order to use the BED model, values of B, U, N and the differential oscillator strengths, $df(w)/dw$, are needed for each sub-shell of an atom. Of these values, B and N are readily available in the literature, while the average kinetic energy U can be calculated from electronic structure codes such as those developed by Desclaux and Indelicato [50, 51] and Froese-Fisher [52]. Differential oscillator strengths are usually harder to get, although total and partial values of $df(w)/dw$ for many atoms can be found in the literature.

In Ref. [10] a list with the relevant values for the application of the BED model to H, He, Ne and H_2 is presented. The differential oscillator strengths for these targets are also listed as fits to experimental values except for H for which theoretical values have been used in the fitting process. Although any form of theoretical $df(w)/dw$ can be used, analytic fits are certainly more convenient to use than numerical tables or graphs.

2.6 Binary encounter Bethe (BEB) model

As Kim *et al* [10] pointed out, although the BED model is substantially simpler to use than most *ab initio* theories for electron impact ionization, the differential oscillator strengths are usually not very simple to obtain, especially sub-shell by sub-shell. Because of this,

and taking into account our main goal of obtaining a simple, analytical expression free of adjustable parameters, a simplified version of the BED model is needed. In this version, to be referred as binary encounter Bethe (BEB) model, we follow the derivation of Kim and Rudd [10] that make use of the fact that differential oscillator strengths for targets such as H, He and H_2 have simple shapes, and can be cast as a series of inverse powers of $w + 1$, starting from $(w + 1)^{-2}$, that is,

$$\frac{df(w)}{dw} = \frac{b}{(w + 1)^2} + ..., \tag{2.60}$$

where b is a constant. If we truncate the series in the first term, we can get simple functions for N_i and M_i^2,

$$N_i = b \int_0^\infty \frac{dw}{(w + 1)^2} = b, \tag{2.61}$$

$$M_i^2 = \frac{Rb}{B} \int_0^\infty \frac{dw}{(w + 1)^3} = \frac{Rb}{2B}. \tag{2.62}$$

By combining Eqs. (2.45), (2.61) and (2.62), we get

$$M_i^2 = \frac{RN_i}{2B} \qquad \text{and} \qquad Q = \frac{N_i}{N}. \tag{2.63}$$

Going back to our choice of F_3 and f_3 and taking note that both functions will always be used as a product and not individually, we can rewrite Eq. (2.51) using the first term of Eq. (2.60), Eq. (2.61) and Eq. (2.63) and obtain

$$F_3(t) f_3(w) = \frac{Q \ln t}{Nt} \frac{1}{(w + 1)^3}, \tag{2.64}$$

after which we can, just to simplify our notation for f_3, separate to

$$F_3(t) = \frac{Q \ln t}{t} \qquad \text{and} \qquad f_3(w) = \frac{1}{(w + 1)^3}. \tag{2.65}$$

Combining Eqs. (2.33), (2.58), (2.63) and (2.65), the SDCS in the BEB formalism is given by

$$\frac{d\sigma(W, T)_{\text{BEB}}}{dW} = \frac{S}{B} \sum_{n=1}^3 F_n(t) \left[\frac{1}{(w + 1)^n} + \frac{1}{(t - w)^n} \right] \tag{2.66}$$

where

$$F_1 = -\frac{F_2 \phi}{t + 1}, \qquad F_2 = \frac{2 - Q}{t + u + 1}, \qquad F_3 = \frac{Q \ln t}{t + u + 1}. \tag{2.67}$$

When nothing is known, apart from the binding and kinetic energies of the electron undergoing ionization, Kim and Rudd set $Q = 1$. From now on, we will only refer to this model as binary encounter Bethe model (BEB) if this approximation is made. If Q is not set to 1 we should label it as BEQ to avoid confusion. To further simplify, Kim and Rudd used the Vriens Φ function in its asymptotic form, meaning that $\phi = 1$. The two approximations made above severely simplify the BEB expression and still provide cross sections that are very reliable in shape and magnitude, from the ionization threshold to several keV [10, 12, 13, 53, 54]. The role of the Vriens Φ function can be better understood if we plot the relative difference between the BEB model with $\phi = 1$, and the same model without the said simplification [Eq. (2.32)], which we will call binary encounter Bethe-Vriens BEBV model.

In Fig. 2.3 we can see that for low binding energies, of the order of the Rydberg constant, we can get discrepancies up to 15%. This effect should be important when calculating cross

sections for the ionization of outer-shells of alkaline metals, but as a rule should always be inserted for total ionization cross section computations.

The total ionization cross section (TICS) for a given sub-shell in the BEB(Q) model is then obtained by integrating Eqs. (2.66) and (2.67) from $w = 0$ to $w = (t - 1)/2$, and the final expression is given by

$$\sigma_{BEB(Q)} = \frac{S}{t + u + 1} \left[\frac{1}{2} Q \left(1 - \frac{1}{t^2} \right) \ln t + (2 - Q) \left(\left(1 - \frac{1}{t} \right) - \frac{\ln t}{t + 1} \right) \right], \quad (2.68)$$

where once again the reduced units are

$$
\begin{aligned}
t &= T/B, \\
w &= W/B, \\
u &= U/B, \\
S &= 4\pi a_0^2 N (R/B)^2.
\end{aligned}
\quad (2.69)
$$
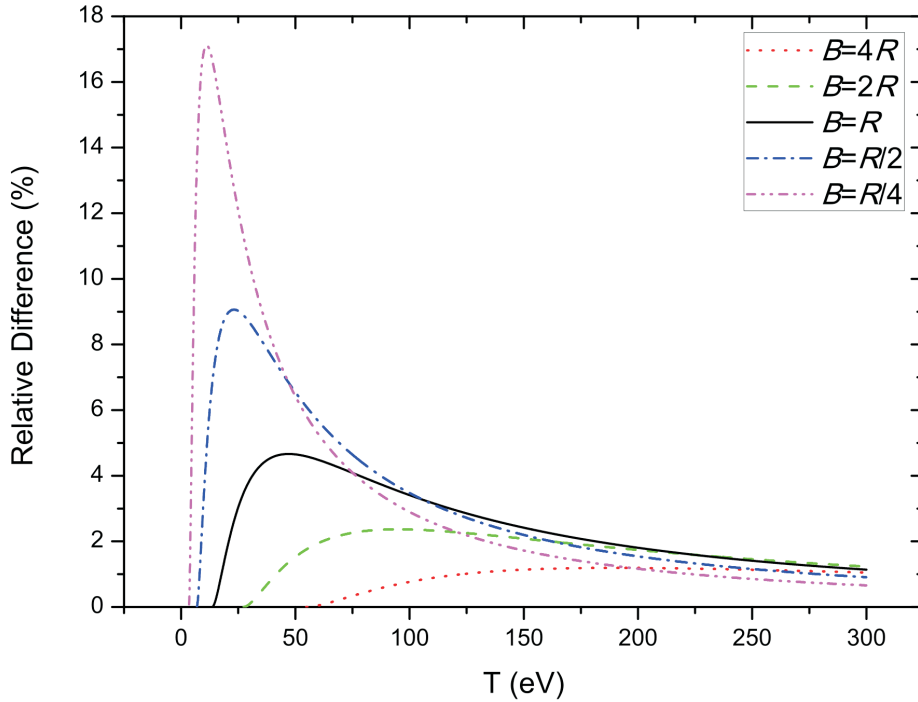
Figure 2.3: Plot of the ratio of the difference between the BEBV and BEB model to the BEB cross section. The starting point of each curve corresponds to $T = B$

2.7 Relativistic binary encounter Bethe (RBEB) model

In the derivations above, as well as in the original derivations of Mott and Bethe, all non-relativistic energy values were obtained from the velocities of the primary and secondary electrons. All quantities, such as the momentum transfers and binding energies have been obtained in the non-relativistic regime through $K = mv^2/2$ where v is the speed of an electron and m its mass. On the other hand, in relativistic formulas, these quantities are written

as ratios of the electron speed to the speed of light. Taking into account the Lorentz transformations and the specific energy values used in the BEB model, we get a set of relativistic energy terms which will be used to change the BEB expression accordingly,

$$\beta_t = \frac{v_t}{c}, \qquad \beta_t^2 = 1 - \frac{1}{(1+t')^2}, \qquad t' = \frac{T}{mc^2}, \tag{2.70}$$

$$\beta_b = \frac{v_b}{c}, \qquad \beta_b^2 = 1 - \frac{1}{(1+b')^2}, \qquad b' = \frac{B}{mc^2}, \tag{2.71}$$

$$\beta_u = \frac{v_u}{c}, \qquad \beta_u^2 = 1 - \frac{1}{(1+u')^2}, \qquad u' = \frac{U}{mc^2}, \tag{2.72}$$

where v_t is the speed of an electron with kinetic energy T, v_b is the speed of an electron with kinetic energy B and v_u is the speed of an electron with kinetic energy U. Applying this transformations on Eq. (2.68), as can be seen on Ref. [14], results in the TICS for the relativistic binary encounter Bethe (RBEB) model, Eq. (2.73). Each term has its origin on the relativistic version of the Mott and Bethe cross sections, and a similar treatment to what was performed for the BEB expression, which will not be shown here, was done in order to achieve the final RBEB expression [10].

$$\sigma_{\text{RBEB}} = \frac{4\pi a_0^2 \alpha^4 N}{\left(\beta_t^2 + \beta_u^2 + \beta_b^2\right) 2b'} \left[\frac{1}{2} \left(\ln\left(\frac{\beta_t^2}{1-\beta_t^2}\right) - \beta_t^2 - \ln\left(2b'\right) \right) \left(1 - \frac{1}{t^2} \right) \right.$$
$$\left. + 1 - \frac{1}{t} - \frac{\ln t}{t+1} \frac{1+2t'}{\left(1+\frac{t'}{2}\right)^2} + \frac{b'^2}{\left(1+\frac{t'}{2}\right)^2} \frac{t-1}{2} \right]. \tag{2.73}$$

As can be readily seen, the relativistic Eq. (2.73) reduce to its non-relativistic counterpart, Eq. (2.68) in the limit $\beta_t \ll 1$ by noting that

$$R = \frac{mc^2\alpha^2}{2},$$
$$T \cong \frac{mv_t^2}{2},$$
$$U \cong \frac{mv_u^2}{2},$$
$$B \cong \frac{mv_b^2}{2}. \tag{2.74}$$

2.8 Considerations on the binary encounter Bethe models

Cross sections based on the Bethe theory, are normally very reliable for high T mainly because of the correct asymptotic behaviour that is not present in other classical theories, such as Gryzinski's [21, 55–57] and further models which were based on Gryzinski's such as Quarles's [58], Deutsch's [59] and Vriens's [22–24, 47] models. These classical theories, however, tend to provide reliable cross sections in the low energy regime. Since the BEB/RBEB models combine the classical binary encounter model at low T with the leading dipole term of Bethe's theory at high T and since the RBEB model reduces to the correct non-relativistic BEB model at low energies, we expect the RBEB model to provide reliable ionization cross sections for a very wide range of T, thus making it ideally suited for modelling ionization events that cover incident electron energies from the threshold to several MeV, such as those occurring in plasmas.

The most noticeable relativistic effect, which is known as the relativistic rise since it raises the cross section at high energies $T > mc^2$ sometimes to values higher than the peak itself, is very well described by the RBEB model. Other relativistic effects, which occur mainly at

energies much higher than mc^2, such as the density effect are not taken into account. The density effect is an apparent increase in the target density due to Lorentz contraction of the length in the direction of the incident electron beam.

The RBEB model is in very good agreement with experimental results [14, 15], as well as with relativistic plane wave Born approximation (RPWBA) calculations [60], although in the ultra-relativistic regime ($T > 1MeV$) it seems to overestimate the ionization cross section of inner-shells. This might be due to the fact that for inner-shell ionization the RBEB model overestimates the M_i^2 term, which is a weighted integral of the differential oscillator strength. This shortcoming could be corrected by actually calculating this term with a suitable relativistic continuum wave function, although this quantity is not very easily obtained. Nevertheless, even in the BEB approximation, $Q = 1$, the cross sections are very reliable for a very wide range of energies.

In Fig. 2.4 we can see the contribution of the different approximations made in the BEB model with respect to the BED and BEQ expressions. We conclude that the approximations, which were performed for the asymptotic regime, hold very well in the low T region. At this point the experimental uncertainties do not allow us to choose one theory instead of another.
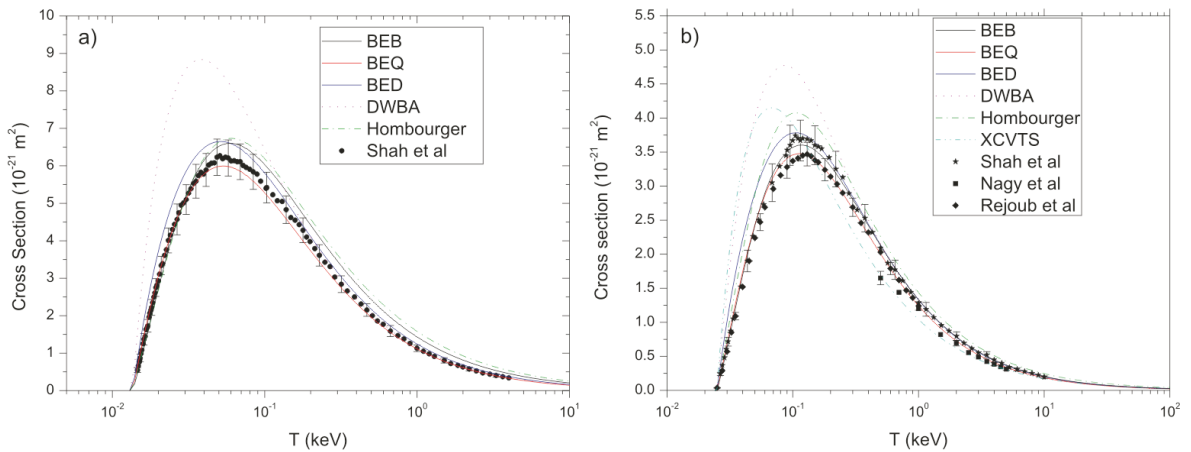
Figure 2.4: Comparison of the BED model with BEQ and BEB models for the calculation of electron impact ionization cross sections for a) hydrogen and b) helium. Experimental results are taken from Refs. [61–64]

We should note, however, that the "'Burgess-Vriens"' denominator, $T + U + B$ is the only *ad hoc* term inserted without proper derivation in the BED and BEB/RBEB models, and application to diverse atomic targets suggests that the role of this term should be further investigated. The substantial reduction of cross sections at low T achieved with the use of the Burgess-Vriens denominator for neutral targets is unlikely to be correct in magnitude, as concluded by Kim and Vriens, when the incident electron is subject to a long-range Coulomb interaction from an ion target. Also, application to K-shell ionization showed that, even for neutral targets, the denominator would reduce the cross section too much, probably because of the distortion of the wave functions in the presence of the incident electron, as well as the polarization of the target.

Scaling Rules of Binary Encounter Cross Sections

3.1 Scaling factors of the BEB model

In this section we will address mainly the role that the Burgess-Vriens denominator plays on the correct calculation of atomic targets. A thorough Pareto-type analysis was performed for every other term in the BEB theory in order to check the contribution of the different terms to the overall cross section. The first thing investigated was the contribution of the correlation of the bound electrons on the target. Although the binding energy values can be usually obtained from experiments, the kinetic energy of the bound electrons are normally calculated using Hartree-Fock or Dirac-Fock codes. In this work, we used almost exclusively the multiconfiguration Dirac-Fock general matrix elements, MCDFGME, code developed J. P. Desclaux and P. Indelicato [50, 51] to calculate all atomic theoretical quantities. The binding and kinetic energy values of the bound electrons in the sub-shell to be ionized were calculated both in the monoconfiguration and the multiconfiguration modes with correlation orbitals with principal quantum number up to $n = 6$ for oxygen, sulphur, silver, gold and uranium. The change in energy between the monoconfiguration and the multiconfiguration modes resulted in a very small change in the cross section ($< 1\%$) at the cross section peak for this elements. In fact, deriving the BEB TICS with respect to U, we see that the slope is almost zero for T ranging from the ionization threshold to several keV. However, the cross section is much more sensible to changes in the binding energy. In the ionization peak, the relative change in intensity is almost linear with the relative change of the binding energy, changing up to 50% with a 35% change in B. Hence, since the energy values obtained with state-of-the-art electronic structure codes such as the one used in this work are accurate up to 1% or better, we do not expect these uncertainties to dominate the error budget. Another main source of error could arise from the differential dipole oscillator strength simplification. Fig. 2.4 already shows that the approximation seems to be quite good for low Z neutral elements. The $df(w)/dw$ functions can be obtained either from photoionization experiments or reliable theories, although the literature is quite scarce. However, since the differential oscillator strength is contained in the leading dipole term, and the Bethe theory describes the asymptotic region very well, we can compare the quantity M_i^2 with our theories. This could only be done due to the analytical nature of the BED/BEQ/BEB models. Lets recall that

$$M_{\text{Bethe}}^2 = \frac{R}{B} \int_0^\infty \frac{1}{w+1} \frac{df(w)}{dw} dw = \frac{NRQ}{2B}.$$

(3.1)

Table 3.1: Q values for hydrogen, helium and neon.

Element	subshell	Q
H	1s	0.4343
He	1s	0.8025
Ne	1s	0.8430
Ne	2s	0.3528
Ne	2p	1.1605

Both the M_{BED}^2 and M_{BEQ}^2 are similar to the one obtained by Bethe because of the approximation $Q = 1$ made in the BEB model,

$$M_{\mathrm{BEB}}^2 = \frac{NR}{2B}. \tag{3.2}$$

In Table 3.1, Q values for hydrogen, helium and neon are listed.

The fact that Q was set to 1 in the BEB model was not arbitrary. A survey of Q values showed that the order of magnitude involved was consistent with the choice, and from previous papers [10, 14] we know that the BEB cross section provides cross sections for low Z neutral atoms that are within $10 - 15\%$ of the ones obtained in the BED formalism. The apparent erratic behaviour of the differential oscillator strength for medium to high Z elements did not enabled us to find a function that could provide a better simplification than the one made by Kim and Rudd.

The term that remains, $1/(T + U + B)$ is the only *ad hoc* term, inserted without proper derivation in the three models, the Burgess-Vriens denominator. This term reflects the scaling method used to scale first-order PWBA electron impact excitation and ionization cross sections [65], and the original qualitative justification for it was that the "effective" incident energy seen by the incoming electron is T plus the potential energy of the target electron. The choice to insert this denominator originated from the symmetric form of the binary encounter theory [47]. The resultant reduction of the cross section is a desired effect since most collision theories overestimate the cross section near the peak. Much of the sucess of the BEB model for neutral low Z targets can be attributed to this denominator.

In the early days of the model, Kim and Rudd [10] noticed that they had to reduce the denominator to apply the non-relativistic BEB to the ion He$^+$. Also, several applications of the BEB to singly charged ions revealed that the use of $T + (U + B)/2$ instead of $T + U + B$ resulted in better agreement with experimental data [53]. Moreover, comparisons to distorted-wave Born cross sections [66] and experimental data [15] suggested that a simple average of the BEB cross sections with $T + U + B$ denominator and T reproduces the theoretical and experimental K-shell ionization cross section data at low to intermediate Z values. For L- and M-shell ionization of heavy atoms, the classical denominator T is actually the most suited. For sub-shells with large angular momentum of heavy neutral atoms, another "fine tuning" of the Burgess-Vriens denominator was needed [14], and the denominator $T + U + B$ was replaced by $T + (U + B)/n$, where n corresponds to the principal quantum number of the sub-shell being ionized. The reason was to avoid excessive reduction of the cross sections due to large values of U for outer orbitals, resulting from many radial nodes and high quantum numbers in the kinetic energy operator $\ell(\ell + 1)/2r^2$.

In Table 3.2 the denominators commonly used as scaling factors in the binary encounter theory are listed and their domain of applicability is shown.

The existence of such a range of different scaling factors, lead to a necessity in understanding the role of the Burgess-Vriens denominator in the BED/BEB model. In the succeeding years after the model development, Kim and co-workers failed in finding an explanation for

Table 3.2: Scaling factors used in the binary encounter theory.

Type	Denominator	Applications
Classical	$\frac{1}{T}$	L- and M-shells, highly charged ions
Burgess	$\frac{1}{T+B}$	He$^+$, Li^{2+}, outer-shells of neutral atoms
Vriens	$\frac{1}{T+B+U}$	H, He and mostly neutral targets
Kim (average)	$\frac{1}{2}\left(\frac{1}{T} + \frac{1}{T+B+U}\right)$	K-shell of low to intermediate Z elements
Kim (ions)	$\frac{1}{T+(B+U)/m}$	lowly charged ions (m = charge state)

the denominators variation, although it was well known that it was related to the shielding of the nuclear charge as seen by the incident electron. Moreover, the analysis of the results obtained by Santos *et al.* [15] shows that there is a hidden Z dependence on the correct value of the denominator which cannot be accurately described by the scaling of either the binding energy and/or the kinetic energy of the target electron.

3.2 X-Type scaling

In this work, we propose a different scaling for the BEB/RBEB models, in which, instead of using the denominator $T + U + B$, we adopt the denominator $T + X$, following the work done by Kim [65] for electron impact excitation. As described in the mentioned reference, the X constant should be related somehow to the shielding of the nuclear charge by the bound electrons of the target atom and has units of energy.

Although this type of scaling has been inserted in several theories such as the PWBA [65], its success remains to be explained, even though it is an excellent way to account for the electron exchange, distortion and polarization effects that are absent in the first-order PWBA.

The X-type scaling is in agreement with the original Burgess papers [67, 68], in which the constant X was equivalent to the binding energy B since it represents the energy gain of the incident electron by travelling from outside the atom to the vicinity of the target electron inside the atomic cloud.

Although, Vriens noted that the Burgess assumption was not correct since the effective potential seen by the incident electron was higher than the binding energy. This happens due to the fact that the bound electron has a non zero kinetic energy, and a corresponding centrifugal term that lowers the binding energy. In hydrogen, for instance, the correct potential energy of the bound electron is $-|U + B|$. However, when analysing a multielectronic atom, we conclude that both the Burguess and Vriens assumption is not correct for every sub-shell essentially because of correlation and the complex orbital motion (on a purely classical viewpoint) of the bound electrons; it is an simplified way of describing the overall work required to bring an electron from infinity to the region where the binary encounter occurs.

Considering the electrostatic interaction between the incident and target electrons, we may calculate this effect by looking at the atomic electrons as a space charge distribution, given by

$$Q_{n,\ell}(r) = e \ |\psi_{n,\ell}(r)|^2, \tag{3.3}$$

where e is the electron's charge, and $\psi_{n,\ell}(r)$ are the normalized radial wavefunctions of the target electrons in the sub-shells labelled by the principal quantum number n and the orbital quantum number ℓ.

Accordingly, the work required to bring an electron from infinity to a distance R from the nucleus is given by the sum of all contributions from the charge distributions of every single orbital plus the nuclear potential. Thus, the parameter X, which is a function of R and Z,

is given by

$$X(Z,R) = \frac{Ze^2}{R} + \sum_{n=1}^{N_{total}} \sum_{l=0}^{n-1} \int_0^\pi \int_0^{2\pi} \int_0^\infty \frac{e^2 |\psi_{n,l}(r)|^2}{|\mathbf{R} - \mathbf{r}|} r^2 \sin\theta \; dr d\phi d\theta. \tag{3.4}$$

where, in spherical coordinates, $\mathbf{r} = \mathbf{r}\,(r\sin\theta\cos\phi; r\sin\theta\sin\phi; r\cos\theta)$ and $\mathbf{R} = \mathbf{R}\,(0;0;R)$. Since the impact parameter is absent from the binary encounter model, and only the energy gain of the incident electron is important in this framework, the collision was set as head-on with the direction of the $z-$ axis. This can be done with no accuracy compromise because the integral is independent of the path taken, depending only on the integration limits, which in this case are ∞ and R. After studies of convergence and final accuracy, the high limit of the integration was set to 100 a.u. since the potential at that distance is effectively zero, specially for neutral atoms. For highly charged ions the integration limit was set to 1000 a.u. because of the high range tail of the nuclear potential, compromising CPU time but not changing the overall accuracy.

After obtaining the $X(Z,R)$ function for a given atom, the distance R at which the ionization of a given sub-shell occurs is needed.

To our knowledge, there is no study of the parameter corresponding to the necessary overlap between the incident and target electron's wavefunction to allow ionization in binary encounter-type models.

An educated guess could be obtained by calculating the distance corresponding to the maximum of the probability distribution of the target electron, i.e. the radius of the classical orbit in the Bohr model of the atom, although it is somewhat intuitive that the direct ionization does not require such high overlap between the incident and target electron's wavefunction. In Fig. 3.1 we can see the $X(Z,R)$ function for carbon, $Z = 6$. In the plot we have represented the nuclear potential and the effective potential seen by the incident electron, Eq. (3.4). The point corresponding to the crossing of the maximum of the $1s$ wavefunction and the binding energy, B, of the K-electrons of Carbon is represented, schematising the Burgess's assumption. The same is done for $B + U$ to represent the Burgess-Vriens denominator.

Bearing in mind the success of the BEB model with the average of $1/T$ and $1/(T+U+B)$ for K-shell ionization [15], BEB$_{average}$, a systematic study was performed for elements with $3 \le Z \le 92$, in which the BEB$_{average}$ cross section value at the peak was compared to the BEB model with the X-scaling, BEB$_X$, in order to obtain the distance $R = R_K$ at which the K-shell ionization cross section peaks for a given Z value.

The function $X(Z,R)$ was obtained by computing Eq. (3.4) for elements ranging from Lithium to Uranium, with Dirac-Fock wave functions calculated using the MCDFGME computer code developed by J. P. Desclaux and P. Indelicato [50, 51].

The code was used in the single-configuration mode, that is, no correlation orbitals were included in the wave function calculations. Details of the method can be found, for instance, in [69, 70].

The obtained results are represented in Fig. 3.2, where we can observe that the $R_K(Z)$ parameter follows an inverse power law, the same approximate behaviour as the maximum of the 1s and 2s probability densities.

The $X(Z,R)$ function, for $R = R_K$, is approximately given by

$$X(Z, R_K) = 0.203\, Z^{2.147}. \tag{3.5}$$

Looking at Eq. (3.5) and taking into account that the binding energy of the K-shell of neutral atoms (in a.u.) scales as [71]

$$\frac{B}{2R} = 0.212 Z^{2.1822}, \tag{3.6}$$

we can see the reason for the success of Burgess theory. In fact, only for the total ionization of very light atoms, the need for the Vriens modification of the denominator is really required.
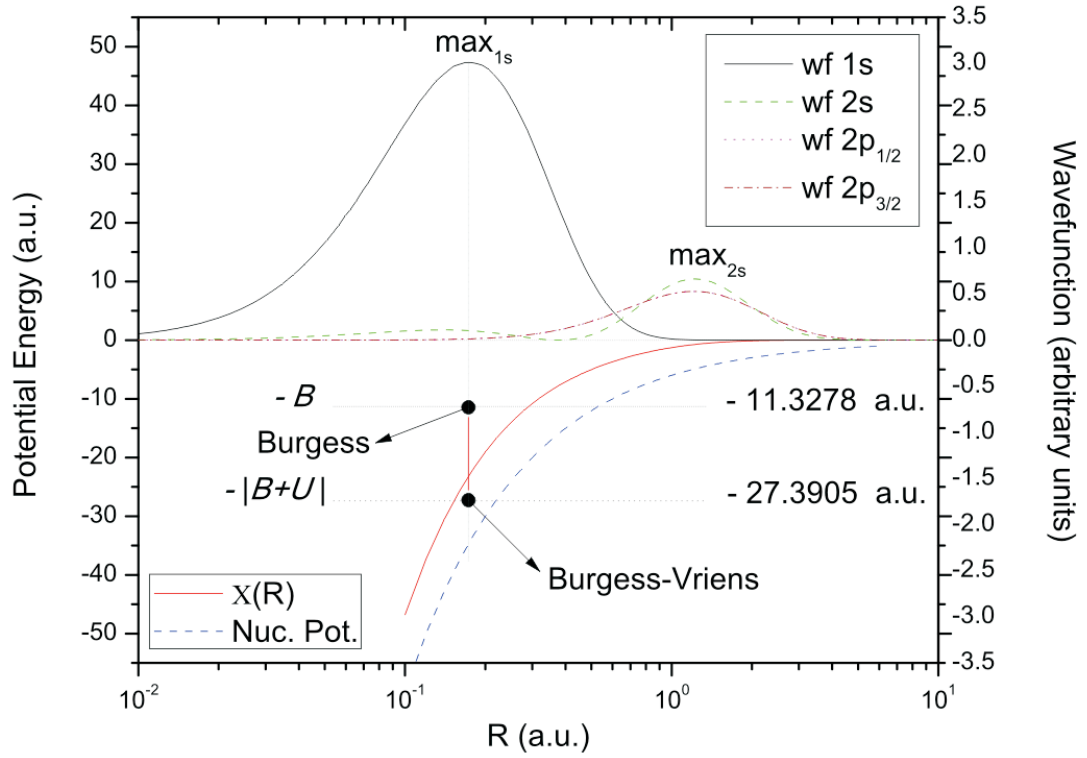
Figure 3.1: Nuclear and effective potential, $X(R)$, calculated with Eq. (3.4) for carbon. The spatial distribution of the electronic radial wavefunctions is also shown.

3.2.1   Binary encounter ionization region

In order to find the correct distance R at which the binary encounter occurs, we proceed in a similar fashion as in the previous section. Using experimental results near the ionization peak we iteratively scale the RBEB model with the new denominator so as to minimize the χ^2 and record the corresponding X value, which from Eq. (3.4) translates to a specific R_K value. We then repeat the process for the entire range of elements. When the quotient between the R_K parameter and the R_{Max1s}, obtained with the MCDF code, is calculated, it can be seen in Fig. 3.3 that the binary encounter occurs at increasing relative distances from the maximum of the $1s$ distribution as the atomic number is increased. For Lithium, the binary encounter region is already at approximately 1.5 times the maximum of the 1s wavefunction and extends up to 3 times for Uranium.

Considering the form of the $X(Z)$ function in Eq. (3.5), and that the binding energy of the K-shell electrons in neutral atoms (in a.u.) scales as $0.4240Z^{2.1822}$ (Casnati *et al.* [71]), we see that $X(Z)$ has an almost quadratic form.

Therefore, as a first approximation, we can adopt $X(Z)$ to be equal to the hydrogenic energy levels expression, i.e., $X(Z) = Z_{\text{eff}}^2/(2n^2)$, where n the principal quantum number, and Z_{eff} is the effective nuclear charge that accounts for the electronic shielding and electronic correlation. In the cases where the Z_{eff} is not known, we may use the well-known approximation [Eq. (3.7)] that considers the effective nuclear charge to be given by the atomic number
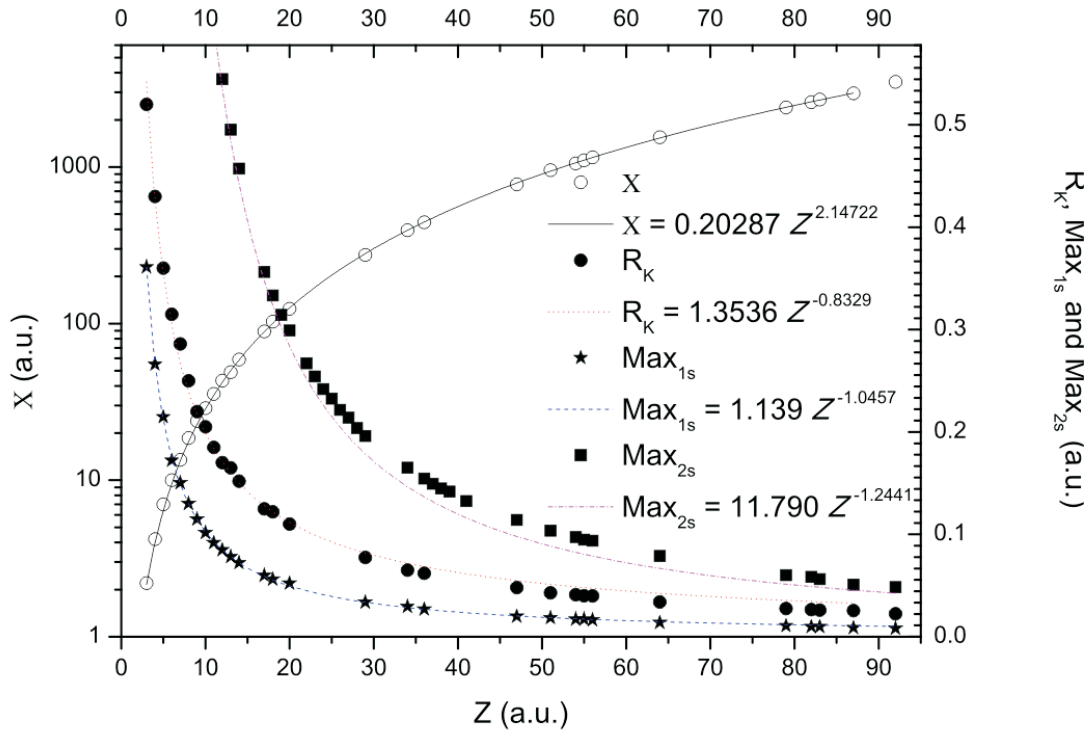
Figure 3.2: Variation of parameters X and R_K for K-shell ionization of atoms with atomic number $3 \leq Z \leq 79$ obtained by comparing the X-type scaling BEB/RBEB model with the averaged denominator BEB/RBEB model.

minus the inner electrons up to the sub-shell being ionized.

$$Z_{\text{eff}}(n\ell j) = Z - \sum_{i=1s1/2}^{n\ell j} N_i. \tag{3.7}$$

where Z is the target atomic number and N_i is the number of electrons of the subshell i. Moreover, based on the results from Figs. 3.3 and 3.2, in order to emulate the energy change of the incident electron when it penetrates the electronic cloud, we assume a linear combination of the consecutive corresponding sub-shell hydrogen-like energy levels for the function $X(Z)$. Although the correct Z dependence cannot, until now, be derived from first principles, the functional behaviour of Eq. (3.8) should describe fairly well the scaling of the X function for a wide range of Z values. Thus, the X function, in atomic units, can be written as

$$X_{n\ell j}(Z) = a\frac{Z_{\text{eff},n\ell j}^2}{2n^2} + b\frac{Z_{\text{eff},n'\ell'j'}^2}{2n'^2}, \tag{3.8}$$

where a and b are constants and $n'\ell'j'$ stands for next subshell after the subshell $n\ell j..$ In order to assess the correct values for the a and b coefficients, we used the experimental values of the R_K calculations and the theoretical calculations for the maximum of the probability distribution of the $1s$ and $2s$ wavefunctions across the Z spectra from carbon to uranium. To find the values of the coefficients a and b, we plotted the relative distance between the R_K and the maxima of the $1s$ and $2s$ wavefunctions in the following way

$$R_{K_{\text{rel1s}}} = \frac{R_K - \text{max}_{1s}}{\text{max}_{2s} - \text{max}_{1s}}. \tag{3.9}$$
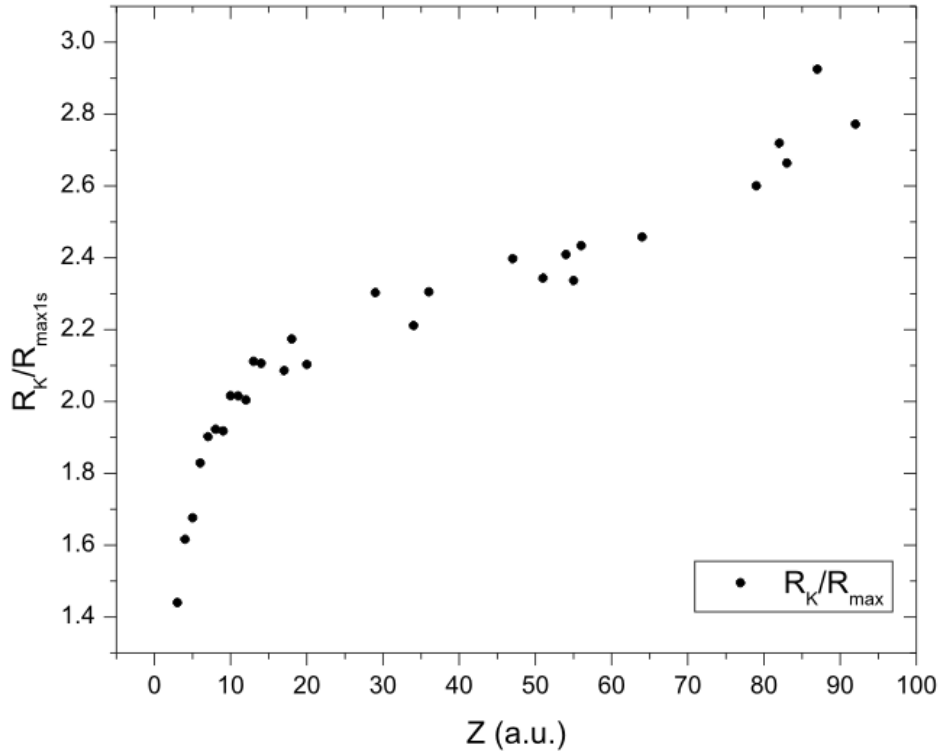
Figure 3.3: Quotient between the binary encounter region for k-shell ionization and the maximum of the 1s probability distribution.

Thus, since the collision region for K-shell ionization is always between the two shells the coefficients are always restricted to the rule $a + b = 1$. An analysis of the results shown in Fig. 3.4 leads to the use of $a = 0.3$ and $b = 0.7$. We can see that for elements lighter than argon, the penetration of the atomic cloud is more pronounced. This might be due to the fact that for lighter atoms, the K-shell is much less contracted, thus requiring the incident electron to penetrate deeper to a region where the probability of finding the $1s$ electron is higher. The contraction of inner-shells for high-Z atoms on the other hand moves the binary encounter region to the tail of the probability distribution. In this case, although for heavy atoms the binary encounter occurs much closer to the nucleus, the relative distance to the maximum of the $1s$ wavefunction increases.

Although this hypothesis was proposed for K-shell ionization, there is no reason *a priori* for it not to work for other sub-shells. For L-shell ionization we expect the same behaviour presented in Fig. 3.4, although somewhat shifted to the high-Z end of the graph. The lack of experimental L-shell electron impact ionization cross sections near the ionization peak for low- to medium-Z elements prevents us from effectively evaluating the behaviour. The model was tested for K-, L- and M-shells of neutral targets and later used on all shells of several ions. We have used the coefficients obtained from Fig. 3.4 in all shells apart from the last occupied shell for total ionization of ions since there is no orbital above it for the linear combination of Eq. (3.8) When applying this scaling factor for calculations of total ionization, the scaling factor $X_{n\ell j}(Z)$ for the last occupied sub-shell should be written as

$$X_{n\ell j}(Z) = \frac{Z_{\text{eff},n\ell j}^2}{2n^2}, \tag{3.10}$$
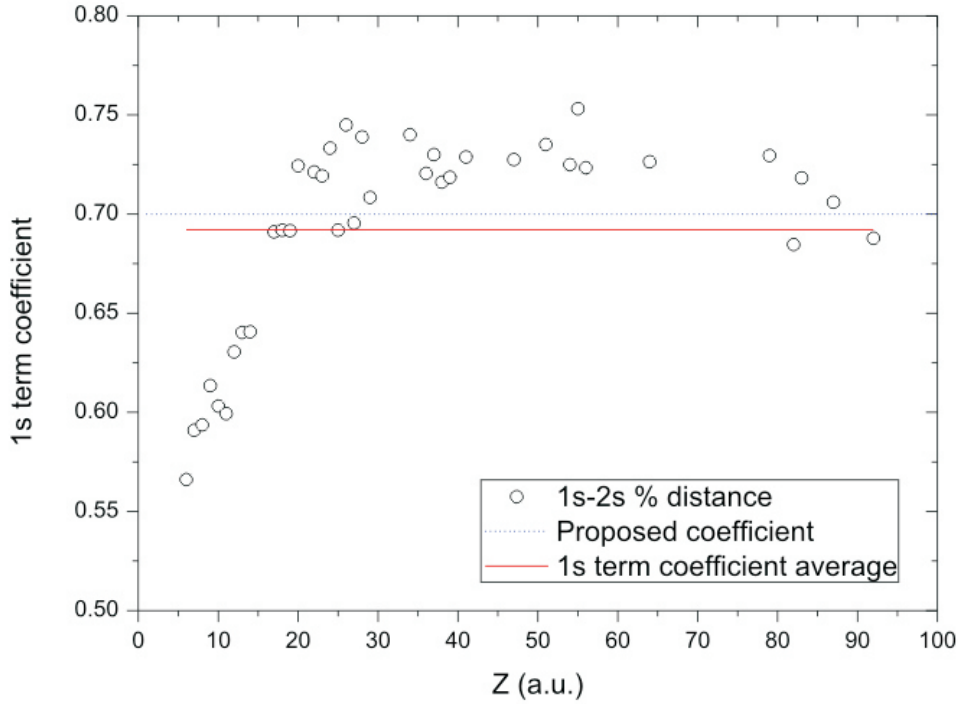
Figure 3.4: Coefficient of the 1s term in the linear combination of energy levels of Eq. (3.8).

meaning that for the outer shells the penetration of the incident electron upon ionization, in this model, is much higher than for inner-shells as expected if the hypothesis given above for the behaviour of Fig. 3.4 is correct. Application of this scaling factor in the BEB formalism shows very good agreement for both inner-shell and total ionization cross sections of atoms and ions, as is presented on Chapter 4.

3.3 Modified binary encounter Bethe (MBEB) model

Taking into account the scaling factor described above, and the derivation made in Chapter 2, specially Eq. (2.68) the total ionization cross section expression of the modified binary encounter Bethe model (MBEB), in reduced units, is written as [72]

$$\sigma_{\text{MBEB}} = \frac{S}{t + \chi} \left[\frac{1}{2} \left(1 - \frac{1}{t^2} \right) \ln t + \left(1 - \frac{1}{t} \right) - \frac{\ln t}{t + 1} \right], \tag{3.11}$$

where the reduced units are expressed as

$$
\begin{aligned}
t &= T/B, \\
\chi &= (X/B)2R, \\
S &= 4\pi a_0^2 N (R/B)^2. \tag{3.12}
\end{aligned}
$$

In Eq. (3.12), X is the scaling constant given by Eq. (3.8), N is the occupation number of the sub-shell to be ionized, a_0 is the Bohr's radius (5.29×10^{-11} m), and R is the Rydberg energy (13.6 eV).

The relativistic counterpart of the modified binary encounter Bethe model (MRBEB) reads

$$\sigma_{\text{MRBEB}} = \frac{4\pi a_0^2 \alpha^4 N}{(\beta_t^2 + \chi \beta_b^2)\, 2b'} \left\{ \frac{1}{2} \left[\ln \left(\frac{\beta_t^2}{1 - \beta_t^2} \right) - \beta_t^2 - \ln \left(2b' \right) \right] \times \right. \tag{3.13}$$

$$\times \left(1 - \frac{1}{t^2} \right) + 1 - \frac{1}{t} - \frac{\ln t}{t+1} \frac{1 + 2t'}{(1 + t'/2)^2} +$$

$$\left. + \frac{b'^2}{(1 + t'/2)^2} \frac{t-1}{2} \right\}$$

where

$$\beta_t^2 = 1 - \frac{1}{(1+t')^2} \qquad\qquad t' = T/mc^2,$$

$$\beta_b^2 = 1 - \frac{1}{(1+b')^2} \qquad\qquad b' = B/mc^2,$$

$$t = T/B \qquad\qquad\qquad \chi = (X/B)2R,$$

$$\tag{3.14}$$

and α is the fine structure constant, c is the speed of light in vacuum, and m is the electron mass. It is assumed that all the energy values are in the same units and a_0 is in the SI system. This expression is valid for all shells of elements with atomic number ranging from $Z = 3$ (Lithium) to $Z = 92$ (Uranium). In order to calculate total ionization cross sections for neutral elements or ions, we need only to sum the contributions from all active shells, hence

$$\sigma_{\text{Total}} = \sum_{\text{occupied } n\ell j} \sigma_{\text{M(R)BEB}, n\ell j}. \tag{3.15}$$

Chapter 4

Results

4.1 Electron impact ionization of inner-shells

The present MBEB/MRBEB models produce reliable cross sections between the threshold and the ionization peak without using any shell-dependent parameters.

As an illustration, we apply the non-relativistic MBEB and relativistic MRBEB expressions to the K-shell ionization of C, Ne, Si, Sc, Ti, V, Cr, Fe, Zn, Co, Sr, and Ag, to the L-shell ionization of Se, Kr, Ag, Sb, Xe, and Ba, and to the M-shell ionization of Pb and Bi.

Contrary to the BEB/RBEB models, which require two input parameters (B and U), the MBEB/MRBEB models require only the knowledge of one parameter, the binding energy B. For the binding energies of inner-shell electrons, one can use experimental values [73] to match experimental thresholds precisely, or theoretical binding energies from Dirac-Fock wave functions that are reliable to 1% or better in general. The values of B for the elements studied in this work are listed in Table 4.1. For the carbon atom the K-shell binding energy was taken from Ref. [74], while the remaining elements K-shell binding energies were obtained from Ref. [73]. The L- and M-shell binding energies were evaluated using the MDFGME code [50, 51].

The electron occupation number was set to $N = 2$ for full $s_{1/2}$ and $p_{1/2}$ orbitals, $N = 4$ for full $p_{3/2}$ and $d_{3/2}$ orbitals and $N = 6$ for full $d_{5/2}$ orbitals. The results presented here were published in [72].

4.1.1 K-shell ionization

On Fig. 4.1 (for C, Ne, Si, Sc, Ti, and V) and Fig. 4.2 (for Cr, Fe, Zn, Co, Sr and Ag), we compare the present MBEB [Eq. (3.11)] and MRBEB cross sections [Eq. (3.13)] to all available experimental data, to the empirical cross sections by Hombourger *et al*[75], Haque *et al*[37], and to the analytical model by Bote *et al.* [36], which results from a fit to a database of cross sections calculated using the plane-wave (PWBA) and distorted-wave (DWBA) Born approximations. For overvoltages ($t = T/B$) lower than 16, the fit was done to the DWBA database, and for $t > 16$ the PWBA database was used, since, for high-energies, the difference between the DWBA and PWBA cross sections is negligible. The DWBA/PWBA model, labelled solely as DWBA for simplicity, provides ionization cross section values that agree with those in the DWBA/PWBA database to within about 1%, except for projectiles with near-threshold energies. Since both the Hombourger *et al* model and the XCVTS model of Haque *et al* are empirical, the range of validity of such models is limited by the availability of experimental data. Furthermore, the XCVTS model uses a scaling term with different coefficients for different shells as in the unmodified BEB/RBEB expressions.

In the analysis of Figs. 4.1 and 4.2, as discussed previously by Santos *et al* [15], caution is

Table 4.1: Binding energy B values for the K-, L- and M-shells. The B value for C is from Ref. [74]. The remaining K-shell and L-shell B values are from Ref. [73]. The M-shell binding energies were evaluated using the MDFGME code [50, 51]

Element	B(eV)								
	K-Shell	L-shell			M-shell				
		L1	L2	L3	M1	M2	M3	M4	M5
C	296.07								
Ne	866.90								
Si	1840.05								
Sc	4489.37								
Ti	4964.58								
V	5463.76								
Cr	5989.02								
Fe	7110.75								
Co	7708.75								
Zn	9660.76								
Se		1652.44	1474.72	1433.98					
Kr		1916.30	1729.66	1677.25					
Sr	16107.20								
Ag	25515.59	3807.34	3525.83	3350.96					
Sb		4698.44	4381.90	4132.33					
Xe		5452.89	5103.83	4782.16					
Ba		5995.90	5623.29	5247.04					
Pb					3905.53	3601.14	3110.21	2628.17	2525.49
Bi					4056.25	3744.91	3223.11	2731.84	2623.08

warranted when comparing the experimental and theoretical data represented. Experimental data are mainly obtained through the detection of X-rays or Auger electrons emitted when bound electrons fill the K-shell vacancies created by electron impact. However, K-shell vacancies can be created not only by direct ionization but also by excitations of K electrons to unoccupied bound states. Since most theories, including the MBEB/MRBEB models, are designed for only direct ionization by electron impact, experimental data may exceed the theoretical data by the amount due to excitations of K electrons to bound levels. Therefore, unless experimental data have explicitly excluded the K-shell vacancies created by excitation, comparisons of theories and experiments may have an inherent ambiguity of $\sim 10\%$.

Below we discuss the cases that we analysed and that are shown in Figs. 4.1 and 4.2. In order to compare the experimental values to the different theoretical results, we calculated the reduced χ^2, Q, defined by

$$Q = \chi^2_{\text{red}} = \frac{1}{\nu} \sum_{i=1}^{N} \left(\frac{f_i - f_{\text{theo}}(x_i, A, x_0, w)}{\sigma_i} \right)^2 \tag{4.1}$$

where, $f(x_i)$ is the measured experimental data, $f_{\text{theo}}(x_i)$ ν is the theoretical data. σ_i is the variance of the observation and ν is the number of degrees of freedom, usually given by $N - n$, where N is the number of data points and n the number of fitted parameters, which in this case is 0 because we are not fitting the data points with our model but simply estimating if our model follows the experimental trend.

- Carbon: The relativistic and non-relativistic cross sections are almost identical for $T < 1$ keV. The present MRBEB cross section, the DWBA and the XCTVS results are in good agreement with the experimental data by Egerton *et al*[76], Tawara *et al*[77], and Isaacson *et al*[79] (with the reduced χ^2, Q, equal to 0.91, 0.65 and 0.73, respectively), while the experimental data by Hink *et al*[78] display an increasing trend toward lower T not seen in any other theory or experiment.

- Neon: The relativistic and non-relativistic cross sections are almost identical for $T <$ 100 keV. The theoretical cross sections are in fairly good agreement with experimental data by Tawara *et al*[77], Glupe *et al*[80], and Platten *et al*[81].

- Silicon: We see the beginning of the relativistic rise at $T > 100$ keV, which is not followed by the non-relativistic MBEB. In this high T region, all theoretical relativistic data agree with the experimental data by Ishii *et al*[82] and Shchagin *et al*[85], with Q values from 0.4 (Hombourger) to 0.7 (DWBA).

- Scandium: The experimental results by An *et al.* [88] are not in agreement with any of the theories presented here, so new experimental data are required to better understand this case.

- Titanium: The experiments are divided into two groups. The experimental cross sections by Jessenberger *et al.* [87] lie above all theoretical data in the peak region, while the experimental cross sections by He *et al.* [86] are lower than all theoretical data.

- Vanadium: The MRBEB cross section values for vanadium are in good agreement with the experimental data by An *et al.* [88], having the lowest Q value of all theoretical models, which ranges from 20.9 to 130.5.

- Chromium: We notice that all experimental data except the one from He *et al.* [86] for chromium agree with the represented theoretical models, confirming the trend of the experimental data by He *et al.* observed in Ti.

- Iron: Although there is a general agreement between the theoretical data and the experimental results, the MRBEB model underestimates slightly the ionization cross sections in the peak region.

- Zinc: The MRBEB cross sections are in good agreement with the experimental data by Tang *et al.* [93] at low T, and with the only experimental value at high T from Ishii *et al.* [82]. This is confirmed by the low Q value of 1.1 that we find, to be compared to the high value of 18.3 for the XCVTS model. Nevertheless, the MRBEB values become larger than the other three theoretical cross section values beyond $T = 1$ MeV. There is thus a strong need of new experiment for $T > 1$ MeV is desirable to distinguish different predictions from different theories.

- Cobalt: The experimental data by An *et al.* [94] agree very well with the MRBEB model, from threshold to the ionization peak, which produces the lowest Q value of all models in a range from 0.2 to 10.6.

- Strontium: The theoretical data disagree among them and with the experimental data. However, we observe that the MRBEB model (Q=3.2) follows more closely the experimental data by Shevelko *et al.* [95] at low T, while the DWBA (Q=6.3) and the Hombourger (Q=10.0) models follow more closely the experimental data by Middleman *et al.* [96] at high T.

- Silver: Ten sets of experimental data are compared with the MRBEB cross sections and other theories. Again, experiments are divided into groups near the peak. The experimental data by Davis *et al.* [97] agree well with the Hombourger cross sections. The experimental data by Schneider *et al.* [98], Kiss *et al.* [101], Hoffman *et al.* [84] agree with the MRBEB cross sections. The data by el Nasr *et al.* [103] and Hubner *et al.* [104] disagree with all the presented theoretical cross sections. Although all theoretical cross sections agree in the vicinity of $T = 500$ keV, the difference between the present MRBEB cross section values and the other theoretical relativistic cross section values

is widening at $T = 1$ MeV, amplifying the trend observed in Zn and Sr. The silver atom is another example for which definitive measurements would help to distinguish different theories.

4.1.2   L- and M-shell ionization

In order to investigate the range of applicability of the approach presented in this work besides the K-shell ionization, we have also applied the MBEB and MRBEB models to the L-shell ionization of Se, Kr, Ag, Sb, Xe and Ba, and to M-shell ionization of Pb and Bi.

On Fig. 4.3 and Fig. 4.4 the MBEB and MRBEB cross sections for the L- shell (for Se, Kr, Ag, Sb, Xe, and Ba) and M-shell (for Pb and Bi), respectively, are displayed as well as the theoretical results obtained with the DWBA, XCVTS and Lotz [26, 106] models, and by Scofield [60], and the experimental available data for the analysed elements.

The Lotz empirical expression, proposed more than 30 years ago, is one of the most successful formulas for calculating total direct ionization of any given state.

Concerning the L-Shell ionization, we notice that the MRBEB cross sections are in good agreement with the experimental data for the analysed elements, except Xe, having the lowest Q value for Se, Kr, Sb and Ba (1.2, 0.6, 0.5, 0.6, respectively), and the second lowest for Ag (1.4). The theoretical data disagree among them, namely in the peak region; the DWBA values produce the highest peak, followed in equal ground by the XCVTS and the Lotz curves, and finally by the MBEB and MRBEB curves. It should be pointed out that the experimental data by Hippler *et al.* [107] for Xe exhibits the greater uncertainty (about 30%) among the studied cases. This uncertainty is less than 17% for the other elements. The experimental data for the M-shell ionization is scarce and exist only for high incident electron energies, in the relativistic regime ($T > 10^4$ keV). In this high region, all theoretical relativistic data agree with the experimental data by Ishii *et al.* [82] and Hoffman *et al.* [84], with Q values equal to 0.4 (XCVTs), 0.7 (MRBEB), and 1.7 (DWBA) for Pb, and 0.3 (XCVTs), 0.9 (MRBEB), and 2.0 (DWBA) for Bi. The comparison among the theoretical data have the same outcome obtained for the L-Shell, showing that to a certain degree the goal of obtaining a parameter-free, shell-independent, analytical expression for the calculation of EICS was fulfilled.

4.2   Electron impact total ionization of highly charged ions

As described in Chapter 3, the scaling of the BEB theory had to be changed in order to apply it to ionized systems, and the choice of denominators was not obvious. Although the scaling term proposed in this thesis was calculated for inner-shell ionization of neutral atoms, the key physical aspects are still valid and there is no reason *a priori* not to apply the model to ions of all charge states. Hence, in this work the we deal mainly with the results obtained for the total ionization of Kr ions in a wide range of charge states. Calculations of the distribution of atoms over all ionization stages and quantum states is one of the key steps in modeling astrophysical and laboratory plasmas. Krypton is an ubiquitous element in plasmas, from controlled fusion to ECR ion sources, which is used either as a main gas or as a tool for ion density diagnostics. Consequently, a great amount of work has been done in studying the excitation and ionization of this element and its ions, both theoretically and experimentally.

Electron impact ionization cross sections of several ionization stages of Kr have been experimentally obtained by several groups. For neutral Kr see for example [109–111], for Kr^+, Kr^{2+}, and Kr^{3+} see [112], for Kr^{4+}, Kr^{5+}, Kr^{7+} see [113], for Kr^{8+} see [114], and for Kr^{10+} and Kr^{11+} see [115]. It should be mentioned that the Kr^{8+} measurements were strongly affected by ionization from metastable states in the first excited configuration. Recently, ionization cross sections for Kr^{12+} through to Kr^{18+} were measured by Khouilid *et al* [116]

using an animated crossed-beams method.

The Kr^{14+}, Kr^{16+} and Kr^{18+} results show presence of metastable ions in the primary ions beam. Theoretically, all these ions were studied in the configuration-averaged distorted-wave (CADW) level by Loch *et al* [117], and Coulomb-Born calculations using the "ATOM" code [118] were performed for ions ranging from Kr^{10+} to Kr^{18+}.

Although there are no experimental data for charge states higher than Kr^{18+}, some theoretical studies were made. Chen and Reed [119] carried out fully relativistic distorted-wave calculations for the ionization of Kr^{24+} and Kr^{25+}, including contributions from both resonant excitation and excitation-autoionization. Badnell and Pindzola [120] calculated level to level distorted-wave calculations for the ionization, including contributions from both resonant excitation and excitation-autoionization of Kr^{30+}, Kr^{31+}, and Kr^{32+}. Loch *et al* [117] also carried out CADW calculations for Kr^{24+} and Kr^{25+} and obtained single-ionization rate coefficients from the ground state of Kr^{33+}. High level calculations like R-matrix with pseudostates, convergent close coupling and time dependent close coupling methods have only been applied in calculating direct ionization cross sections for ions with only one or two active electrons. For the calculation of excitation-autoionization contributions to the total cross section, which becomes important for moderately high ionization stages, level-to-level multiconfiguration, configuration averaged distorted wave and R-matrix methods have been employed [121].

In X-ray spectroscopy analysis of plasmas there is a need for large amounts of high quality cross sections for the ionization processes involved in the plasma, namely the K-shell direct ionization [8, 9, 122]. Given the analytical nature of the MRBEB model, which has been shown to provide accurate electron impact cross sections for inner-shell ionization for a wide range of neutral elements and energies [72], we investigate in this work how the MRBEB [Eq. (3.13)] performs for highly charged ions. Taking into account the plasma diagnosis tools, and comparing to other analytical methods, a 20% or less uncertainty is enough so that the contribution to the final error budget is not dominated by the cross section calculation with the MRBEB model. The widely used Lotz expression, and other empirical theories, are not ideally suited for this since they often have different coefficients or even expressions for different elements, shells and/or charge states. Also, in some atomic systems, they show more than a 20% disagreement with experimental data.

Because we want to study the applicability of the MRBEB model from lowly to highly charged ions across the Z spectra, emphasis is given not only to ionization of Kr but also to Ar and Fe isonuclear series. We have chosen Ar and Fe for this work because of their importance in fusion, astrophysical and industrial plasmas [123–125]. In magnetic confinement fusion, Ar, along with Kr, is a species of choice for the modification of edge conditions (via transport barriers etc) by radiative cooling and this has led to the decision by the fusion community to establish argon as a reference species [125]. In the astrophysical domain, high-resolution soft x-ray spectra of iron from solar flares have been observed for many years from SMM and YOKHOH satellites and, since 1999, the CHANDRA X-ray observatory as well. Hence, besides Kr, we have studied also the behaviour of the MRBEB model in Ar^{2+}, Ar^{3+}, Ar^{4+}, Ar^{5+}, Ar^{6+}, Ar^{7+}, Fe^{2+}, Fe^{5+}, Fe^{6+}, Fe^{9+}, Fe^{11+} and Fe^{13+}. Results for the direct ionization cross section were compared to the Lotz expression, the Hydrogenic Scaling (HS) model of Sampson *et al* [126] and the Distorted Wave Approximation (DWA) calculated with the GIPPER code of the Los Alamos National Laboratory [127].

The processes that play a major role in electron impact ionization cross sections of ions can be described by the following expressions

$$Kr^{q+} + e^- \longrightarrow Kr^{(q+1)+} + 2e^-,$$

$$Kr^{q+} + e^- \longrightarrow (Kr^{q+})^* + e^- \longrightarrow Kr^{(q+1)+} + 2e^-,$$
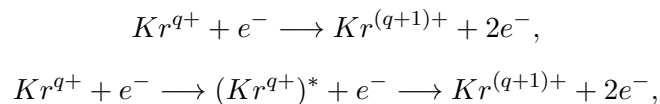
where q is the charge of the Kr ion to be ionized. The first process is called direct ionization

Table 4.2: Ground state configurations obtained from reference [73] and threshold energies for ionization and excitation-autoionization (EA) for Kr^+, Kr^{5+}, Kr^{6+}, Kr^{10+}, Kr^{15+} and Kr^{17+}. The binding energies (B) and excitation thresholds were evaluated using the MDFGME code [50, 51].

Ion	Ground State	B_{exp} (eV)	B_{th} (eV)	$n\ell$ $3d \to n\ell$			EA_{th}^{3d} (eV)
Kr^+	[Ar] $3d^{10}$ $4s^2$ $4p^5$	24.6	24.73	4p			79.46
Kr^{5+}	[Ar] $3d^{10}$ $4s^2$ $4p^1$	78.5	77.71	4p			90.06
Kr^{6+}	[Ar] $3d^{10}$ $4s^2$		107.20	4d			122.92

Ions	Ground State	B_{exp}	B_{th}	$3p \to n\ell$	$3s \to n\ell$	$2p \to n\ell$	EA_{exp}^{2p}	EA_{th}^{2p}
Kr^{10+}	[Ar] $3d^8$	314±3	313.83	4f	4s	3d	1750±25	1605.39
Kr^{15+}	[Ar] $3d^3$	542±3	543.63	8s	6s	3d	1645±5	1636.32
Kr^{17+}	[Ar] $3d^1$	637±5	641.18	9s	6s	3d	1655±5	1655.65

(DI), while the second corresponds to a process of excitation to a bound state followed by autoionization (EA). The later process can occur if the excitation energy is greater than the lowest ionization energy of the atom. For highly charged atoms, radiative stabilization can act to reduce the wheigt of the excitation-autoionization process on the total ionization cross section, which can be described by

$$(Kr^{q+})^* \longrightarrow Kr^{q+} + \gamma.$$

For the purpose of comparing our calculations with experimental data for ionization of ions, one must compute the contribution of the excitation-autoionization (EA) process to the ionization cross section. Excitation cross sections for transitions that result in autoionizing states were summed to the total ionization cross section calculated with the MRBEB model for Kr^+, Kr^{5+}, Kr^{6+}, Kr^{10+}, Kr^{15+} and Kr^{17+}, and compared with configuration averaged distorted wave calculations of Loch *et al* [117] and experimental data.

For the indirect process, described above, we have calculated the excitation cross sections using the averaged approximation (AA) method of Peek and Mann [128] with first order many body theory (FOMBT) for Kr^+, Kr^{5+}, Kr^{6+}, Kr^{10+}, Kr^{15+} and Kr^{17+}. The AA code uses target state wave functions from the Hartree-Fock atomic structure code of R.D. Cowan. To our knowledge, the dependence of the cross sections of neither the charge-state nor the atomic number have been systematically investigated for the ionization of medium to highly charged ions with binary-encounter models. The electron impact cross section data for such targets is incredibly scarce and when existent is almost impossible to deconvolute the direct ionization from all other indirect processes such as excitation-autoionization, radiative recombination and dielectronic recombination.

In order to compute the excitation-autoionization cross sections, a previous calculation of transitions with energies above the ionization threshold, had to be performed. The ground state configurations of each ionization stage of Kr were taken from ref. [129] and the MCD-FGME code developed by J. P. Desclaux and P. Indelicato [50, 51] was used to assess the possible transitions involved in the excitation-autoionization channels. The excited state calculations were performed in single configuration mode, hence no correlation was employed. For the cases studied, all of the thresholds for excitation-autoionization, apart from the 2p-3d transition in Kr^{10+}, agree with experimental data as shown in Table 4.2.

Three sets of data are shown on Figs. 4.5, 4.6 and 4.7, representing ionization cross sections for electron impact of Kr, Ar and Fe isonuclear series, respectively. Excitation-autoionization cross sections were summed to the direct terms for ionization in the Kr isonuclear series and compared to experimental and theoretical data, while for the Ar and Fe isonuclear series only the direct contribution was compared to other models.

4.2.1   Kr isonuclear series

Table 4.2 lists the ground state configuration of the Krypton ions presented in Fig. 4.5 as well as ionization and excitation thresholds. Autoionizing transitions are also presented for the six krypton ions analysed.

- Kr^+: The two experimental data sets for Kr^+ show good agreement between them up to the ionization peak at 60 eV. In that region the MRBEB+EA curve follows closely the rise of the cross section presented by all data points. Above that energy our calculation shows a better agreement with the data of Tinchert *et al.* The small bump in the peak of these data can't be assigned to any direct or indirect process in the collision. Excitations from both the 4s and 3d subshells were included in the EA calculation. The overall agreement for Kr^+ is quite good.

- Kr^{5+}: The experimental data shows non zero cross section values between 60 eV and the ground state ionization energy of 77.7 eV, calculated using the MCDF code. This is an indication of the presence of metastable states in the ion beam, possibly with the configuration $4s4p^2$. The discrepancies seen in the low energy end of the spectra can, therefore, be due to these metastable ions. For energies higher than 125 eV, our calculations tend to overestimate the cross section, when compared to the experimental data. At this stage, it is not conclusive if the direct ionization or the EA are responsible for this discrepancy.

- Kr^{6+}: Contributions from excitation-autoionizaton from the 3spd subshells were included in the calculation. The ionization cross section values for Kr^{6+}, calculated in this work, are in good agreement with the configuration averaged distorted wave calculation of Loch *et al* [117]. It can be seen that, for this charge state, the direct cross section calculated with our model is very similar to the direct contribution of the configuration averaged distorted wave calculation (CADW).

- Kr^{10+} and Kr^{15+}: Near the ionization threshold our values follow closely the experimental data, but for energies greater than 500 eV, approximately where the excitation series from the 3s subshell ends, the excitation-autoionization cannot account for the difference between the experimental data and the direct contribution of the MRBEB model. The bump in the cross section around 1618 eV, which derives from excitations of the 2p electron to the 3d subshell, can barely be seen in the spectra. At the ionization peak, the difference between experimental data and our values is about 20%. The analysis of the Kr^{15+} cross section shows some of the features also present in the Kr^{10+} figure. Near the ionization threshold, results are very similar to both the experimental data and the configuration averaged distorted wave values of Loch *et al.* For energies greater than 700 eV, both the direct term, which seems a bit skewed to the right, and the excitation-autoionization contribution seem to be underevaluated. Compared to the Lotz cross section, the MRBEB model shows a shallow rise which can in part be responsible for the underestimation of the total cross section. Although this case shows the greater discrepancy of all the cases studied, comparing our calculation to the distorted wave results instead of the experimental data, we obtain the same differences as in both the Kr^{10+} and Kr^{17+} ions.

- Kr^{17+}: The observed threshold for Kr^{17+} of 637 eV, from the data of Khouilid *et al*, is 4 eV below the 641 eV value calculated in this work. As can be seen in the EA curve in Fig. 4.5, excitations from the 3s and 3p orbitals to nℓ greater than 6 and 9, respectively, are present in the energy region from the threshold to approximately 750 eV. More than 100 autoionizing excitation cross sections were summed to the direct ionization cross section, from the 3s and 3p orbitals up to orbitals with principal quantum number 12. For

$n = 12$, the EA cross section is more than 4 orders of magnitude lower than the direct contribution. At an incident energy of 1655 eV, excitation followed by autoionization for 2p-3d, becomes extremely pronounced and at 1909 eV the 2s-3d EA is also observed. The 2p-3d experimental threshold of 1655 eV completely agrees with our calculation (see Table 4.2). The MRBEB cross section curve doesn't show such a steep rise as the Lotz empirical formula. That is the reason why, at energies below the cross section peak, the MRBEB+EA curve is lower than the experimental data. It can be also seen that, for energies greater than 3 keV, the MRBEB+EA curve overestimates the cross section. This might be linked to the fact that, for energies greater than 2.4 keV, the direct ionization of the 2p shell contributes to the double ionization of Kr^{17+}, thus lowering the EA cross section. This fact which was not taken into account in our calculation. The overall agreement is quite good, showing a maximum discrepancy of about 20% just before the 2p-3d threshold.

4.2.2 Ar isonuclear series

There is very good agreement between the Lotz, the HS and the MRBEB model for Ar^{2+}, although all three are consistently higher than the DWA peak. The slope of the HS cross section at energies just above the first threshold is higher than all other theories. The same behaviour is observed for Ar^{3+}, although the difference between the MRBEB and the DWA cross section is lower. Since the HS theory shows much skinnier peaks than the other theories, the $2p3/2$ threshold for Ar^{4+} is more pronounced than in the MRBEB, Lotz and DWA theories. The difference between the MRBEB and the DWA cross section values is less than 20%. For Ar^{5+} and Ar^{6+}, the MRBEB curve shows a similar behaviour as the Lotz curve. Both are higher than the DWA peak around 20%. Fig. 4.6 e), which represents the ionization cross section of Ar^{7+}, shows the best agreement between all curves. For this ion, the difference is less than 10% between the MRBEB theory and all the others.

4.2.3 Fe isonuclear series

For Fe^{2+} there is a very good agreement between all theories apart from the hydrogen scaling which sits 35% above the MRBEB curve around the ionization peak. The MRBEB and Lotz cross section are very similar for Fe^{5+}, although they seem to be underestimated when compared to the DWA and HS cross sections by about 12%. The same behaviour is observed for Fe^{6+}. The slope of the cross section just above the ionization threshold is lower in the MRBEB than in all other theories. Regarding the ionization cross section values of Fe^{9+}, there is a very good agreement between the MRBEB, DWA and Lotz cross section, with the HS cross section peak 13% above the MRBEB theory. For electron energies above 100 keV the relativistic rise can be already seen. The height of the ionization cross section peak for Fe^{11+} seems to be very well described by the MRBEB theory, although the rise of the cross section up to the peak is slower than in the three other theories. For Fe^{13+} all four theories presented agree very well with each other except in the high energy region where the relativistic effects are already important.

Figure 4.1: Electron impact K-shell ionization cross sections for (a) C, (b) Ne, (c) Si, (d) Sc, (e) Ti, (f) V. Thick solid curve, present MRBEB cross section Eq. (3.13); dash-dash curve, MBEB cross section Eq. (3.11) dot-dot curve, DWBA by Bote *et al*[36]; dot-dash curve, relativistic empirical formula by Hombourger [75]; short dot-dash curve, XCVTS semi-empirical formula by Haque *et al*[37]; Experimental data by Egerton *et al*[76], Tawara *et al*[77], Hink *et al*[78], Isaacson *et al*[79], Glupe *et al*[80], Platten *et al*[81], Ishii *et al*[82], Kamiya *et al*[83], Hoffman *et al*[84], Shchagin *et al*[85], He *et al*[86], Jessenberger *et al*[87], and An *et al*[88].
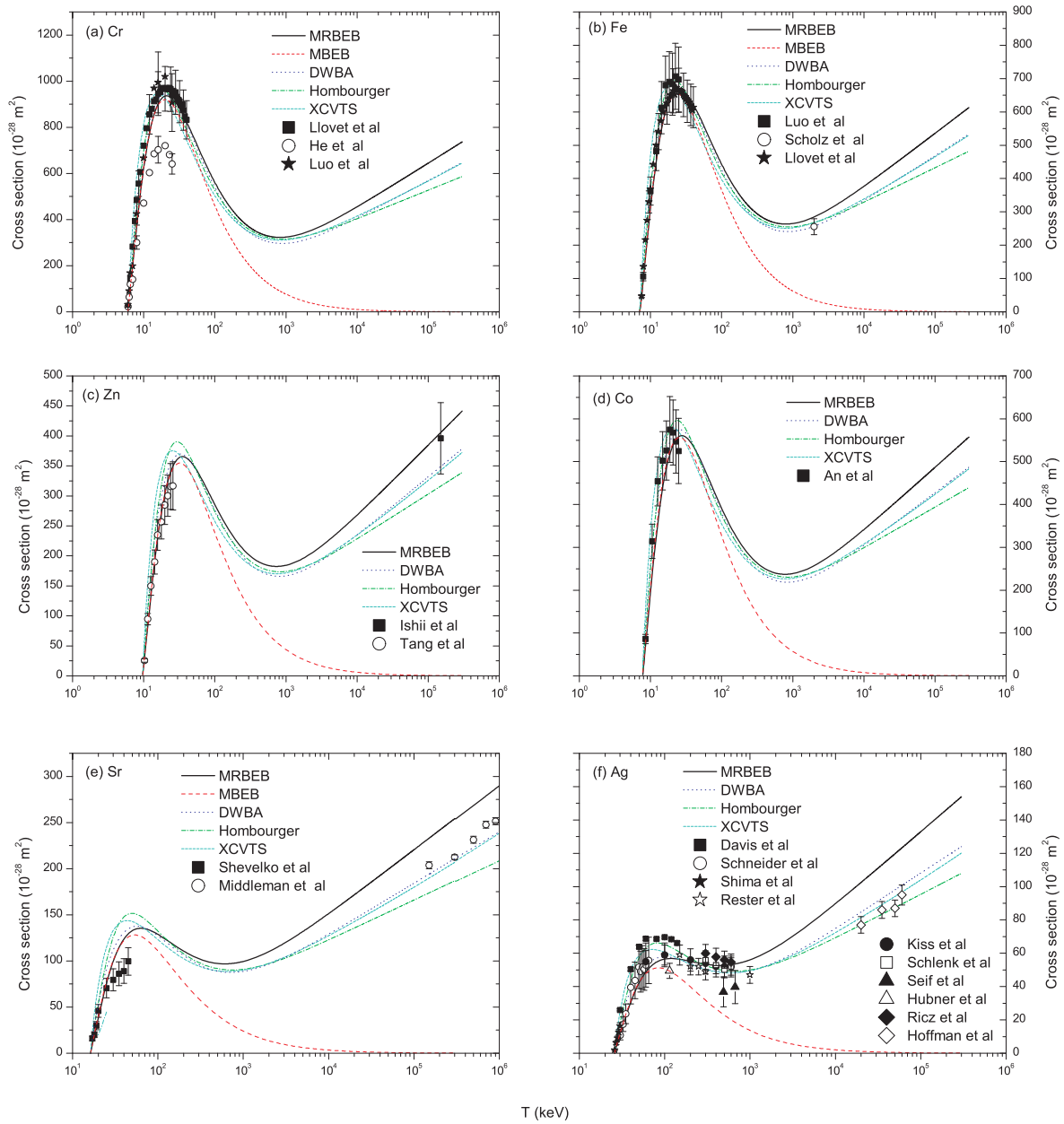
Figure 4.2: Electron impact K-shell ionization cross sections for (a) Cr, (b) Fe, (c) Zn, (d) Co, (e) Sr and (f) Ag. Thick solid curve, present MRBEB cross section Eq. (3.13); dash-dash curve, MBEB cross section Eq. (3.11) dot-dot curve, DWBA by Bote *et al.* [36]; dot-dash curve, relativistic empirical formula by Hombourger [75]; short dot-dash curve, XCVTS semi-empirical formula by Haque *et al.* [37]; Experimental data by Llovet *et al.* [89], He *et al.* [86], Luo *et al.* [90] (Cr), Luo *et al.* [91] (Fe), Scholz *et al.* [92], Ishii *et al.* [82], Tang *et al.* [93], An *et al.* [94], Shevelko *et al.* [95], Middleman *et al.* [96], Davis *et al.* [97] Schneider *et al.* [98], Shima *et al.* [99], Rester *et al.* [100], Kiss *et al.* [101], Schlenk *et al.* [102], El Nasr *et al.* [103], Hubner *et al.* [104], Ricz *et al.* [105], and Hoffman *et al.* [84].
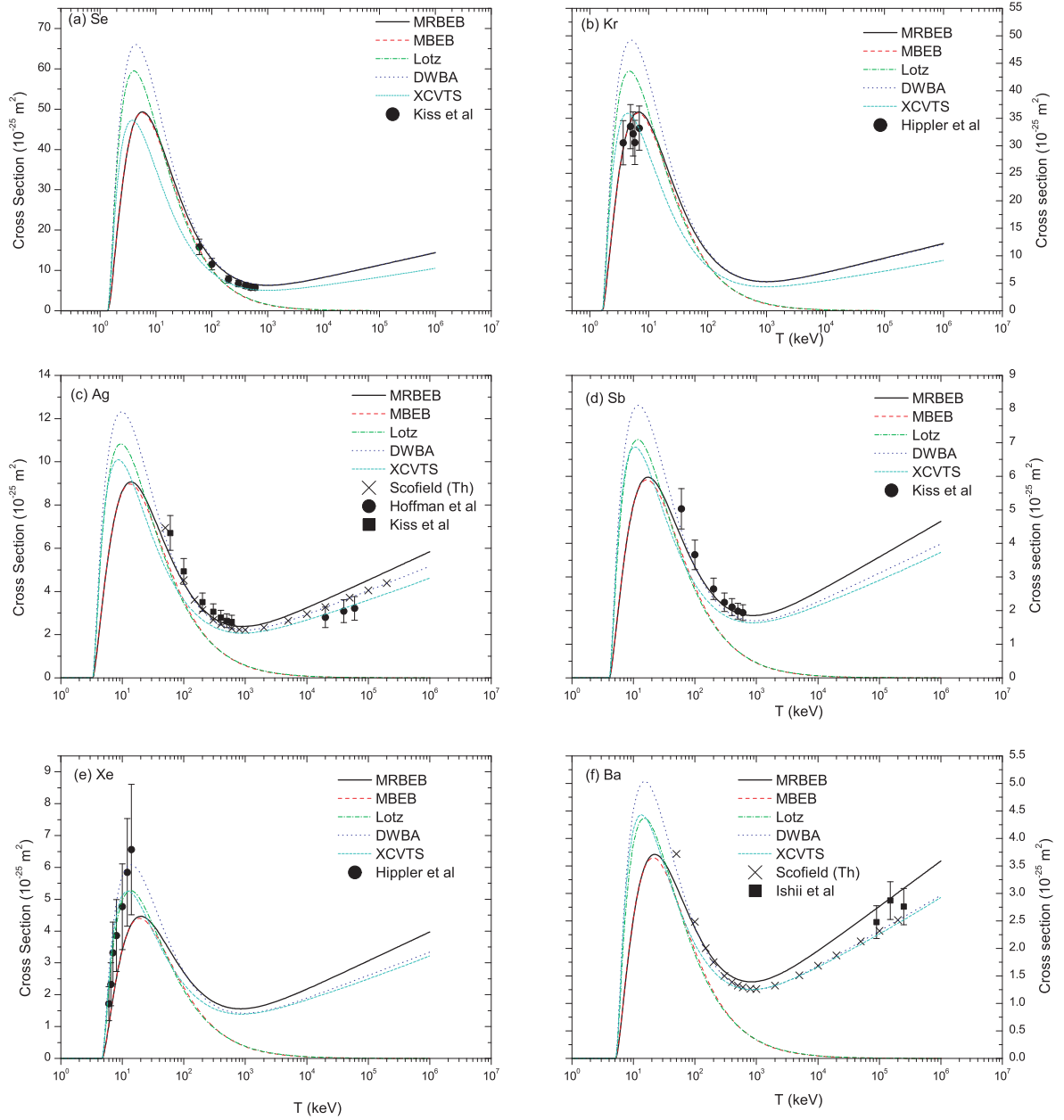
Figure 4.3: Electron impact L-shell ionization cross sections for (a) Se, (b) Kr, (c) Ag, (d) Sb, (e) Xe and (f) Ba. Thick solid curve, present MRBEB cross section Eq. (3.13); dash-dash curve, MBEB cross section Eq. (3.11) dot-dash curve, relativistic empirical formula by Lotz [26, 106]; dot-dot curve, DWBA by Bote *et al.* [36]; short dot-dash curve, XCVTS semi-empirical formula by Haque *et al.* [37]; ×, DWBA values by Scofield [60]; Experimental data by Ishii *et al.* [82], Kiss *et al.* [101], Hippler *et al.* [107], and Hoffman *et al.* [108].
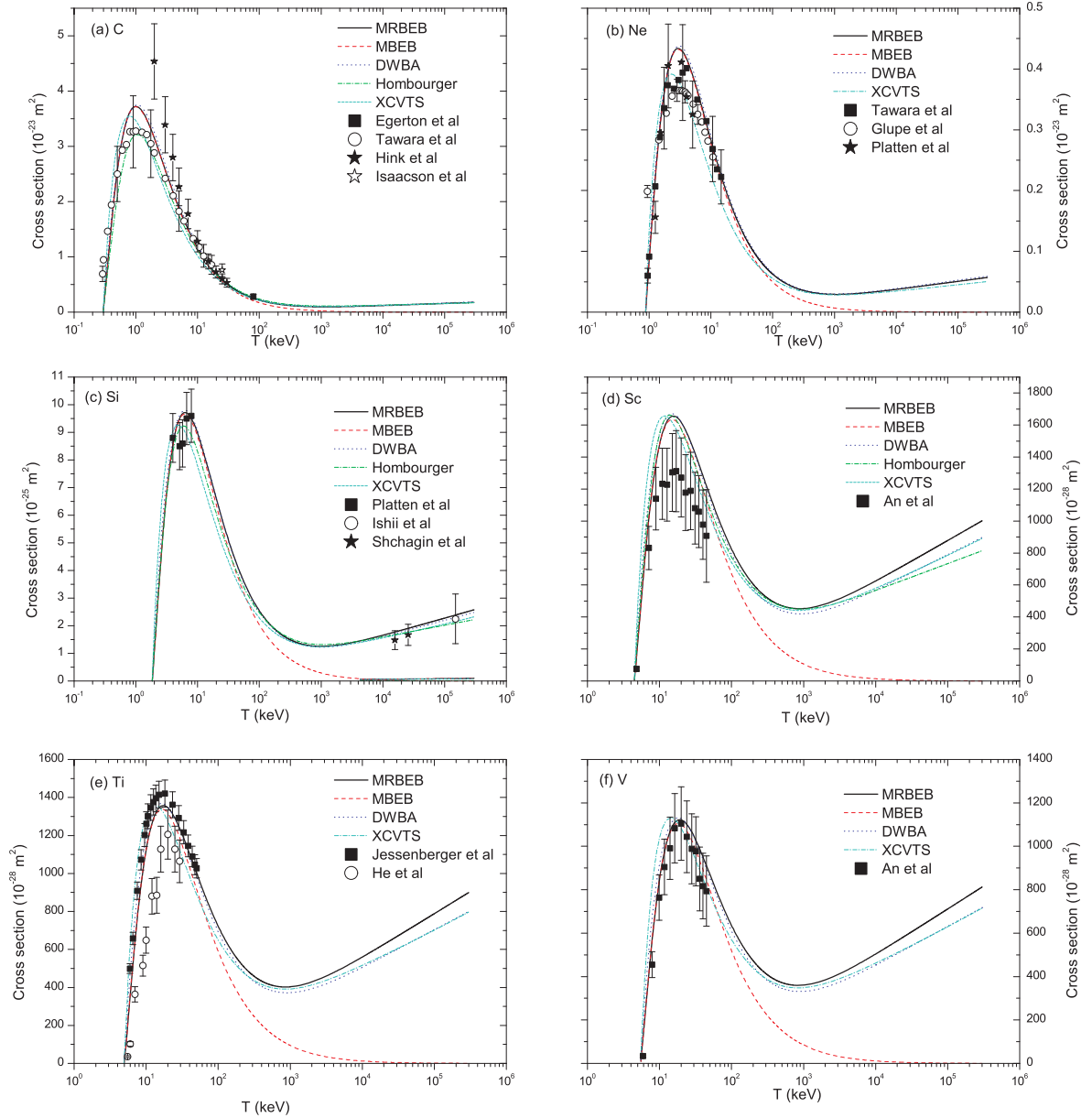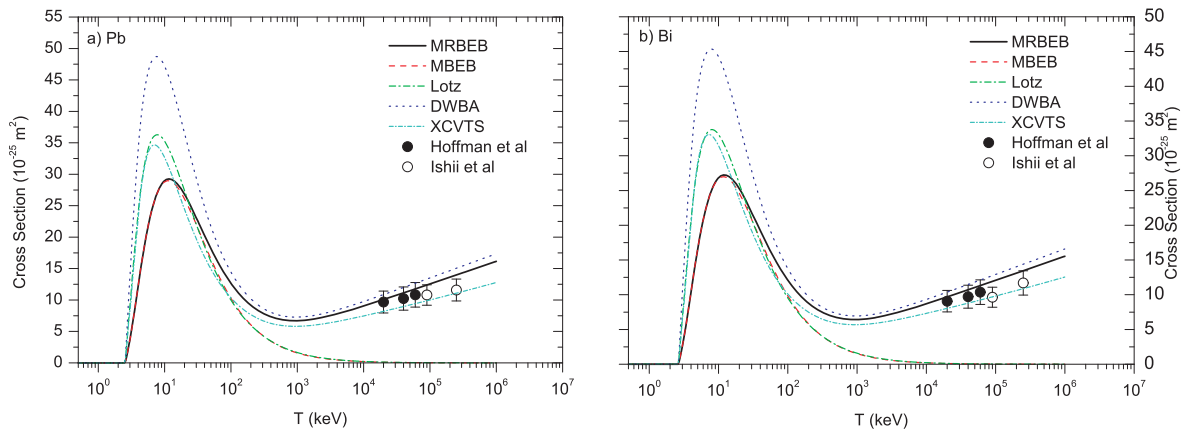
Figure 4.4: Electron impact M-shell ionization cross sections for (a) Pb and (f) Bi. Thick solid curve, present MRBEB cross section Eq. (3.13); dash-dash curve, MBEB cross section Eq. (3.11) dot-dash curve, relativistic empirical formula by Lotz [26, 106]; dot-dot curve, DWBA by Bote *et al.* [36]; short dot-dash curve, XCVTS semi-empirical formula by Haque *et al.* [37]; Experimental data by Ishii *et al.* [82], and Hoffman *et al.* [108] .
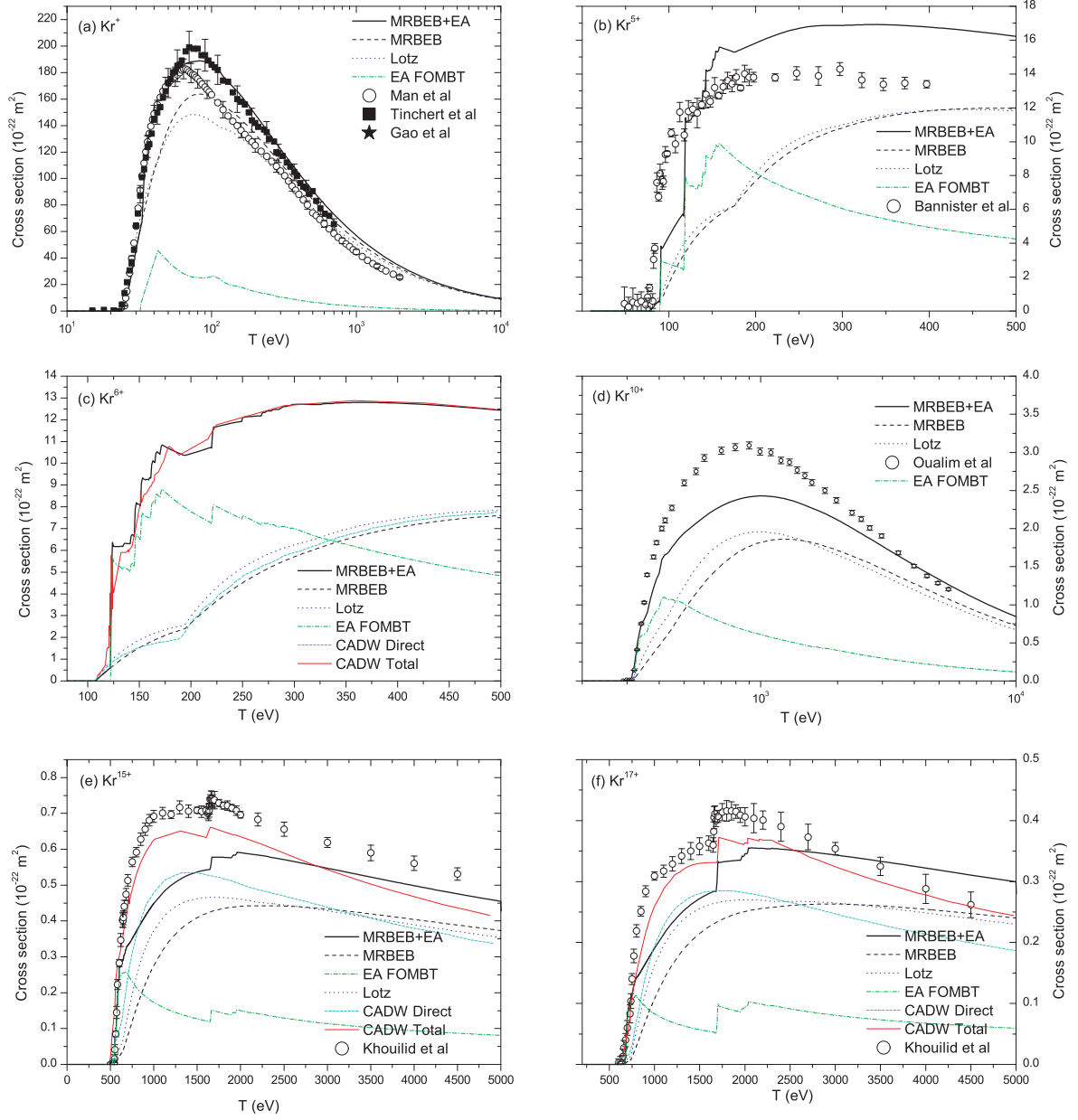
Figure 4.5: Total electron impact ionization cross sections for (a) Kr$^+$, (b) Kr^{5+}, (c) Kr^{6+}, (d) Kr^{10+}, (e) Kr^{15+}, (f) Kr^{17+}. Thick solid curve, presents the MRBEB cross section Eq. (3.13) with the contribution of excitation-autoionization calculated with the code of Cowan; dash-dash curve, MRBEB direct cross section Eq. (3.11); dot-dot curve, Lotz expression *et al*[26]; the remaining curves are explained in the figure; Experimental data by Man *et al*[130], Tinchert *et al*[112], Bannister *et al*[113], Oualim *et al*[115] and Khouilid *et al*[116]
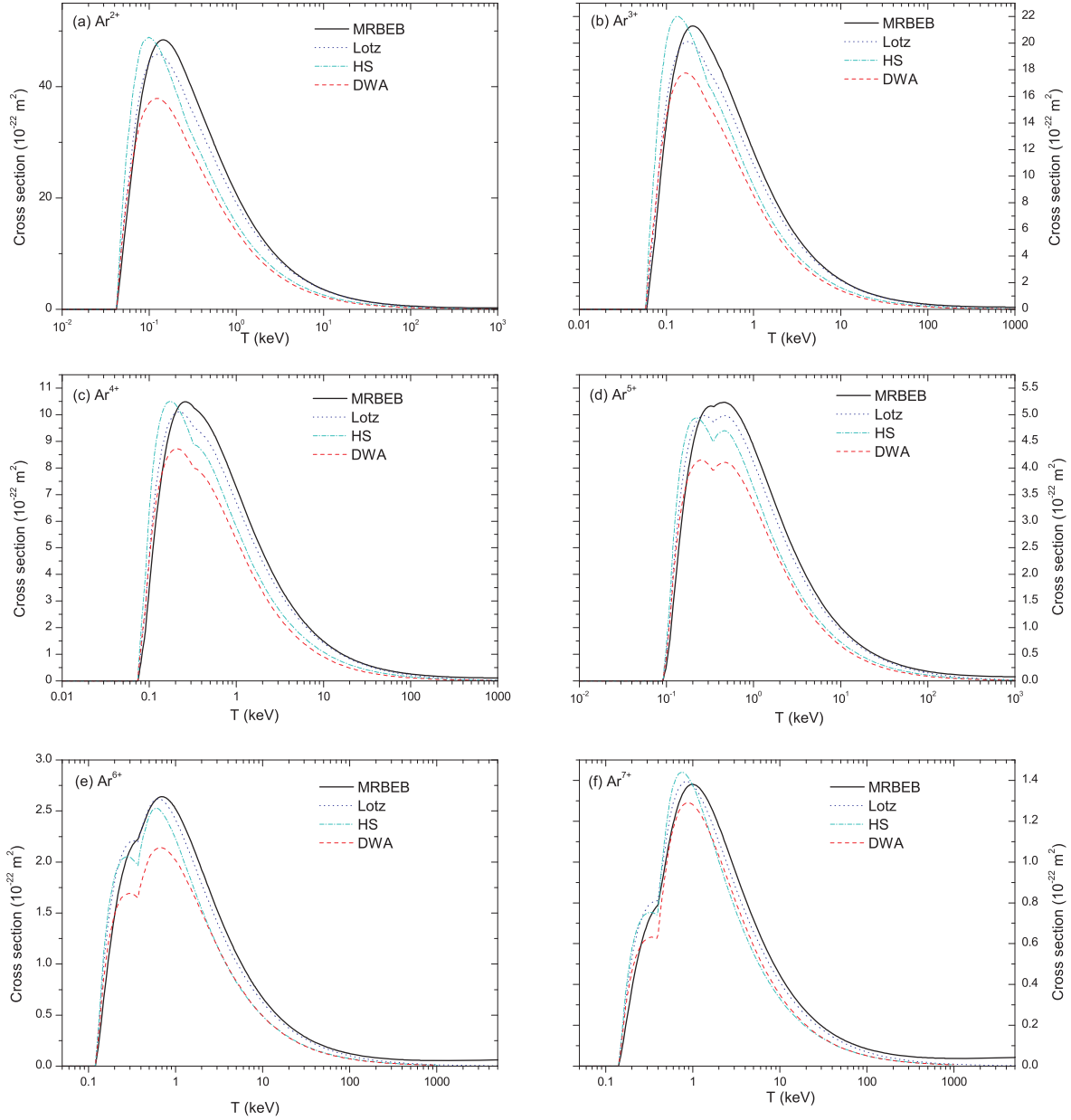
Figure 4.6: Total direct electron impact ionization cross sections for (a) Ar^{2+}, (b) Ar^{3+}, (c) Ar^{4+}, (d) Ar^{5+}, (e) Ar^{6+} and (f) Ar^{7+}. Thick solid curve, presents the MRBEB cross section Eq. (3.13); dash-dash curve, Hydrogenic Scaling (HS) direct cross section (Ref. [126]); dot-dot curve, Lotz expression (Ref. [26]); dash-dot curve, Distorted Wave Approximation (Ref. [127]).
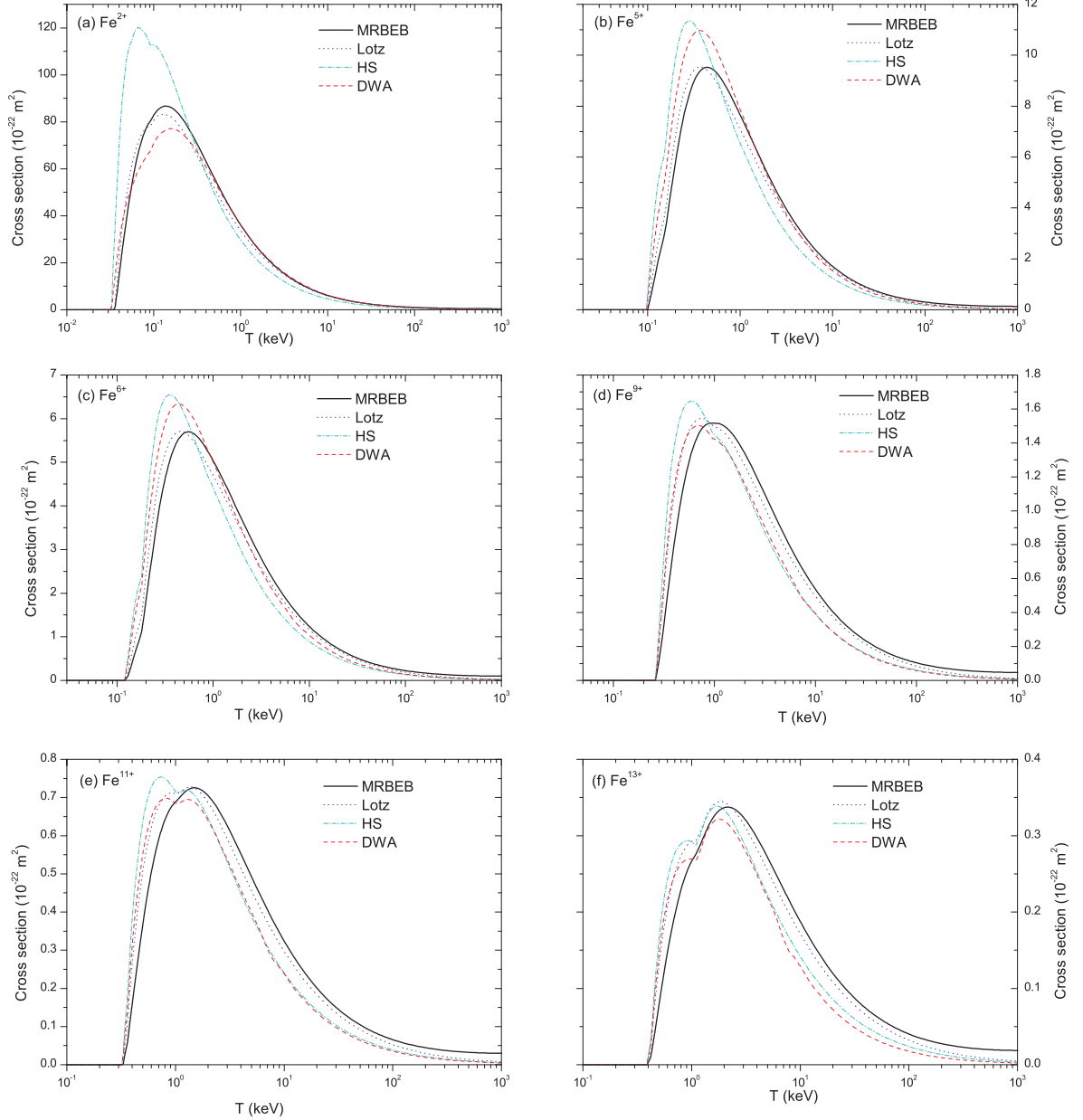
Figure 4.7: Total direct electron impact ionization cross sections for (a) Fe^{2+}, (b) Fe^{5+}, (c) Fe^{6+}, (d) Fe^{9+}, (e) Fe^{11+} and (f) Fe^{13+}. Thick solid curve, presents the MRBEB cross section Eq. (3.13); dash-dash curve, Hydrogenic Scaling (HS) direct cross section (Ref. [126]); dot-dot curve, Lotz expression (Ref. [26]); dash-dot curve, Distorted Wave Approximation (Ref. [127]).

Results

Chapter 5

Conclusions

5.1 Conclusions

The new MBEB and MRBEB models presented in this work require only one atomic parameter, namely the binding energy of the electrons to be ionized, and, contrary to the BEB/RBEB models, use only one scaling term $[1/(T+X)]$ for the ionization of all sub-shells. The role of the Burgess-Vriens denominator was investigated, and some light was shed on the early success of binary encounter-type models that relied on this scaling factor.

The MBEB and MRBEB expressions were used to obtain the K-, L-, and M shell ionization cross sections by electron impact for several atoms with Z from 6 to 83. The scarcity of data for near threshold energies of L- and M-shell cross sections does not allow us to assess the competing models in the ionization peak. On the other hand, in K-shell ionization our model excels and is very accurate in a wide range of elements.

We pointed out that the comparison of the MRBEB cross sections to experimental values contains inherent ambiguities because, like most of the analytical models, whether derived from first principles or empirical, the MRBEB model predicts cross sections for the direct ionization of electrons of a definite sub-shell. However, most experimental data are based on all sub-shell vacancies created by direct ionization as well as excitations to bound levels, so unless this processes are effectively excluded there will be some indirect processes in the experimental data.

As show on Figs. 4.1 to 4.7, relativistic effects become increasingly important as the binding energies of the elements increase. Hence, relativistic theory must be used for treating both atomic structure and collision dynamics for medium to heavy atoms or ions.

The method shows that for inner-shell of neutral atoms and total ionization of lowly charged as well as for moderately charged ions, the cross section shape and intensity is within resonable limits ($\pm$ 20%) for use in X-ray spectroscopy analysis of plasmas of any kind, which was our main goal.

The calculation of excitation cross sections for the Kr ions were also performed in this work as they are one of the dominant processes in X-ray analysis from plasmas.

Comparison to crossed-beams experimental measurements, as well as configuration averaged distorted wave and distorted wave approximation theories, shows that the slope of the MRBEB cross section at energies below the first ionization peak is lower than expected. Nevertheless, in electron-cyclotron-resonance ion-source (ECRIS) plasma processes, the near threshold effects for the valence electron are not as important as the processes which occur at higher energies. The electron temperatures considered in the analysis of ECRIS plasma spectra are normally higher than 1 keV and lower than 20 keV [9, 122] as will be shown in Chapter 8. These values were taken from a survey of temperature measurements from the electrons in the plasma of a variety of ECRIS [131–137], with microwave frequencies ranging

from 2.45 GHz to 28 GHz and with conventional, permanent or superconducting magnets.

The simple relativistic MRBEB expression presented in this work provides a continuous coverage of inner and outer-shell ionization cross sections by electron impact of neutral atoms and ions from the threshold to relativistic incident energies, making this expression ideally suited for modelling systems where ionization cross sections for a wide range of incident energies are required, such as fusion plasmas.

A web database was built during the course of this work for the purpose of allowing electron impact ionization cross sections calculations with the MRBEB model in a very easy way. This ionization cross section database was named ELIIXS. In ELIIXS, elements ranging from hydrogen to uranium can be picked and the ionization cross sections can be calculated for every sub-shell of the chosen element. The database is being constantly updated in order to present, along with the MRBEB results, experimental results for each atom and/or subshell. Every result will be exportable as an Excel file for practical usage. The ELIIXS web database is located at http://sites.fct.unl.pt/eliixs/.

Part II
X-ray spectroscopy of an electron-cyclotron-resonance ion-source Ar plasma

Chapter 6

Experimental Aparattus

6.1 Goals and Motivation

In the experimental part of this work, we have used a double crystal spectrometer (DCS) and an electron cyclotron resonance ion source (ECRIS) to perform a 2.5 ppm measurement on the $1s2s\ ^3S_1 \to 1s^2\ ^1S_0$ "relativistic" $M1$ transition in He-like argon. This measurement was made without reference to any theoretical or experimental energy, using the known lattice spacing of a Si crystal, tied to the definition of the meter, as a transfer standard. The experimental apparatus has been built during the last ten years at an ECRIS source located at Source d'Ions Multichargés de Paris (SIMPA). The experiment is located at the Laboratoire Kastler Brossel in the Ecole Normale Supérieure, CNRS, Université Pierre et Marie Curie-Paris 6.

Detailed tests of bound-state QED have been provided by measuring transitions in simple systems like hydrogen. Decays to the $1s$ level have been measured [138] with an accuracy of a few parts in 10^{14} while the $n = 2$ Lamb shift is known to a few ppm accuracy [139]. Helium has also been thoroughly studied [140], and agreement between experiment [141, 142] and theory [143] in the fine structure is now very good. However, a recent measurement of the Lamb shift in muonic hydrogen (μP) [144] provides a proton charge radius 6.9 standard deviations away from the latest 2010 CODATA value obtained by combining results from hydrogen spectroscopy and electron-proton scattering [145].

The cause of this discrepancy can be investigated with measures in atomic ions with different scale compared to the electron Compton wavelenght λ_C, the fundamental scale of QED, different field strengths as measured by $(Z\alpha)$ and different nuclear size corrections. Compared to simple neutral systems like hydrogen or helium, one- and two-electron ions are more sensitive to QED corrections, which vary as $(Z\alpha)^4$, while the dominant non-relativistic contribution to the transition energy varies like $(Z\alpha)^2$, thus making these systems highly adequate to explore the said corrections.

In the last years, a number of accurate experiments have been performed on the $1s^2 2p \to 1s^2 2s$ transition in Li-like ions with Z = 1 to 92 at storage ring [146] or EBIT facilities [147]. These measurements have accuracies of the order of the size of two-loop QED corrections to the lower level energy (see for example Ref. [148] for a recent review). Such $\Delta n = 0$ transitions have also been measured in two-electron Si^{12+} with laser spectroscopy to 0.8 ppm [149] and in U^{90+} [150]. Measurements of $n = 2 \to n = 1$ transitions, even at high-Z, are not yet sufficiently accurate to test two-loop QED corrections [151]. Very high-Z systems are also very sensitive to nuclear size corrections (see, e. g., [152]) and nuclear polarization [153], which ultimately limits the accuracy of the comparison. Recently, the allowed $1s2p$ $^1P_1 \to 1s^2\ ^1S_0$ transition in He-like Ar has been measured to 1.9 ppm accuracy, relative to the theoretical value of the Lyman α transition in H-like Ar [154]. In the same work, the

Lyman α transition in H-like chlorine was measured to 10 ppm accuracy, without external reference. Earlier absolute measurements on both the $1s2s\ ^3S_1 \rightarrow 1s^2\ ^1S_0$ "relativistic" $M1$ and $1s2p \rightarrow 1s^2$ transitions of He-like V [155], were calibrated against a series of X-ray standards [73, 156], reaching an accuracy of ≈ 30 ppm. Half of this uncertainty is related to the difficulties associated with broad, asymmetric X-ray standards from core-excited neutral elements, sensitive to excitation conditions and chemical effects [73, 156].

The method used in this work, which successfully combines for the first time a DCS and an ECRIS, prevents the difficulty associated with existing X-ray standards since it provides absolute measurements tied to the definition of the meter. Contrary to the case of x rays emitted by neutral elements with a K-hole, which were, up to now, the only transitions measured with a DCS, the $M1$ line is much narrower than the instrument response function. It can thus be directly used to probe for the first time the shape of this response function. To deconvolute the experimental spectra from all the known physical features arising from the use of a DCS in reflectivity mode, Amaro [157] developed a simulation code, that exactly contains the geometry of the instrument and of the X-ray source, the X-ray beam vertical divergence and the shape of the crystal reflectivity profile, as well as the line width and Gaussian Doppler broadening. This simulation was also a key ingredient in the fine tuning of the experimental apparatus by targeting and correcting systematic errors as can be seen in Ref. [157].

The experimental part of this work is organized as follows: On the remainder of this chapter we will make a brief overview of the technical aspects of the ECRIS (Sec. 6.2). In Sec. 6.3 we will explain the operating mechanics of the DCS and describe roughly the Monte-Carlo simulation used to both improve and interpret experimental results obtained from this particular DCS. In Sec. 6.4 we will make a description of the temperature control for both crystals of the DCS and discuss the role of the temperature control on the overall error budget.

On Chapter 7 we will present a measurement of the "relativistic $M1$" transition energy in heliumlike argon and compare them with other experimental and theoretical results. From the $M1$ line we will probe the response function of the experimental apparatus (Sec. 7.2). This will set the basis on which the natural lines of any given transition can be thoroughly investigated.

On Chapter 8 the first survey spectrum of an argon plasma obtained with a DCS is analysed in order to obtain an external reference for the charge state distribution inside the ECRIS.

The final conclusions will be given in Chapter 9.

6.2 Electron-Cyclotron-Resonance Ion-Source (ECRIS)

Electron-cyclotron-resonance ion-source devices are in wide use, providing medium to highly charged ion (HCI) beams for injecting in accelerators, ion traps or to study the interaction dynamics of ions with matter at low energies. The ECRIS was first proposed by Geller *et al*[158] in 1969 and by Potsma *et al.* [159] in 1970, and the first operational ECRIS was presented by Geller and his co-workers in 1971 [160]. From that time on, the technology has rapidly advanced and several splendid reviews on the technique can be found in the literature [161–164].

In an ECRIS, the energy source for plasma generation and maintenance is resonant electron heating by microwave radiation. The basic principles upon which the ECRIS is predicated are demonstrated in Fig. 6.1. A metallic vessel serves both as a multi-mode cavity and as a plasma chamber. The dimensions of the chambers must be larger than the microwave wavelength being used, generally with frequencies ranging from 2.2 to 28 GHz. For a frequency of 14.5 GHz like the all permanent-magnets, SUPERNANOGAN [165] ECR ion

source, named SIMPA (Source d' Ions Multichargés de Paris), the wavelength is $\lambda = 2$ cm. The SIMPA, on which this work has been performed, has been jointly operated by Laboratoire Kastler Brossel (LKB) and the Institut des NanoSciences de Paris (INSP) since 2004. The microwave field, in this particular machine is created by a 2KW klystron and inserted through a single ridge wave guide on the plasma chamber. From the first stage or injector stage, a reservoir of electrons, provided by a polarization electrode, a stream of electrons diffuses into the main second stage where the cold plasma is ignited. In order to produce
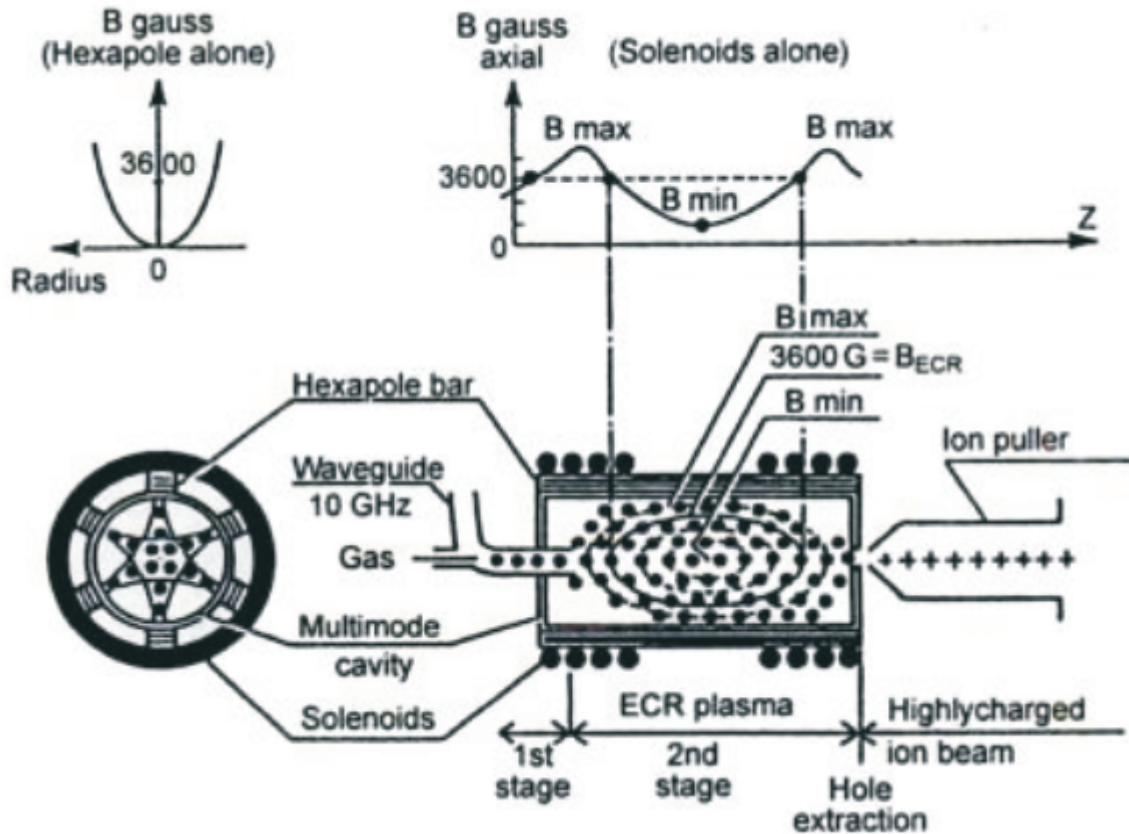
Figure 6.1: Principle of operation of a 10 GHz ECRIS. The plasma electrons are trapped in a B_{min} structure and are energized at the magnetic surface where the magnetic field is B_{ECR}. Picture taken from Ref. [166] ©1991 Springer

multiply charged ions through step-by-step ionization it is essential to maximize the product of electron density, electron velocity and ion confinement time, $N_e v_e \tau_c$. At the same time the neutral density has to stay low in order to avoid charge exchange between neutral atoms and highly charge ions, which results in ion-charge reduction. Theoretical estimates [167] show that ion confinement times of 10 ms or more are required to effectively produce highly charged ions like Ar^{16+}. Such high confinement times are achieved through the use of magnetic traps or bottles in a so-called minimum-B structure. This is illustrated in Fig. 6.1 where the magnetic configuration is a superposition of an axial mirror and an hexapole field used, respectively, for the axial and radial confinement of electrons. This magnetic bottle is usually created using either permanent magnets, or normal coils, although several devices such as the VENUS in Berkeley [168] and SERSE in Catania [169, 170] use superconducting coils. Other devices, such as the ECR ion trap (ECRIT) at the Paul Scherrer Institute (PSI), use a combined superconducting coils magnetic bottle and a permanent magnet hexapole [171]. In Fig. 6.1 the B_{min} and B_{max} values of the axial field and the ellipsoidal electron-cyclotron-resonance surface fulfilling the resonance condition for a 10 GHz microwave field

are illustrated.

The absorption of the microwave energy occurs on a constant $|B|$ surface in the source such that $2\pi f = e|B|/m_e$ where f is the electromagnetic wave frequency and e and m_e are the electron charge and mass, respectively. For a 14 GHz frequency, the magnetic field corresponding to the ECR surface is $B_{ECR} = 0.51$ T. Upon passing the resonant surface, the electrons may be stochastically heated if a component of the electric field vector of the microwave is perpendicular to the direction of the magnetic field. The energetic electrons, ionize by inelastic collisions the gas in the magnetic structure, and the resulting ions are trapped in the space charge of the electron gas. The resulting plasma is non-thermal, where the ions have temperatures in the range of a few eV while the electrons can reach several tens of keV. Due to the high electron temperature, electron-impact ionization can create holes in the inner-shells of any element present in the plasma, and the radiation coming from the transitions to the created inner-shell holes in the ECRIS plasma can thus be used for plasma diagnostics [172].

In the commercial 14.5 GHz, all permanent-magnets, SUPERNANOGAN [165] ECR ion source, the electronic temperature has been measured through the use of electron Bremsstrahlung spectra [131]. Also, high-resolution X-ray spectroscopy has been applied to characterize charge state distribution and electronic density [8].

In Fig. 6.2, the SIMPA ECRIS is illustrated. On the right side of the ECRIS, a portion of plasma can be extracted with the use of electrostatic lenses and focused with a solenoid. Then, a single charge state from the extracted plasma can be selected with a dipole magnet for experiments, such as spectroscopy inside an electrostatic trap and surface interaction with HCI. On the left side of the ECRIS, there is a beryllium window that is resistant to the vacuum pressure (≈ 100 N/m^2) and semi-transparent to low energy x rays (reduction of a factor of two at 3 keV). This enables the observation of x rays from the plasma center with X-ray spectrometers such as the mosaic-crystal spectrometer or a double crystal spectrometer (DCS).
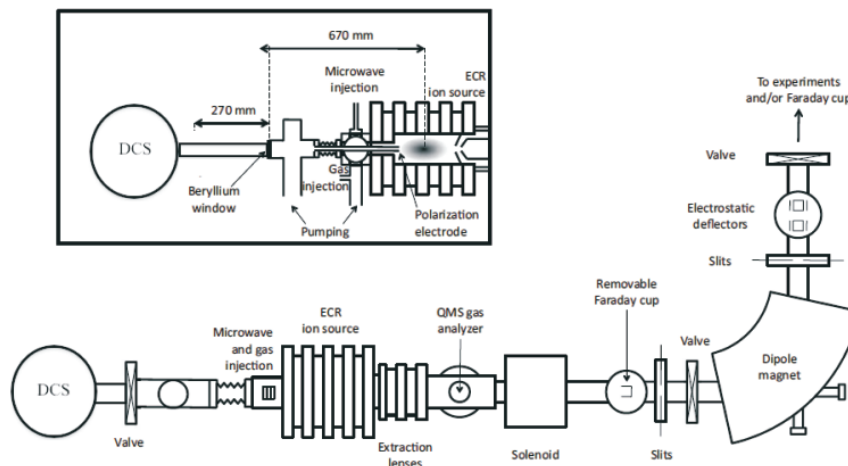
Figure 6.2: On the right side of the apparatus, the HCI are extracted for experiments on electrostatic traps and surfaces experiments, and on the left side, a double crystal spectrometer measures the outcoming x rays from the plasma center. Picture taken from Ref. [131] with a different X-ray detector (DCS)

6.3 Double Crystal Spectrometer (DCS)

Double crystal spectrometers are Bragg-type spectrometers in which two flat crystals are arranged in such a way that the incoming x rays are deflected consecutively by each crystal. An illustration of the operating scheme of a DCS is presented on Fig. 6.3. From the Bragg law,
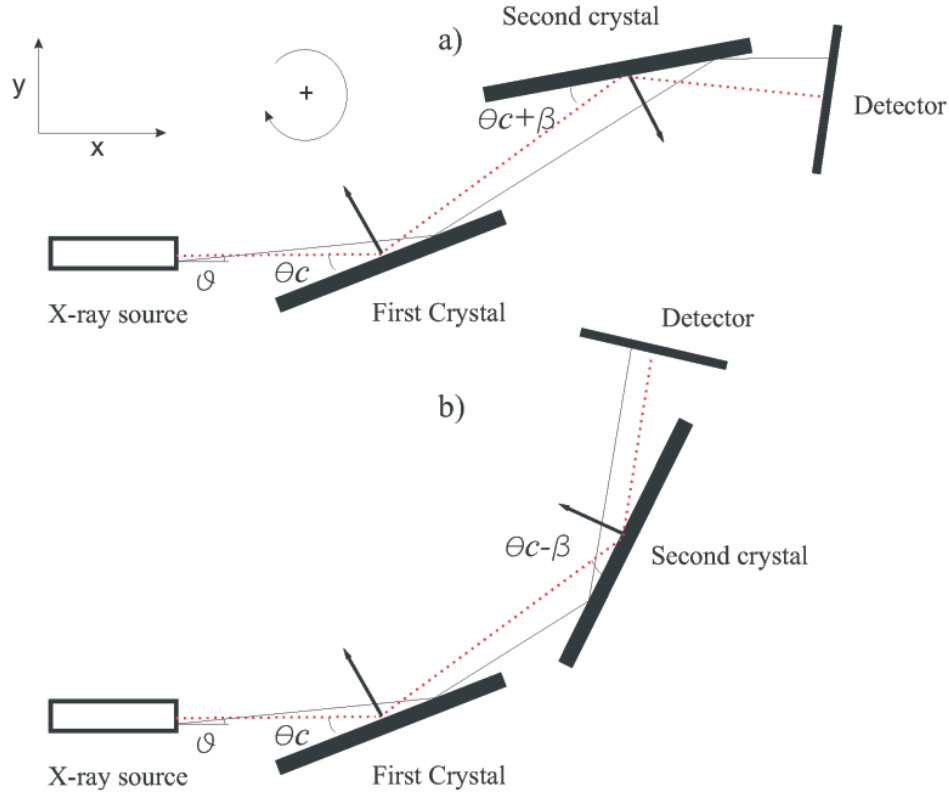
Figure 6.3: Representation of the two operating modes of a DCS. The spectrometer can be set in a way in which the x rays undergo reflections from the two crystals in parallel,a), and antiparallel, b), geometries.

which states that an monochromatic X-ray electromagnetic wave on a crystal will be reflected only at a certain specific angle, θ_B depending on its wavelenght, λ, we get a dependence of the wavelenght reflected from a crystal with the angle between the incident radiation and vector normal to the crystal planes

$$n\lambda = 2d \sin \theta_B, \tag{6.1}$$

where d is the interplanar distance of the crystal and n is the order of the diffraction. Taking into account Bragg's law and the geometrical settings illustrated in Fig. 6.3, we see that in this device, the first crystal, which is kept at a fixed angle, acts as a collimator, defining the direction of the incoming X-ray beam, which is analysed by the second crystal. It is also shown in the figure that two different settings are possible for this spectrometer, one where the two crystals are parallel (non-dispersive mode), and another where both crystals deflect the beam in the same direction (dispersive mode), which will be labelled as anti-parallel from now on. The operating system of a DCS is the following: a first peak is obtained by scanning the second crystal angle in the parallel mode, the shape of which depends only on the crystal reflection profile and provides the instrument response function, whose full width at half maximum (FWHM), in this case, was calculated by Amaro to be $(9.6\pm0.4)\times10^{-4}$ ° or 0.6 ± 0.2 eV [157]. A second peak is obtained in the anti-parallel mode, which is a convolution of the line shape and instrument response function. The position of the first crystal is the

same in both modes. The difference in angle settings of the second crystal between the non-dispersive and the dispersive modes is directly connected to the Bragg angle by the relation $\theta_B = [180 - (\theta_{disp} - \theta_{nondisp})]/2$. Small corrections due to the Si index of refraction and to the vertical divergence of the beam must be performed (see, e.g., [73]).

The spectrometer used in this work, which is presented in Figs. 6.4 and 6.5 was built for mechanical and thermal stability and precision positioning of the crystals. The table and the axis of the table are made of a special steel (nitrated stainless steel LK3) that was thermally treated at 900 °C after machining to avoid residual constraints in the material. An Huber goniometer 410/410A motor is used for the first crystal, a Newport RV80 for the second crystal and a RV240 for the rotation of the detector which sits on a third rotation table, concentric to the second crystal axis. The angle of the first crystal is measured with an Heidenhain ROD800 encoder installed in the vertical axis to a precision of 0.07", while the second crystal angle is measured up to a precision of 0.2" (1.2 ppm at 3.1 keV) with an Heindenhain RON905 encoder, controlled by an Heidenhain AWE1024 box. The encoders have built-in transparent glasses with high quality graduated scales concentric to the axis rotation. A LED and photocell system are mounted on opposing sides of the graduated scale, resulting in a detected light signal which depends on the position of the LED/photocell system in relation to the glass grating. As the encoder is turned on its axis the optical signal is almost perfectly sinusoidal allowing for a very precise angle reading. Measurement of absolute angles are possible trough a second glass scale which has only a single reference mark, therefore after every reboot, a full turn of the encoders is needed in order to find the reference. The table rotates inside a metallic chamber around the same vertical axis as the first crystal. The metallic surface, where the table rotates on cone shaped wheels inside the chamber, was prepared to be horizontally flat to a 2 μm accuracy. The chamber can be pumped down with a rotary pump to primary vacuum of 10^2 mbar that reduces the absorption of the low energy x rays. Other technical aspects about the DCS not mentioned here can be found in Schlesser's Thesis [173].
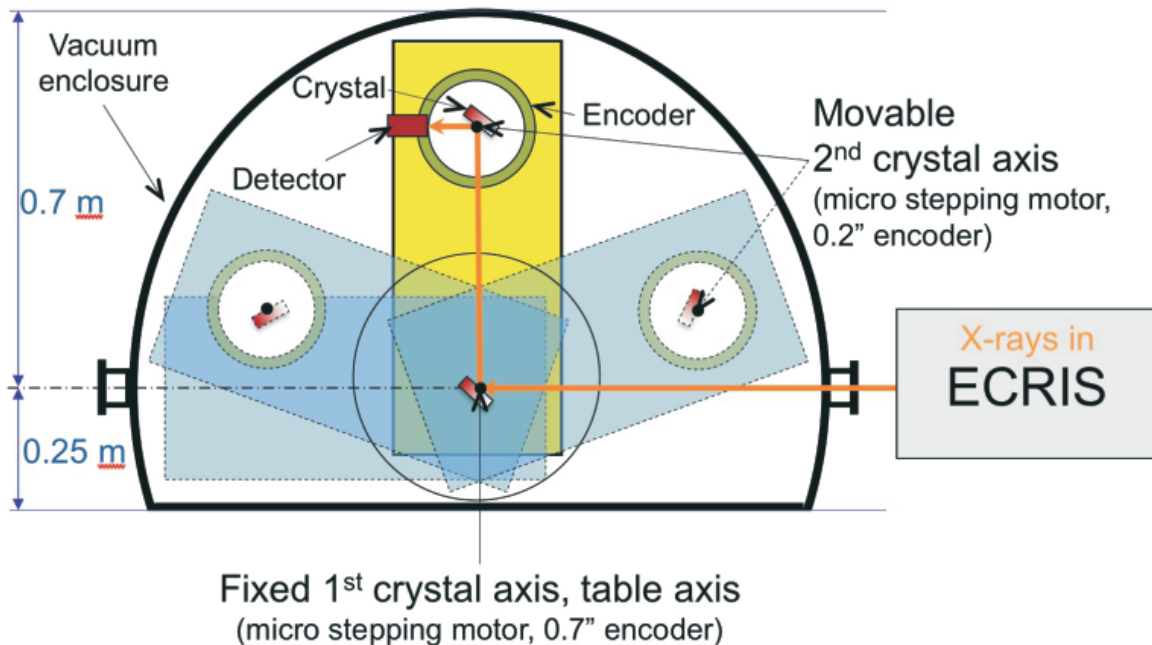

Figure 6.4: Top view illustration of a DCS. The rotating axes of both crystals are mounted in a single table with a rotating axis concentric with first crystal axis. The detector is also mounted in the table with a rotating path concentric with the second crystal axis..
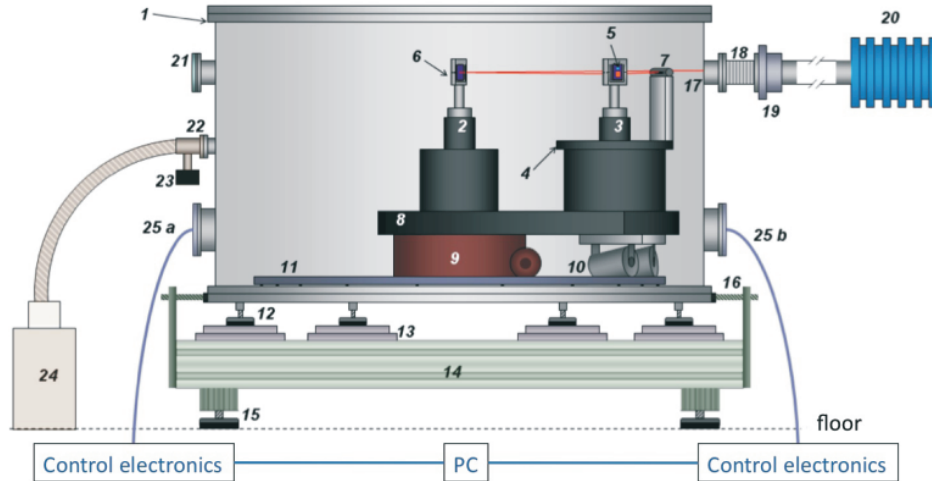
Figure 6.5: 1) vacuum enclosure; 2) axis ♯1 (crystal 1 and table); 3) axis ♯2 (crystal 2 and detector); 4) detector rotation support; 5) crystal; 6) crystal holder; 7) detector; 8) table; 9) table rotation support; 10) rotating cones; 11) tracks for cones; 12) enclosure support; 13) translation stages; 14) support; 15) legs; 16) translating screws; 17) X-ray entrance; 18) bellows; 19) Be window; 20) ECRIS SIMPA; 21) window; 22) connection to pumping; 23) pressure gauge; 24) rotary vacuum pump; 25) a and b feed-through for cables. Figure obtained from Ref. [157]

6.3.1   X-ray input

As said before, the incoming x rays emitted from the ECRIS pass through a beryllium window which is semi-transparent to low energy x rays (attenuation of 50% at an energy of 3 keV). The polarization electrode inside the plasma chamber, together with the first crystal, acts as a collimator for the radiation reaching the second crystal. As described on Amaro's PhD thesis [157], the ray distribution reaching the first crystal with a given angle depend on the shape of the geometrical slits and the distribution of the intensity of the focal spot. For an uniform source and the combination of the collimators present on the experiment, the number of rays reaching the first crystal with a given wavelength as a function of the horizontal and vertical angles, is a conical distribution (Fig. 6.6). Because, varying the energy is effectively the same as changing the first crystal angle, we conclude that, for a fixed first crystal angle, the number of rays (or the X-ray radiation intensity) decreases almost linearly with the change in energy from a central point in which the intensity is maximum. Simulations were performed with high statistics in which the first crystal angle, optimized for an energy of 3104 eV, was kept fixed and the energy of the monochromatic uniform-focal ray distribution was changed in 1 eV intervals. Voigt functions were fitted to every spectra and the maximum of the Voigt peak was recorded as a function of the energy. In Fig. 6.7 the simulated maximum number of rays, as a function of their energy, reaching the detector are presented. From Fig. 6.6 we expect that the distribution should be either triangular, if the vertical divergence is close to zero, or hyperbolic, if the vertical divergence is not null. If the vertical angle ϕ varies with the change in the horizontal angle ϑ the intensity distribution would not be hyperbolic nor triangular. In fact, if the dependence of ϕ with ϑ in the measured region is linear, we would observe a parabolic intensity distribution. Thus, measuring a given line with different first crystal angles with sufficient accuracy could provide a reasonable method for inferring the vertical alignment of the DCS, although for a correct distribution measurement the X-ray source would have to be very stable in the course of several hours or the measured line would have to be very intense. Fig. 6.7 shows that although the vertical divergence is not exactly
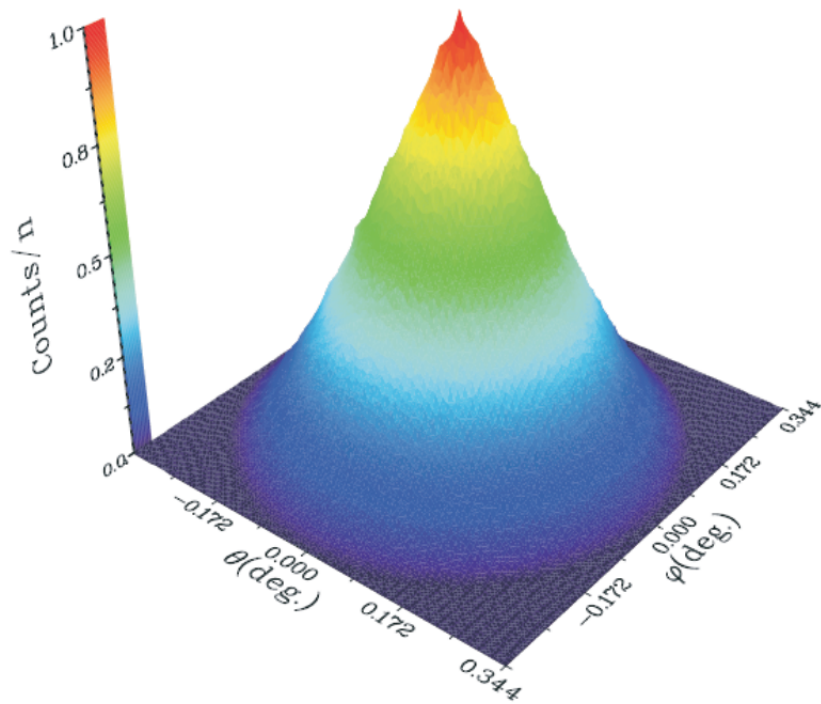
Figure 6.6: Histogram of the number of rays for horizontal and vertical angles, ϑ and ϕ respectively, for an uniform focal distribution and a cylindrical geometry as a collimator. Figure taken from Ref. [157].
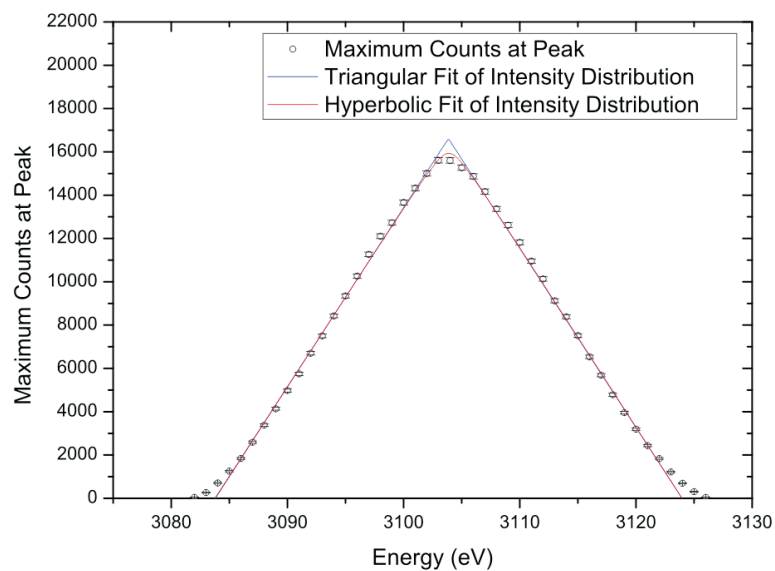

Figure 6.7: Intensity of the x rays reaching the detector for a given energy. A triangular fit to the data is shown in blue and an hyperbolic fit is shown in red.

zero, it is very close. The tails of the distribution do not follow the expected triangular or hyperbolic behaviour because in that region the X-rays are hitting the second crystal near the edge and other dynamical effects may play an important role. Nevertheless, measurements are always performed with the first crystal angle set in such a way that the measured line sits in the center of the distribution. The wide Ar spectrum presented in Sec. 8 sits on the 3087-3119 eV energy range presented on Fig. 6.7 which as can be seen is within the linear dependence. Depending on the energy of the peak, slight asymmetries of the line can occur. Such asymmetries are taken into account if a fit is performed with a simulated profile rather than a voigt profile. Such sensitivities to asymmetries arising from both the reflectivity profiles and the geometrical effects of the DCS apparatus are taken into account for the first time in X-ray standards measurements.

6.3.2 Crystal diffraction

The crystals used in this experiment were cut from a single bundle of silicon to ensure a perfect crystal without defects. Two different pairs of crystals were cut with Miller indices (111), which was used throughout this work, and (220). The crystals were polished and etched at NIST with a symmetry of the cut (angle between crystal planes and crystal surface) controlled to 11" at a temperature of 22.5 °C. The lattice spacing of the two orientations in the same Si bundle was also measured at NIST, using the crystal of the Avogadro Project [174] as the standard reference. The measured lattice spacing of the Si(220) crystal is $d(220) =$ 1.92015569(50) Å that corresponds to a lattice spacing of the Si(111) crystal equal to $d(111) =$ 3.13560111 Å. The uncertainty of these values varies according to the crystal and energy. For the Si(220) the uncertainty ranges from 0.45 to 3.6 ppm for the energy range from 3.6 to 12.0 KeV, while for the Si(111), the range is 0.45 to 3.6 ppm for the energy range 2.2 to 7.5 KeV. The linear thermal coefficient $\alpha(T)$ was also measured, and was found to be $\alpha(T) = 2.56 \times 10^{-6}$ °C^1. To remove the mechanical stresses and strains caused by the cutting procedures of the crystals and to avoid any mosaic effect, the crystals were etched in a bath of hydrofluoric acid, then polished and etched again.

The incoming x rays are reflected by the first crystal onto the second crystal and using dynamical theory of X-ray diffraction we can accurately calculate the reflectivity profiles of the crystals. For this purpose, the XCRYSTAL package, included in the X-ray oriented program 2.3 (XOP) [175] was used to obtain the reflectivity of both crystals. This package provides models of X-ray sources, like a synchrotron source, characteristics of X-ray optical devices, such as filters and crystals, data visualization and data analysis. In Fig. 6.8 a plot of the reflectivity of the Si(111) flat crystal is shown as a function of the angle centered on the Bragg angle $(\alpha - \theta_B)$ for the σ and π polarization of the incoming 3.104 keV photons as well as their sum, to account for the expected unpolarized radiation. Dynamical effects such as pendellosung and anomalous absorption are taken into account in the calculation of the reflectivity profiles and refraction indexes. Pendellosung occurs when a thin crystal is used with a thickness of the order of the extinction length. In our case, we used a crystal of thickness 0.6 cm, much higher than the extinction depth, which has values of 1.4 μm for s-polarization and 7 μm for p-polarization at 3.104 KeV for Si(111). We performed several simulations with XOP, proofing that pendellosung effects are washed out for crystal thicknesss above 20 μm. The σ and π refer to the polarization vector perpendicular and parallel to the surface, respectively. The inclusion of absorption on the generation of the reflectivity profile causes an asymmetric distortion of the σ component which results in an asymmetric unpolarized profile. The convolution of the reflection on both crystals results in a symmetric line in the non-dispersive mode and a slightly asymmetric line in the dispersive mode. We used the ray-tracing Monte-Carlo simulation code of Amaro [157] for the DCS, to evaluate the polarization contribution with simulated spectra. We simulated a profile with reflectivity of both crystals in three cases: unpolarized, σ polarization and π polarization.
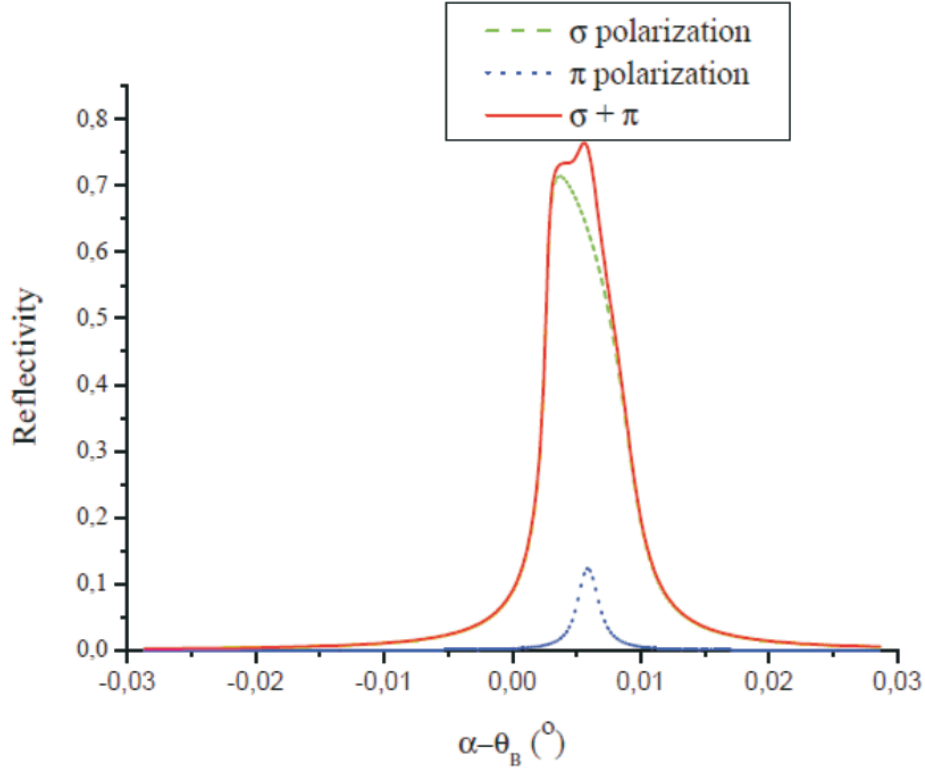
Figure 6.8: Reflectivity profiles of the Si(111) crystals obtained with the XOP code. The σ and π polarization profiles are shown by the green and blue lines respectively along with an unpolarized profile (red line) obtained by summing both polarization profiles [157].

We compared the simulated profiles to experimental data and we noticed excellent agreement for the unpolarized case. The agreement for the σ-polarized was only slightly worse since the reflectivity for the π case is much weaker than for the σ case. The worst agreement was for the case of the π-polarization since the reflectivity curve for this case is very narrow, so that the simulated spectra were much narrower than experimental ones. Therefore, we estimate the effect of polarization as the energy difference between the simulations with the unpolarized case and the σ-polarized case, obtaining 1 meV. One also should note that with π-polarized x rays we would not have been able to observe any line, as the integrated reflectivity for a single crystal for π-polarization is 6% of the σ-polarization. That would lead to roughly 230 times fewer counts.

6.3.3   X-ray detection

A xenon (90 %) and methane (10 %) gas filled proportional counter detector is mounted on the table with an axis of rotation concentric with the second crystal vertical axis. The detector has a 50 μm thick Be window and an active area of about 12 by 25 mm and is charged to its operating high voltage of about 2000 V by an external power supply. The detector signal is processed by a preamp, a 142AH ORTEC amplifier and a gated signal adopted for the approximate X-ray energy to be measured and counted by a computer card controlled by Labview^{TM}. The detector thresholds are adjusted for the specific line energy being measured. The motors of both crystals, the detector and both encoders are controlled by a Labview^{TM} interface. The same interface also allows to start scans of the second crystal while the first crystal is steady and record spectra as well as the temperature of both crystals as a function of time.

6.4 Temperature Control

The role of the surface temperature of the crystals in the DCS can be easily understood from the Bragg law [Eq. (6.1)], in which the lattice spacing d is directly tied to the Bragg angle. The average interatomic distance of the Si atoms in the lattice is correlated with their kinetic energy and hence with their temperature. As pointed before, the dilatation coefficient provided by NIST for the Si(111) crystals used in our setup is $2.56 \times 10^{-6} \ °C^{-1}$. The correct measurement of the surface crystal temperature is then essential in obtaining a reliable lattice spacing that translates to a correct line energy. Because $\frac{\Delta E}{E} = \frac{\Delta d}{d} = 2.56 \times 10^{-6}$, for each degree that the measured temperature strays from the real temperature, the obtained energy will be off by 2.56 ppm, which can be a serious problem when trying to study energy transition values at the ppm level.

In the measurements made in previous years, the temperature was not controlled and the measured values could drift several degrees over the course of a full measurement day. Later, a proportional-integral-differential (PID) controller, whose output is connected to a heater inserted in a copper sandwich pressed to the back of the crystal was installed on the apparatus. The PID chosen is a Jumo Dicon 500 with parameter self-optimization. The self-optimization procedure provided by Jumo works really well when the experiment is running at atmospheric pressure, but when in vacuum the optimization procedure resulted in incorrect PID parameters, which made the system oscillate with very high temperature amplitudes, sometimes higher than 10 °C. We can see this behaviour in Fig. 6.9 in which a 0.9 °C variation for the first crystal temperature was measured with the self-optimized parameters for a 16 hour survey. In order to properly calculate the temperature effects in the experimental
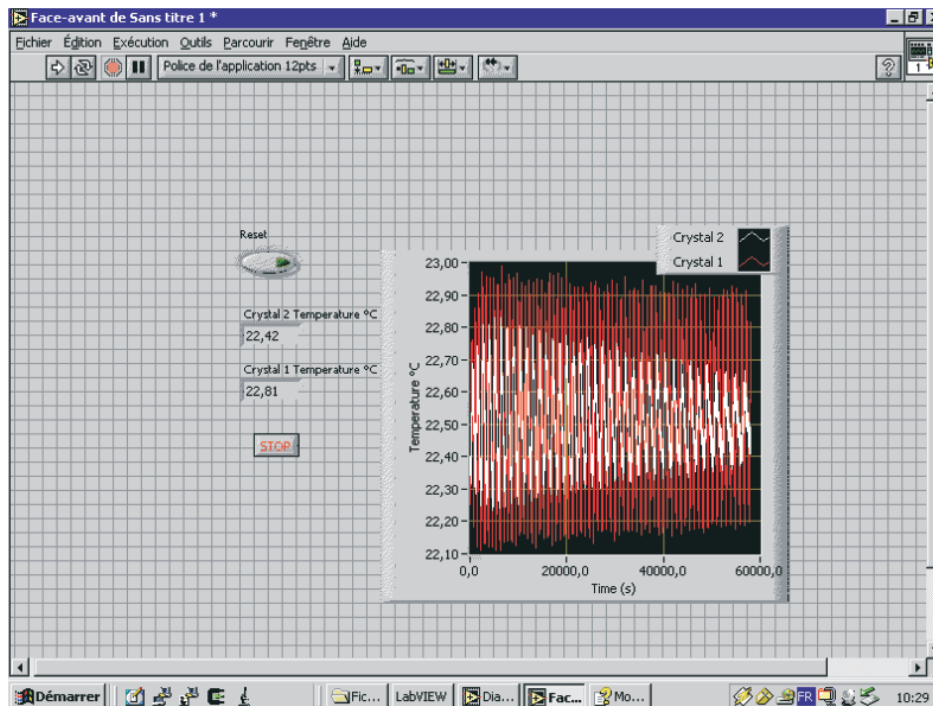
Figure 6.9: Temperature recorded with the DCS running during a 16 hour period with the self-optimized PID parameters

spectra, not only should we keep the temperature oscillation to a minimum but we should also record the instant temperature information during the whole scan time. This goal was fulfilled by connecting the Jumo 500 via a RS422 serial interface to the control computer and by improving the Labview code used to run the experiment. The communication protocols from the PID controller were not very well described in the manual but through a very

time-consuming investigation of the input/output strings we were able to conclude that the protocol used was indeed a Modbus protocol with a CRC16 checksum. Having solved the communication problem, we focused on the modification of the Labview code. Because the final spectrum is a sum of individual spectra whose duration and number of bins can be chosen, a new histogram was developed in which the average temperature recorded for each bin was kept (usually the scan takes 5 to 10 seconds in each bin). The average temperature and standard deviation during the whole scan is also kept. In order to deal with the temperature oscillation problem we had to optimize the PID parameters ourselves, and the Ziegler-Nichols method [176] was used. In our case, we can only properly control the system when the temperature is higher than the reference value, because there is no cooler in the crystals, only a heater. Although the method works best for a two-way controller in which both regimes, higher and lower than the reference value, are controlled, we used the method as a starting point for a manual tuning. The final PID parameters were chosen in such a way that the settling time was less than 30 minutes and the overshoot wouldn't be more than 10%. After the tuning, several temperature records were taken with different experimental settings and in the time range of a single scan the variation of the temperature was less than 0.1 °C. Nevertheless, the cooling system of the encoder motors wasn't enough to keep the system at a 22.5 °C for the entire duration of a measurement and the temperature started drifting up very slowly giving way to a 0.2 °C variation in the course of a full measurement day. A screenshot of the modified Labview front panel is shown on Fig. 6.10, featuring the temperature measurement and all of the measured properties.
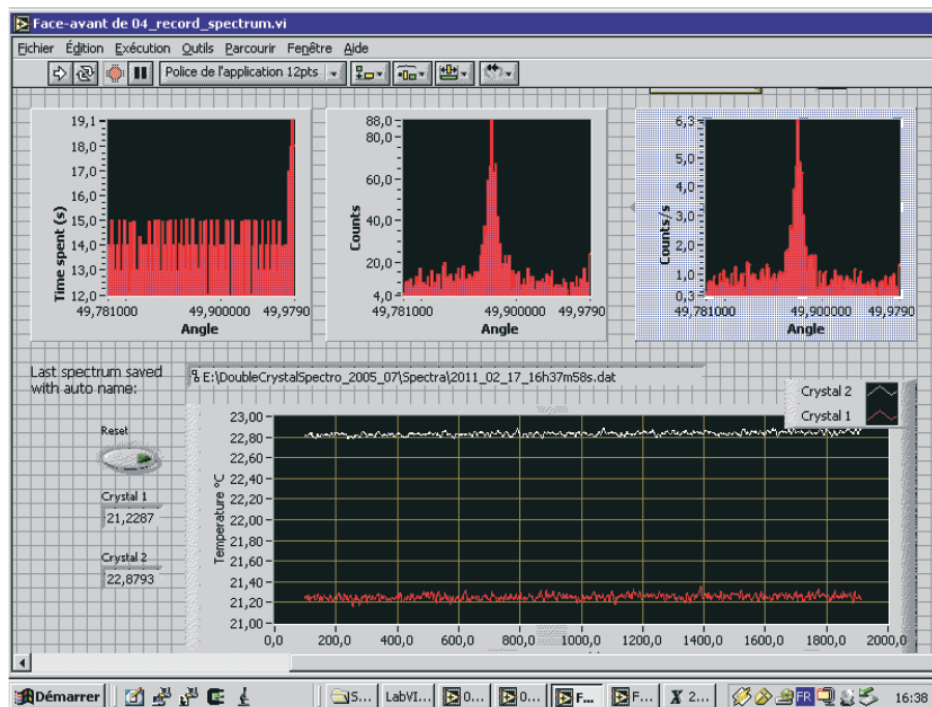
Figure 6.10: Labview front panel of the DCS measurement control. Featured are the histograms regarding the angular measurements and the temperature of the two crystals.

6.4.1 Temperature Miscalibration

The first measurements made for the "relativistic" $M1$, after the temperature control had been installed, showed an energy value 200 meV above the previous ones, which indicates that maybe the temperature measurement was wrong. After ruling out all other possible sources of error, the conclusion was that somehow the temperature was being misread. The

temperature sensors were calibrated by Jumo to better than 0.05 °C in that temperature region. The temperature sensor was pressed to the front of the crystals by a strand of tape, and we considered the hypothesis that the temperature conduction from one surface to another could be made by the air molecules between them, which vanish when the system is in vacuum. In order to investigate this, we inserted one sensor in the back of the crystal tightly pressed between the copper sandwich and the crystal back. The results obtained are presented in Fig. 6.11. We can see that the heat conduction is at the core of this
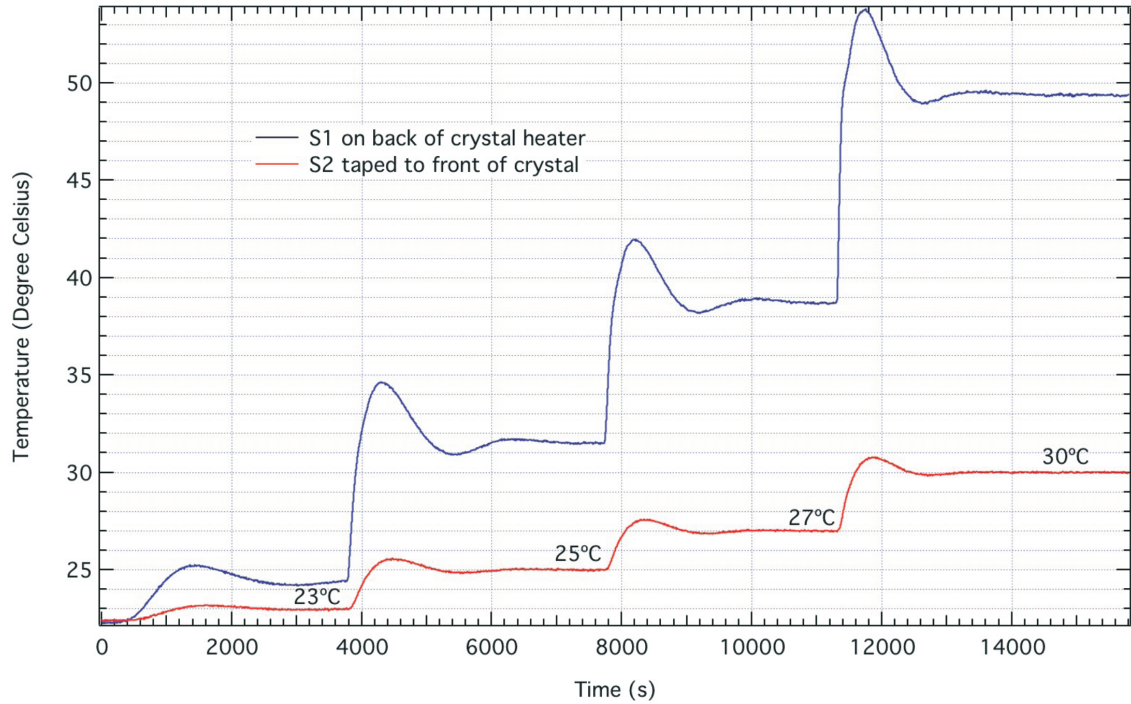
Figure 6.11: [Front-to-back measured crystal temperatures. The blue line corresponds to a temperature measurement at the crystal heater, while the red line corresponds to the temperature at the crystal surface. The measurement was performed in order to do two or three degrees steps at the crystal surface in each hour.

miscalibration, and after increasing the surface contact by tightly pressing the sensor on the front with a clip system and using the PID with the back sensor instead of the front one, the front-to-back temperature differences decreases dramatically as can be seen on Fig. 6.12. A calibration of the front-to-back temperature difference was then performed and both sensors were connected to the copper sandwich at the back of the crystal (see Fig. 6.13). The recorded temperature for each scan was then modified accordingly. To account for this bad thermal contacts under vacuum, we use a final uncertainty for the temperature measurement of 0.5 °C which corresponds to 1.29 ppm, almost dominating the error budget. The use of infrared temperature sensors pointed to the crystal surface could dramatically improve the uncertainty.
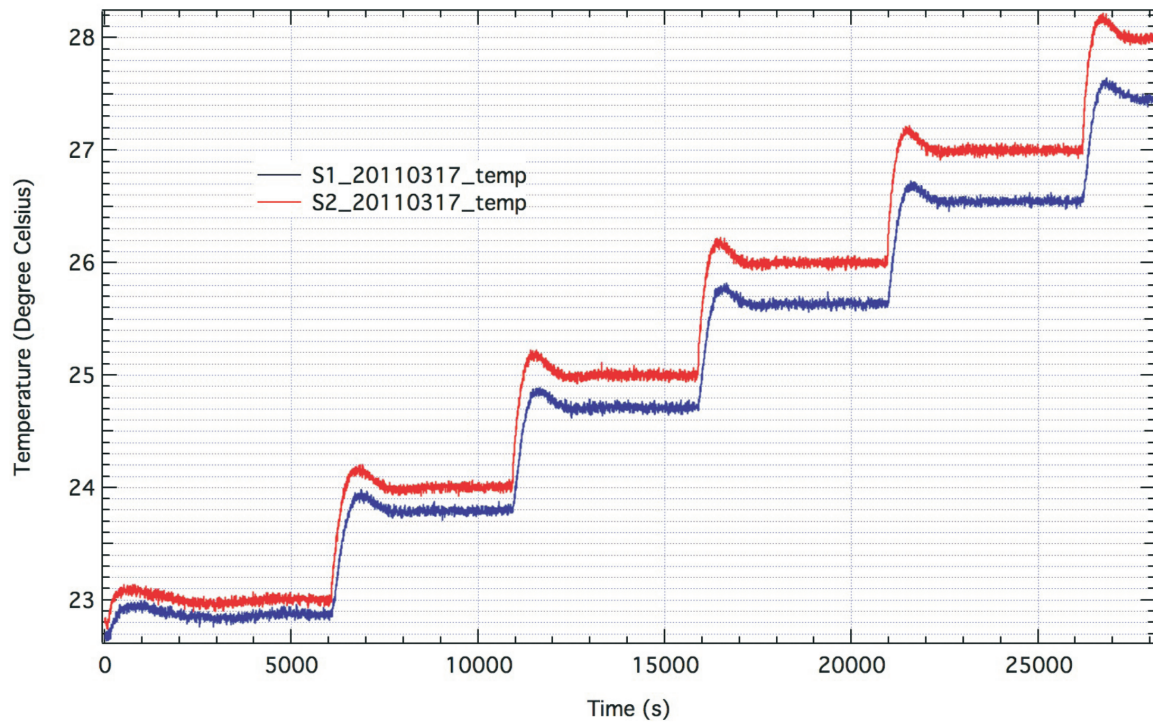
Figure 6.12: Front-to-back measured crystal temperatures with good heat conduction. The red line corresponds to a temperature measurement at the crystal heater with the controlled sensor, while the blue line corresponds to the temperature at the crystal surface.
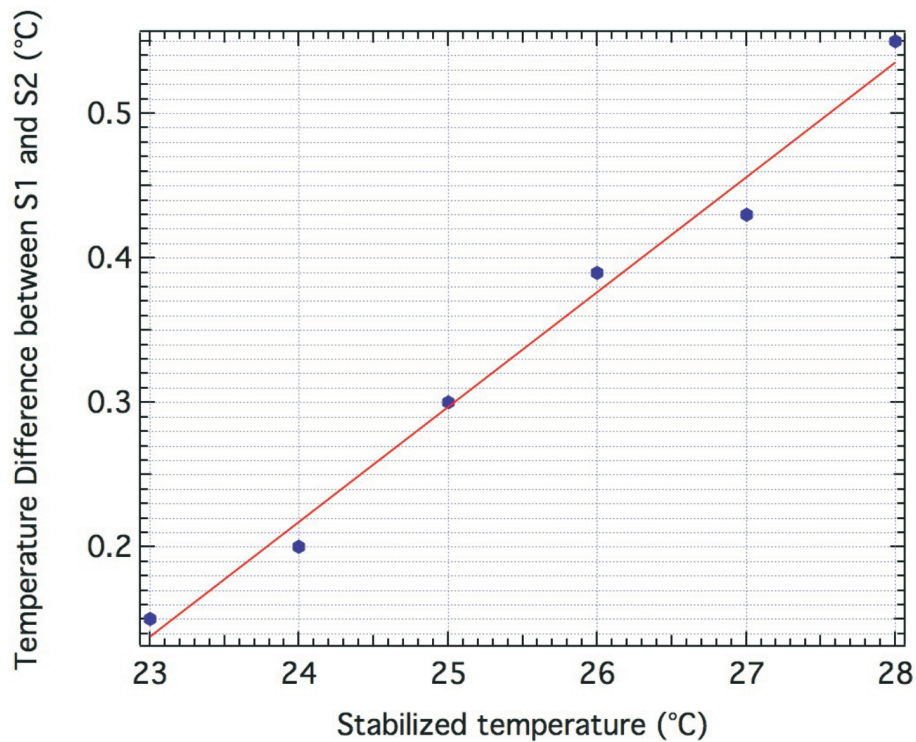
Figure 6.13: Front-to-back temperatures calibration used for correcting the recorded average temperatures in a scan.

Chapter 7

Radiative Transitions on He-Like Ar

7.1 Measurement of the "'Relativistic M1"' Transition Energy in He-like Ar

The double-flat crystal X-ray spectrometer coupled to the electron-cyclotron-resonance ion-source described in the previous section was used in this work with the goal of performing measurements of several atomic properties of highly charged ions for the first time. Among the measurements performed are absolute (reference-free) energies of radiative transitions of heliumlike to boronlike argon ions. The design of the DCS, shown on Chapter 6, allows measurements of transition energies without reference to any theoretical or experimental energy, being tied only to the definition of the meter, as a transfer standard through the lattice spacing of the crystals. The two Si (111) crystals were made and measured at the National Institute of Standards and Technology (NIST) in Gaithesburg. Their lattice spacing in vacuum was found to be $d = 3.135601123(81)$Å at a temperature of 22.5 °, using the NIST lattice spacing comparator, calibrated against a known standard crystal (see [145, 174] and Refs. therein). This method allows the avoidance of difficulties associated with existing X-ray standards such as broad, asymmetric lines from core-excited neutral elements, sensitive to excitations and chemical effects [73, 156]. We have measured the $1s2s\ ^3S_1 \rightarrow 1s^2\ ^1S_0$ "relativistic $M1$" transition energy in heliumlike argon with a 2.5 ppm accuracy. The $M1$ transition was chose due to its very narrow natural width [177, 178] of $\approx 10^{-7}$ eV, completely negligible when compared to the instrument response function. We can thus directly probe for the first time the shape of the response function in that energy range in both the dispersive and non-dispersive modes.

To analyse the experimental spectra, a Monte-Carlo based simulation code was developed by Amaro [157], which performs an exact ray tracing using the geometry of the instrument and of the X-ray source, the shape of the crystal reflectivity profile, as well as the line width and Gaussian Doppler broadening. The effect of the X-ray beam vertical divergence is then described exactly and not by an approximate formula as in previous works. A very thorough description of the systematic errors of the DCS, the alignment procedure and the simulation design can be found on Ref. [157]. The reflectivity profile used in the simulation is calculated using the X0P program [175], which uses dynamical diffraction theory and the latest values for the index of refraction and lattice spacing for Si(111) crystals provided by NIST. The result was also checked with another program, X0h [179, 180], and the differences are negligible. The index of refraction in XOP at 3104.148 eV is 5.100×10^{-5}. The semi-empirical value from Ref. [181] is 5.079×10^{-5}. We use this difference as an error bound for this correction. The simulation is used not only for investigating the systematic errors, but also to provide line shapes that can in the end be compared to the measured spectra. From that procedure we can gather information on the correct energy of the transition as well as on the instrument

response function, line broadening effects and natural widths. An example of a non-dispersive spectrum obtained in this work can be seen in Fig. 7.1. The fit can be performed either with a Voigt profile or a simulated profile. On the non-dispersive or parallel side, both fits give the same peak position although the reduced χ^2 is lower if the fit is done with a simulated profile, resulting in $\chi^2 \approx 1.2$. This value shows the near perfect quality of the crystals and their cut, as well as the almost exact description of the experimental geometry within the simulation. On the dispersive side, for which an experimental spectrum can be seen in Fig. 7.2, the

Figure 7.1: Parallel spectrum made at a first crystal position optimized for the $M1$ with a acquisition time of 943 s.

geometrical constraints such as the collimation resulting from the polarization electrode and the first crystal angle, as well as the reflectivity of both crystals, results in a profile that is slightly asymmetric. Hence, a small shift is obtained if we use a Voigt profile or a simulated profile that translates into a 14 meV (4.6ppm) energy shift. To our knowledge, this is the first time that such a shift is observed and it has never been taken into account in previous X-ray standard measurements reported in the latest X-ray energy tables [73]. In order to study systematic errors, a series of spectra were recorded over a period of several months, at different temperatures, with slightly different first crystal angles and ECRIS operating conditions. The microwave power, gas composition and ion extraction voltage were varied to check their influence on the line energy. No dependence on the first crystal angle or ECRIS parameters was observed other than the change in X-ray intensity due to the collimation effects described in the previous section.

To obtain the transition energy from the spectra, two distinct methods were used. A Voigt profile was fitted to both the dispersive and non-dispersive spectra, as well as to high statistic simulated spectra. The experimental energy was then deduced from the energy used as an input for the simulation corrected for the difference in angle and temperature. In a second method, the simulated profiles were directly used to fit the experimental lines and
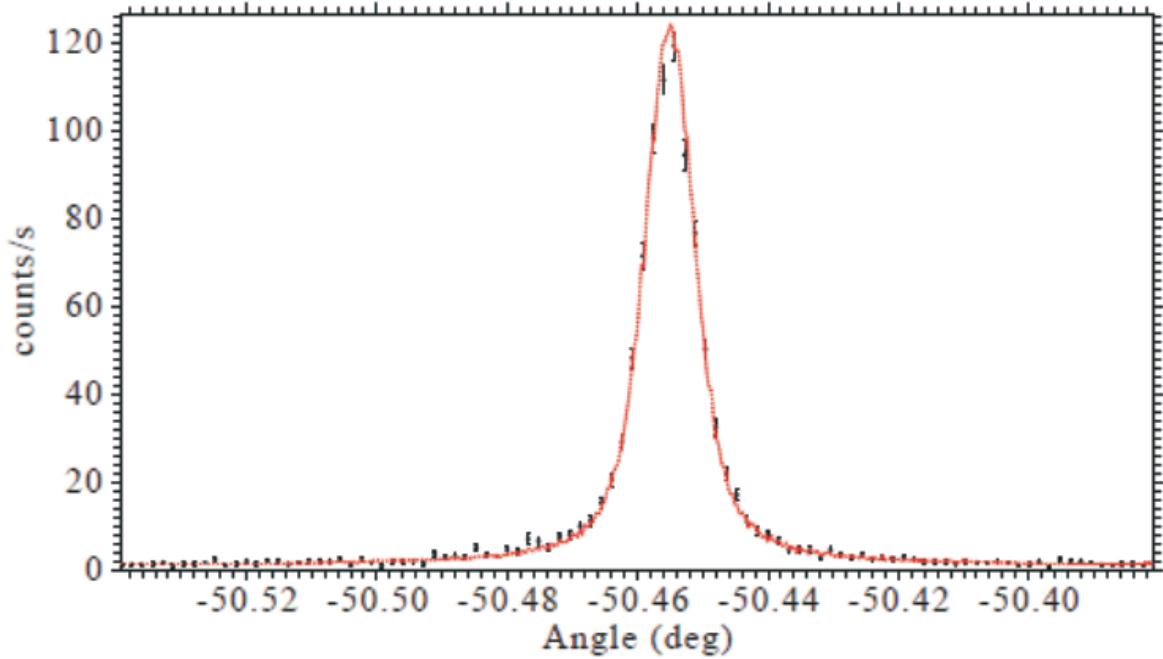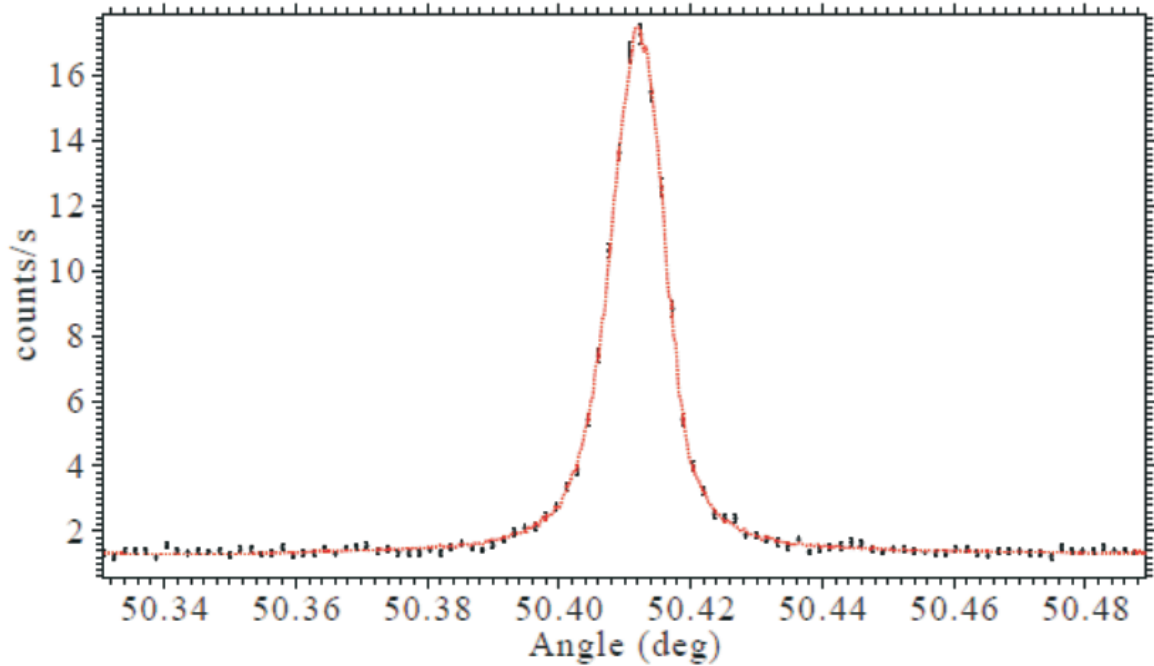
Figure 7.2: Antiparallel spectrum made at a first crystal position optimized for the $M1$ with a acquisition time of 18239 s.

obtain a Bragg angle from which the line energy was deduced. Both methods provide the same result to high accuracy.

The dependence of the energy values obtained on the crystal temperatures is represented in Fig. 7.3. Weighted one- and two-parameter linear fits have been performed. The difference between the value at 22.5 °C obtained with those fits are combined to get an estimate of systematic errors. The list of contributions to the uncertainty is shown in Table 7.1. The uncertainty is limited by statistics, angle and temperature measurements. Possible contamination from satellite transitions, originating from $1s2sn\ell, n > 2$ levels must be low: some satellite lines should be resolved and seen outside of the $M1$ line, yet none can be observed. This is because the $n\ell$ electron decays by $E1$ transitions faster than the $2s$ one. The final value for the $M1$ transition energy is 3104.1605(78) eV, i.e., an accuracy of 2.5 ppm. The comparison with theoretical results is shown in Table 7.2. The theoretical result of Artemyev *et al.* [182] is 1.6 σ below the experimental value. The list of contributions included in Ref. [182] and their uncertainty is also shown in Table 7.2. Our experimental accuracy is 0.7% of the one-electron QED corrections, and 7.4% of the self-energy correction to the electron-electron interaction. The finite size correction represents 2.7 ppm of the transition energy, barely larger than our uncertainty. Its uncertainty cannot influence the comparison between theory and experiment in this case.

7.2 Line Widths of Transitions in Heliumlike Argon

The emission of radiation from an atomic transition does not result in a strictly monochromatic spectral line, but rather in an energy distribution around the central transition energy value, E_0. This gives rise to a line profile $I(E - E_0)$ with a full-width half-maximum, which not only depends on the spectral resolution of the measuring apparatus but also on intrinsic physical properties such as the lifetimes of the atomic states involved in the transition, the

Table 7.1: Contributions to the uncertainty of the $M1$ transition energy measurement at a 68% confidence interval.

Contribution	Value (eV)	Value (ppm)
Fit and extrapolation	0.0044	1.42
Angle encoder error	0.0036	1.16
Lattice spacing error	0.0001	0.03
Index of refraction	0.0016	0.52
X-ray polarization	0.0010	0.32
Coefficient of thermal expansion	0.0002	0.06
Modeling error and alignement	0.0030	0.97
Energy-wavelength correction	0.0001	0.03
Temperature (0.5 °C)	0.0040	1.29
Total	0.0078	2.51

Table 7.2: Comparison between theoretical calculations and experiment (eV). Individual contributions are from Ref. [182]. Older calculations are updated for fundamental constants in Ref. [145]. The MCDF calculation follows Refs. [183, 184].

Contribution	$1s^2\ ^1S_0$	$1s2s\ ^3S_1$	Transition
Dirac	-4427.4154(3)	-1108.0563	3319.3591(3)
ΔE_{int}	305.6560	91.3873	-214.2687
ΔE_{1el}^{QED}	1.1310(1)	0.1525	-0.9785(1)
ΔE_{2el}^{QED}:			
Scr. SE	-0.1116	-0.0154	0.0962
Scr. VP	0.0072	0.0010	-0.0062
2-ph.exch.	0.0091(1)	-0.0004(1)	-0.0095(2)
ΔE_{ho}^{QED}	0.0009	0.0003	-0.0006
ΔE_{rec}	0.0575	0.0141	-0.0434
Total [182]	-4120.6653(4)	-1016.5169(1)	3104.1484(4)
MCDF [185]			3104.171
Drake [186]			3104.138
RMBPT [187]			3104.189
RMBPT [177]			3104.06(19)
Experiment			3104.1605(78)
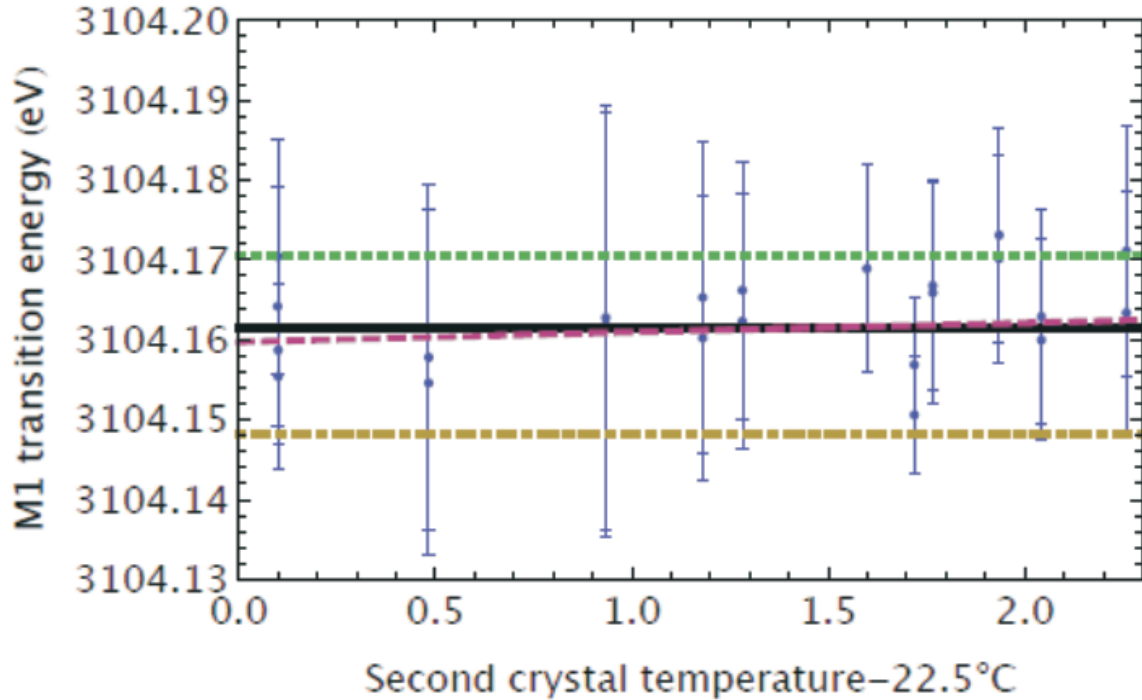
Figure 7.3: One and two parameter extrapolation of the $M1$ transition energy to the standard temperature (22.5 °C). Each data point corresponds to the energy deduced from a one-day measurement, a sequence of three spectra like the ones in Figs. 7.1 and 7.2, performed successively in dispersive, nondispersive and dispersive mode, for a given temperature. The error bars correspond to the statistical errors from the fits. Solid line: one parameter extrapolation, dashed line: two parameter extrapolation, dot-dashed line: Ref. [182], dotted line: MCDF calculation (see Table 7.2).

velocity distribution of the moving atoms or ions and the pressure or collision rate of the sample. The energy levels of atoms and/or ions have an energy uncertainty related to their finite lifetime, which can be understood from the Heisenberg uncertainty principle. From the classical description of a spontaneous emission as a damped oscillation, a frequency profile can be obtained through a Fourier transformation which results in a spectral line with a Cauchy-Lorentzian distribution. In the physics community this distribution is known either as a Lorentzian or Breit-Wigner profile [188].

Several effects contribute to the broadening of the natural widths of transition energy profiles. Depending on the design of the measuring apparatus their influence can be suppressed or enhanced. The most important broadening mechanisms are the following:

- **Doppler Broadening** - Atoms in a gas or ions in a plasma move with a mean velocity v, depending on their mass and on the temperature of the gas or plasma. The direction and module of the velocity of the radiation emitting atoms and ions result in a Doppler-shift of the transition frequency. The convolution of this process with a Maxwell-Boltzmann distribution at a given temperature for the gas or plasma results in a Gaussian function symmetric around the transition energy value.

- **Collision Broadening** - Every atom or ion in a gas or plasma interacts with other neighbouring atoms and/or ions. The electrostatic or Van-der-Walls forces actuate to shift the atomic energy levels. Since this interaction decreases with increasing distance between the interacting atoms or ions, the level shifts increase with the density or pressure of the gas or plasma. Some collisions may even be inelastic, in which some

or all of the de-excitation energy can be transferred to another atom, shortening the effective lifetime of the excited state and hence broadening the line profile. Unlike the Doppler broadening, the collision broadening not only increases the line width but can also shift the line position.

7.2.1 Doppler Broadening of the Ar ions in the ECRIS Plasma

As explained in the previous section, the sensitivity to small changes and asymmetry of the lines measured in the DCS at SIMPA is unique. Due to the very small natural width of the M1 line, much smaller than the instrument energy response function, and to all our purposes considered monochromatic, we were able to investigate the Doppler broadening due to the temperature of the Ar ions inside the plasma. Several high statistic simulations were performed for the M1 transition in which the Lorentzian width of the input rays was set to zero and the Gaussian width was scanned at regular intervals from zero to 400 meV. For each of the dispersive measurements performed with the DCS, a fit was made with all the different Gaussian width simulated profiles. The reduced χ^2, given by Eq. (7.1), was recorded for every different width spectra,

$$\chi^2_{\mathrm{red}} = \frac{1}{\nu} \sum_{i=1}^{N} \left(\frac{f\left(x_i\right) - f_{\mathrm{sim}}\left(x_i, A, x_0\right)}{\sigma_i} \right)^2.$$

(7.1)

Here, $f\left(x_i\right)$ is the measured experimental data, $f_{\mathrm{sim}}\left(x_i, A, x_0\right)$ is the simulated theoretical data, A and x_0 are the fitting parameters, A being the intensity of the peak and x_0 the center of the peak. σ_i is the variance of the observation and ν is the number of degrees of freedom, given by $N - n$, where N is the number of data points and n the number of fitted parameters, which in this case is 2. This way we get a representation of the reduced χ^2 as a function of the Gaussian width w inserted in the simulation. This function, $\chi^2_{\mathrm{red}}(w)$, can be fitted with a quadratic expression and we can then find its minimum, corresponding thus to the Gaussian width that effectively minimizes the reduced χ^2. We have also calculated the standard deviation σ_w, for which we have a 68% chance of finding the experimental value in the interval $[w - \sigma_w; w + \sigma_w]$. In Fig. 7.4 a graphic is shown with this procedure for a measured M1 spectrum. This procedure is then repeated for every one of the 13 recorded spectra and a final averaged value of 80.5(4.6) meV (FWHM) was found for the Doppler broadening. From the Doppler broadening we can infer the temperature of the ions inside the plasma as well as the electron density. As said before, the ions in the ECRIS are trapped in a space charge distribution created by the electrons in the plasma. Assuming that the electrons in the source are on a sphere [131] with 3 cm diameter, and that the plasma chamber, being metallic, enforces a zero potential at the boundary, we can solve the Poisson equation for the electrons, assuming constant density. We then get a quadratic potential, corresponding to the space charge, with a depth proportional to the electron density.

The relativistic Doppler shifted energy of the $M1$ photons emitted by the Ar^{16+} ions in the plasma can be written as a function of the angle θ between the velocity v of the ion and the line connecting the ion and the observer, the relativistic $\beta = v/c$ and the energy of the $M1$ photon

$$E_{\mathrm{Dopp}}\left(E_0, \beta, \theta\right) = \frac{E_0 \sqrt{1 - \beta^2}}{1 - \beta \cos\left(\theta\right)}.$$

(7.2)

Taking the two extreme cases in which the ion is travelling straight towards the observer ($\theta = 0$) and away from it ($\theta = \pi$), we can obtain from the measured broadening of 80.5 meV a value of the relativistic β of $1.29664687 \times 10^{-5}$. This corresponds to a maximum velocity of the trapped ions $v = 3887 \ \mathrm{ms}^{-1}$ and an energy $E = 3.13$ eV. Solving the Poisson equation
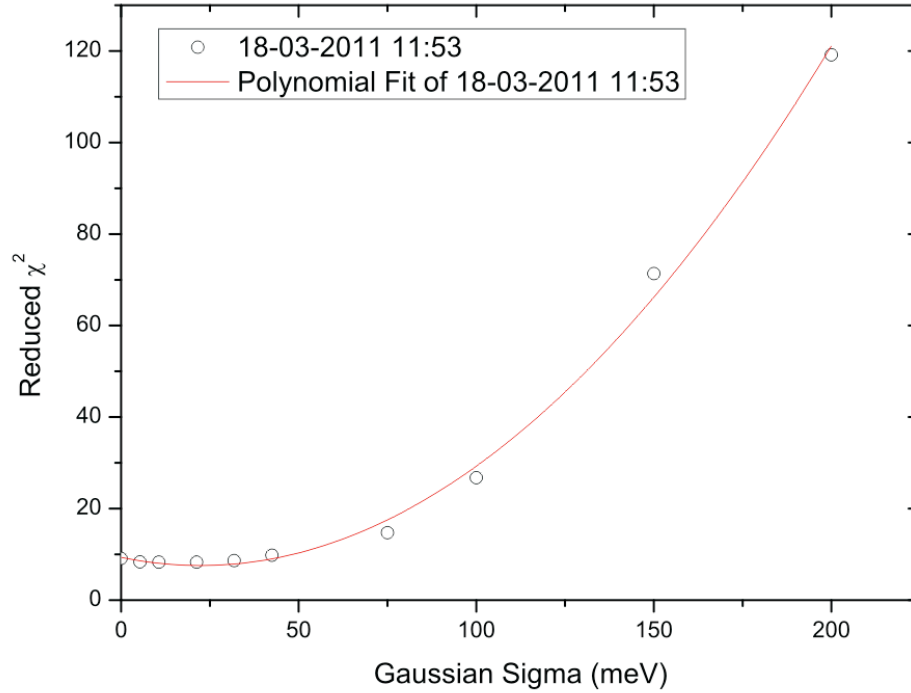
Figure 7.4: Reduced χ squared as a function of the Gaussian sigma calculated using a voigt fit for a particular $M1$ measurement.).

[Eq. (7.3)] for the center of the plasma sphere ($r = 0$)

$$-\frac{de}{6\epsilon 0}\left(R^2 - r^2\right) = -\frac{E}{q} \tag{7.3}$$

where e is the charge of the electron, $\epsilon 0$ is the vacuum permittivity, R is the radius of the plasma sphere, E is the energy of the Ar^{16+} ions and q is their charge, we get an electronic density $d = 7.2 \times 10^{10}$ particles/cm^3. Comparing to the average electronic density obtained for a krypton [131] gas in the SIMPA ECRIS of 5 to 30 $\times 10^{11}$ particles/cm^3 and to the value obtained by Adrouche [189] for an Ar plasma in the same ECRIS of 1.13×10^{11}, we conclude that this method is actually a very elegant way of obtaining ionic temperatures and electronic densities in ECRIS plasmas. As can be seen, the very low ionic temperature of 3 eV is in complete agreement with the ionic temperatures obtained in the ECR survey of Drentje [162].

7.2.2 Measurement of the He-like Diagram Line $1s2p$ $^1P_1 \rightarrow 1s^2$ $^1S_0$ Spectral Width

Having investigated the Doppler broadening of the He-like Ar ions inside the ECRIS plasma, we can then turn to the He-like $1s2p$ $^1P_1 \rightarrow 1s^2$ $^1S_0$ diagram line. In the Doppler broadening calculation, performed in the previous section, we set the natural width of the line to zero because we were measuring a magnetic dipole line, which to all purposes could be considered monochromatic. For this line, we can assume that the Doppler broadening remains unchanged, which is sensible because the ion generating the transition is the same. Hence, we can perform the same analysis as before, but instead of performing simulations with zero natural widths and a range of Gaussian widths, consider a fixed value of the gaussian width and a range of natural widths. The Gaussian width is set to 80.5 meV and the Lorentzian

75

Table 7.3: Natural widths of the 7 measurements of the He-like Ar diagram line. The dates of the measurements, its standard deviations and reduced χ^2_{min} are also presented.

Measure Date	Natural width w_{min} (meV)	Uncertainty at 68% (meV)	Reduced χ^2_{min}
23/05/11	21.63	47.02	1.230
24/05/11	105.34	24.23	0.975
25/05/11	89.13	34.54	1.0647
26/05/11	100.71	21.27	1.135
30/05/11	47.67	30.99	1.18
01/06/11	89.50	24.89	1.058
03/06/11	36.29	26.91	1.007
	Average Width	Std. Dev.	
Results	$w_{\mathrm{av}} = 79.08$ meV	$\sigma_w = 10.40$ meV	

width is then scanned around the expected theoretical value of 70.4 meV. Simulations with high statistics for Lorentzian widths ranging from zero to 200 meV were performed and fits were made to the 7 measurements of the diagram line. In Table 7.3, the minimum Lorentzian widths, its standard deviation and the reduced χ^2 are presented for each of the line measurements. The expected natural width of the $1s2p\ ^1P_1 \rightarrow 1s^2\ ^1S_0$ line of 70.4 meV is within the $w_{av} = 79.08 \pm 10.40$ meV obtained interval, which once again proves that this method can be thoroughly used to calculate radiative and auger transition widths for highly charged ions as well as electronic densities and ionic temperatures for ECRIS plasmas. Nevertheless, an increase of the number of measurements for this line should provide greater insight by reducing the uncertainty of the width measurements.

Chapter 8

Analysis of an Ar X-ray spectrum from an ECRIS plasma

8.1 X-ray spectrum from an Ar plasma

One of the main problems of ECRIS plasmas diagnostics is the determination of the ion charge-state distribution inside the plasma. Several articles from our group [8, 9, 122] have shown that the analysis of high resolution X-ray spectra is an excellent tool to estimate the ion charge state distribution (CSD) inside an ECRIS plasma. In 2001, Martins *et al.* [8] performed a detailed analysis of a K X-ray spectrum emitted by Ar ions in a ECRIS plasma. In that first work they showed that a complete analysis of these spectra called for a careful examination of all excitation and ionization processes that lead to the excited states of the different ionic species whose decay will yield the detected lines. In the same work, the relevant atomic parameters were calculated for each charge state but a single average energy for the electrons in the plasma was used. Also, the lack of multi-ionization processes in the analysis was later proven [9] to be insufficient to explain all the features present in the spectrum. The inclusion of double-KL and triple-KLL ionization accounts for many of the low intensity peaks as was shown later in the study of sulfur plasmas [9, 122]. A re-evaluation of Ar plasma X-ray spectra is thus in order. We are anticipating the need to fully develop a reliable way for obtaining the CSD for any plasma and, from a realistic CSD obtained from the extracted ions for example, check the theoretical intensities of some lines of interest. In this way we can choose carefully what transitions to target with the DCS given all the experimental restrictions.

8.2 Processes of Creation and Decay of Highly Excited States in an ECRIS

In this section, we have used the methodology of Santos *et al.* [9] and inserted some of their derivations to better understand the overall procedure. The process used to estimate the ion CSD includes the following steps:

1. The spectrum of characteristic X-rays from ions inside the plasma was measured;

2. The excited states that produce the X-ray spectrum were identified;

3. The main processes leading to these excited states, from the ground configurations, were found and the corresponding cross sections were calculated, using a physically justified electron distribution function;

4. Radiative and radiationless transition energies and probabilities of the identified transitions were obtained from the previous work of Martins *et al.* [190];

5. The real peak intensities of the measured spectra were obtained by simulating iteratively the lines positions, intensities and widths until the overall reduced χ^2 is minimized;

6. From the comparison of the peak intensities in the corrected theoretical and the measured experimental spectrum we arrive at the ion charge-state density ratios.

In this work, we assume that the ions in a ECRIS are in their ground configurations, since the lifetimes of the excited configurations are orders of magnitude lower than the collision times for K excitation and K, KL, KLL ionization. However, there are some metastable states, like the $1s^22s2p\ ^3P_0$ state in Be-like ions, which could live long enough to be considered as alternative ground states. The processes that occur in X-ray emission from ECR sources can range from electronic inner-shell ionization and excitation, dielectronic recombination, charge exchange reactions, radiative recombination and radiative and radiationless decays. For highly charged ions, dielectronic recombination, charge exchange and radiative recombination rates are usually low when compared to the dominant inner-shell ionization and excitation and radiative and radiationless decays [6].

8.2.1 Transition Energies and Probabilities

The very high energy accuracy in the DCS experimental spectra calls for very sophisticated theoretical methods for the calculation of transition energies. The importance of knowledge of precise transition energy values cannot be overemphasized and the correlation contribution to transition energies is very important in few electron ions, which makes the use of multiconfiguration or configuration-interaction approaches very useful. Electrons in highly charged ions, especially in inner shells, are, in general, highly relativistic, so a relativistic calculation is required. Finally, quantum-electrodynamics effects (QED) such as the electron self energy and vacuum polarization must, in general, be taken into account. Radiative and radiationless transition energies, transition probabilities and fluorescence yield values for the Ar isonuclear series calculated with the MCDFGME code can be found on Ref. [190].

8.3 Distribution of Electron Energies in the Plasma

Because the plasma generated within an ECRIS is a cold plasma in which the electron temperature and ion temperature differ, the resulting electron temperature is strongly non-Maxwellian and can, in principle, be represented by two populations [137]: a cold one with energies up to 10 keV, and a hot one with energies of several tens of keV; the latter being well confined inside a closed egg-shaped surface centered around the source main axis. Barué *et al.* [137] and Gumberidze *et al.* [131] studied the energy distribution of the hot electrons inside ECRIS devices by observing the bremsstrahlung and electron cyclotron emission.

The cold electrons can be considered approximately Maxwellian whereas the hot electrons distribution must differ from the Maxwellian distribution. Following the work of Pras *et al.* [133], we set the global electron distribution $f(E)$ as a linear combination of the Maxwellian, $f_{\mathrm{Mw}}(E)$, and the non-Maxwellian, $f_{\mathrm{NMw}}(E)$, energy distributions.

Let N_e, $v(E)$ and $\sigma(E)$ be the electron density, the electron velocity and the cross section for a given process, respectively, at a specific electron energy E, then the quantity $\langle N_e\sigma v\rangle$ is the rate of the number of events related to a process (excitation or ionization), averaged over

the electron distribution energy, and is defined by

$$
\begin{aligned}
\langle N_e \sigma v \rangle &= N_e \int_{E_{\min}}^{\infty} v(E)\, \sigma(E)\, f(E)\, dE \\
&= N_e \int_{E_{\min}}^{\infty} v(E)\, \sigma(E)\, [(1-x)\, f_{Mw}(E) + x f_{NMw}(E)]\, dE,
\end{aligned}
\tag{8.1}
$$

where x is a mixing coefficient.

In order to evaluate the integral in Eq. (8.1), the cross sections for all the processes considered must be calculated for a wide range of energies, from threshold, $E_{\min}$, to infinity, which is an impossible task if the cross sections for the processes considered are not given in an analytical form. Although the ionization cross sections can be obtained through a simple analytical expression, as the work performed in the first part of this thesis asserts, the excitation cross sections cannot be obtained in a reliable analytical form.

Fortunately, the mathematical expression for the electron distributions used here is well suited for the use of Gauss-Laguerre integration. With this method, only a small number of cross section values, usually 7 to 20, are needed to calculate each process, each charge state and each temperature value.

8.3.1 Gauss-Laguerre integration

The Gauss-Laguerre integral form is

$$
\int_0^{\infty} e^{-x} f(x)\, dx \approx \sum_{i=1}^{n} w_i f(x_i),
\tag{8.2}
$$

where x_i is the ith root of the Laguerre polynomial $L_n(x)$, and the weight w_i is given by

$$
w_i = \frac{x_i}{(n+1)^2 \, [L_{n+1}(x_i)]^2}.
\tag{8.3}
$$

8.3.1.1 Maxwell distribution

In order to apply the Gauss-Laguerre integration method, we need to write the integral

$$
\int_{E_{\min}}^{\infty} f_{\mathrm{Mw}}(E)\, v(E)\, \sigma(E)\, dE,
\tag{8.4}
$$

in the form

$$
\int_0^{\infty} e^{-x} g(x)\, dx.
$$

The Maxwell energy distribution function is given by,

$$
f_{\mathrm{Mw}}(E, T) = \frac{2}{\sqrt{\pi}} \frac{E^{\frac{1}{2}}}{(kT_{\mathrm{cold}})^{\frac{3}{2}}} e^{-\frac{E}{kT_{\mathrm{cold}}}},
\tag{8.5}
$$

where E is the kinetic energy of the electrons, T is the thermodynamical temperature, and k is the Boltzmann constant. If we use the relativistic form of E, we can write the electrons velocity as

$$
v = cE^{\frac{1}{2}} \frac{(E + 2mc^2)^{\frac{1}{2}}}{(E + mc^2)},
\tag{8.6}
$$

and Eq. (8.4) transforms to [9]

$$
\int_{E_{\min}}^{\infty} f_{\mathrm{Mw}}(E)\, v(E)\, \sigma(E)\, dE = \frac{2c}{\sqrt{\pi}\, (kT_{\mathrm{cold}})^{\frac{3}{2}}} \int_{E_{\min}}^{\infty} E e^{-\frac{E}{kT_{\mathrm{cold}}}} \frac{(E + 2mc^2)^{\frac{1}{2}}}{(E + mc^2)} \sigma(E)\, dE.
\tag{8.7}
$$

Considering that

$$z = E - E_{\min},$$

Eq. (8.7) becomes

$$\int_{E_{min}}^{\infty} f_{\mathrm{Mw}}(E)\, v(E)\, \sigma(E)\, dE$$

$$= \frac{2ce^{-\frac{E_{min}}{kT_{\mathrm{cold}}}}}{\sqrt{\pi}\,(kT_{\mathrm{cold}})^{\frac{3}{2}}} \int_{0}^{\infty} (z + E_{min})\, e^{-\frac{z}{kT_{\mathrm{cold}}}} \frac{(z + E_{min} + 2mc^2)^{\frac{1}{2}}}{(z + E_{min} + mc^2)} \sigma(z + E_{min})\, dz. \quad (8.8)$$

Changing variables,

$$x = \frac{z}{kT_{\mathrm{cold}}} \rightarrow z = xkT_{\mathrm{cold}} \rightarrow dz = kT_{\mathrm{cold}}dx, \quad (8.9)$$

Eq. (8.8) assumes the form,

$$\int_{E_{min}}^{\infty} f_{\mathrm{Mw}}(E)\, v(E)\, \sigma(E)\, dE = \frac{2ce^{-\frac{E_{min}}{kT_{\mathrm{cold}}}}}{\sqrt{\pi}\,(kT_{\mathrm{cold}})^{\frac{1}{2}}} \int_{0}^{\infty} e^{-x} g(x)\, dx, \quad (8.10)$$

where

$$g(x) = (xkT_{\mathrm{cold}} + E_{min}) \frac{(xkT_{\mathrm{cold}} + E_{min} + 2mc^2)^{\frac{1}{2}}}{(xkT_{\mathrm{cold}} + E_{min} + mc^2)} \sigma(xkT_{\mathrm{cold}} + E_{min}). \quad (8.11)$$

8.3.1.2 Non-Maxwell distribution

Performing the same way for the non-Maxwellian energy distribution, $f_{\mathrm{NMw}}(E)$, the integral,

$$\int_{E_{min}}^{\infty} f_{\mathrm{NMw}}(E)\, v(E)\, \sigma(E)\, dE, \quad (8.12)$$

needs to be transformed accordingly. Concerning the non-Maxwellian electron energy distribution, we follow the suggestion of Celata [191] and use the relativistic version of the Dory-Guest-Harris expression [137, 192],

$$f_{\mathrm{NMw}}(E, T) = C_n E \left(1 + \frac{E}{2mc^2}\right) \left(1 + \frac{E}{mc^2}\right) e^{-\frac{E}{kT_{\mathrm{hot}}}}, \quad (8.13)$$

where

$$C_n = \frac{1}{(kT_{\mathrm{hot}})^2} \frac{1}{1 + 3\alpha + 3\alpha^2} \qquad \text{and} \qquad \alpha = \frac{kT_{\mathrm{hot}}}{mc^2}. \quad (8.14)$$

Substituting this form of f_{NMw} into Eq. (8.12) leads to

$$\int_{E_{min}}^{\infty} f_{\mathrm{NMw}}(E)\, v(E)\, \sigma(E)\, dE$$

$$= \frac{C_n c}{2\,(mc^2)^2} \int_{E_{min}}^{\infty} E^{\frac{3}{2}} \left(E + 2mc^2\right)^{\frac{3}{2}} e^{-\frac{E}{kT_{\mathrm{hot}}}} \sigma(E)\, dE. \quad (8.15)$$

Considering that

$$z = E - E_{min} \rightarrow dE = dz,$$

Eq. (8.15) becomes

$$\int_{E_{\min}}^{\infty} f_{\mathrm{NMw}}(E)\, v(E)\, \sigma(E)\, dE$$

$$= \frac{C_n c e^{-\frac{E_{min}}{kT_{\mathrm{hot}}}}}{2\,(mc^2)^2} \int_{0}^{\infty} (z + E_{min})^{\frac{3}{2}} \left(z + E_{min} + 2mc^2\right)^{\frac{3}{2}} e^{-\frac{z}{kT_{\mathrm{hot}}}} \sigma(z + E_{min})\, dz. \quad (8.16)$$

Performing the variable change

$$x = \frac{z}{kT_{\text{hot}}} \rightarrow z = xkT_{\text{hot}} \rightarrow dz = kT_{\text{hot}}dx, \tag{8.17}$$

we transform Eq. (8.16) to

$$\int_{E_{min}}^{\infty} f_{\text{NMw}}(E) \, v(E) \, \sigma(E) \, dE = \frac{C_n c \, (kT_{\text{hot}}) \, e^{-\frac{E_{min}}{kT_{\text{hot}}}}}{2 \, (mc^2)^2} \int_0^{\infty} e^{-x} g(x) \, dx, \tag{8.18}$$

with

$$g(x) = [x(kT_{\text{hot}}) + E_{min}]^{\frac{3}{2}} \left[x(kT_{\text{hot}}) + E_{min} + 2mc^2\right]^{\frac{3}{2}} \sigma\left[x(kT_{\text{hot}}) + E_{min}\right]. \tag{8.19}$$

8.3.2 Electron Impact Ionization

8.3.2.1 Electron Impact Single Ionization

The expression developed in the first part of this work fulfils perfectly the requirements of the electron impact single ionization cross sections needed to simulate an ECRIS plasma. The ability to model ionizing events that cover incident electron energies from the threshold to relativistic values with a minimal input data, and its analytical nature, makes Eq. (3.13) ideally suited to be applied in this method.

8.3.2.2 Electron Impact Multiple Ionization

In this work we have included double KL- and triple KLL-ionization processes from the ions ground configurations. The binary encounter formalism can be applied to multiple ionization, but as noted by Vriens [47], the fact that multiple hard collisions are needed to express the multiple ionization processes in the binary encounter model, leads to an increasing underestimation of the cross section as the number of collisions is increased. Although the fact that such an expression, free of empirical parameters is ideal for this method, the dramatic drop in accuracy of the model for multiple ionization makes it impossible to use. For the calculations of the double and triple ionization cross sections we have used the semi-empirical formula of Shevelko and Tawara [193], with the fitting parameters proposed by Bélenger *et al.* [194], which, to our knowledge, is the only analytical expression that provides cross sections for multiple ionization processes. This expression, in S.I. units reads

$$\sigma_n = \frac{a(n) \, N^{b(n)}}{(I_n/R)^2} \left(1 - \frac{I_n}{T}\right)^c \frac{\ln(T/I_n)}{T/I_n} \times 10^{-22}, \tag{8.20}$$

where T is the incident electron energy in eV, I_n is the combined ionization energy of the KL, or KLL electrons, N is the total number of electrons in the target atom, n is the number of electrons to be ionized and R is the Rydberg energy in eV. The fitting parameters a, b and c were evaluated from experimental data and are $a(2) = 14.0$ and $b(2) = 1.08$ for the removal of two electrons, and $a(3) = 6.30$ and $b(3) = 1.20$ for the removal of three electrons [194]. The c parameter should be set as unity, $c = 1$, for neutral atoms and $c = 0.75$ for ions. This expression was developed for the multiple ionization of the outermost electrons, so its accuracy cannot be fully granted for inner-shell ionization. Because the expression works best for multiple ionization of the outer electrons, Shevelko and Tawara suggested that the parameter I_n should be calculated as the sum of the consecutive first ionization energies of the chain of generated ions, i.e., the combined ionization energy of a given atom I_n is calculated as

$$I_n = \sum_{i=0}^{n-1} B_i, \tag{8.21}$$

where B_i are the lowest electron binding energies of the atoms with charge states i. For example, for the Kr atom we have $B_0 = 13.993916$ eV, $B_1 = 24.728224$ eV, $B_2 = 37.053620$ eV, $B_3 = 50.995085$ eV, corresponding to the first ionization energies of the elements Kr, Kr^+, Kr^{2+} and Kr^{3+} respectively. Hence, for the removal of 4 electrons from the neutral Kr atom by electron impact, the combined ionization energy $I_4 = 13.99 + 24.73 + 37.05 + 50.99 = 126.76$ eV.

For the selective multiple ionization of KL and KLL electrons, indispensable for this work, we have used the MCDFGME code to obtain the total energy of the configurations involved in the feeding mechanisms for these processes, and the total multiple ionization energy was calculated as the difference between the total energies of those configurations. Because the energy region of interest comprises transitions from combinations of electronic configurations with two to four electrons with a K hole, we calculated the single, double and triple ionization energy values presented in Table 8.1.

Table 8.1: Ionization Energies for the K, KL and KLL Ionization of Ar.

Ionization Type	Initial Configuration	Final Configuration	Ionization Energy (eV)
	$1s^2 2s^2 2p$	$1s 2s^2 2p$	3842.3588
K	$1s^2 2s^2$	$1s 2s^2$	3941.7821
	$1s^2 2s$	$1s 2s$	4030.5030
	$1s^2 2s^2 2p^2$	$1s 2s^2 2p$	4518.3296
	$1s^2 2s^2 2p^2$	$1s 2s 2p^2$	4518.3296
KL	$1s^2 2s^2 2p$	$1s 2s 2p$	4693.0492
	$1s^2 2s^2 2p$	$1s 2s^2$	4693.1201
	$1s^2 2s^2$	$1s 2s$	4872.0409
	$1s^2 2s^2 2p^3$	$1s 2s^2 2p$	5137.0839
	$1s^2 2s^2 2p^3$	$1s 2s 2p^2$	5137.0839
	$1s^2 2s^2 2p^3$	$1s 2p^3$	5189.7335
KLL	$1s^2 2s^2 2p^2$	$1s 2s 2p$	5379.3080
	$1s^2 2s^2 2p^2$	$1s 2s^2$	5379.3790
	$1s^2 2s^2 2p^2$	$1s 2p^2$	5414.2007
	$1s^2 2s^2 2p$	$1s 2s$	5628.0626
	$1s^2 2s^2 2p$	$1s 2p$	5647.0496

8.3.3 Electron Impact Excitation

Electron impact excitation cross sections can be found in several sources, from scientific papers to atomic databases [195, 196], for a wide number of atoms and ions. However, the sheer volume of data necessary for plasma diagnostic, specially on a large energy range makes the use of published excitation cross sections inappropriate. The use of an analytical expression for the calculation of excitation cross sections is better suited than other *ab initio* calculations because of the number of transitions involved and the energy intervals for which the values are needed. Estimates of electron-impact excitation cross sections are frequently provided by the Fisher *et al.* expression [197], which is based on the van Regemorter expression for bound-bound electron excitation [198]. Nevertheless, the use of this formula is questionable for ions, because it was derived for neutral atoms and also because it only takes into account electric dipole transitions. Sampson and Zhang tested extensively the Regemorter expression and concluded that for $\Delta n \geq 1$ excitation transitions from levels with $\ell < n - 1$, the expression is frequently found to be a very poor approximation [199]. On the other hand, accurate excitation cross sections can be calculated from computer codes such as the MCDFGME of

Desclaux and Indelicato [50, 51] or the GIPPER package of Archer *et al.* [127] that uses the atomic structure code of Cowan [127, 200]. The MCDFGME code uses multiconfiguration Dirac-Fock wave functions for the bound electron, Dirac wave functions for the free electron and the first Born approximation for the electron impact excitation cross section. The GIP-PER code uses the muticonfiguration Hartree-Fock method of R. D. Cowan for obtaining the wave functions, and the electron impact excitation cross sections are calculated using the distorted wave approximation. The use of such atomic structure programs is useful because they calculate also other atomic parameters needed for modelling x-ray spectra from ECRIS plasmas. Although the cross section values calculated with such codes are not continuous in energy, the Gauss-Laguerre integration method, shown above, solves this complication, and usually only 20 points in the energy grid are needed for the calculation of the $\left\langle N_e v \sigma_i^{K-exc,q} \right\rangle$ quantities. As in electron impact ionization, the existence of a reliable, easy-to-use, analytical expression for the computation of excitation cross sections, would prove an excellent improvement on the method proposed thus far.

8.4   Calculation of Line Intensities

For the calculation of the balance equation we need to consider all the processes leading to a given ion in the charge state $q = Z - m$, m being the number of bound electrons in the atom. However, depending on the energy region of the spectra we might be probing essentially inner-shell transitions. In this work we are mainly concerned with ions with K holes in several excited states, and we assume that the ions are initially in their ground configuration. The balance equation for a process leading to an ion in charge state q with a K hole in the excited level i, is given by [9]

$$N_0^q \left\langle N_e v \sigma_i^{K-\text{exc},q} \right\rangle + N_0^{q-1} \left\langle N_e v \sigma_i^{K-\text{ion},(q-1,q)} \right\rangle$$
$$+ N_0^{q-2} \left\langle N_e v \sigma_i^{K-\text{double-ion},(q-2,q)} \right\rangle$$
$$+ N_0^{q-3} \left\langle N_e v \sigma_i^{K-\text{triple-ion},(q-3,q)} \right\rangle = N_i^{K,q} A_i^q, \tag{8.22}$$

where A_i^q is the level i decay probability by any process (radiative and radiationless), $N_0^{q'}$ is the ion density in the ground configuration for the ions with charge state q'. The excitation cross section for the process leading from an ion in the charge state q in the ground configuration to its excited level i with a K hole is represented by $\sigma_i^{K-\text{exc},q}$. The single-, double- and triple-ionization cross sections of the processes leading from ions with positive charge q' ($q' = q - 3, ..., q$) in their ground configuration, to the excited state i of the ion with charge q and a K hole, are represented, respectively, by $\sigma_i^{K-\text{ion},(q-1,q)}$, $\sigma_i^{K-\text{double-ion},(q-2,q)}$ and $\sigma_i^{K-\text{triple-ion},(q-3,q)}$. $N_i^{K,q}$ is the density of ions in the charge state q, with a K hole and in the level i. All $\langle N_e \sigma v \rangle$ quantities are calculated using Eq. (8.1). The $\sigma_i^{K-exc,q}$ values are obtained by summing the individual cross sections for the processes leading from each level j of the X^{q+} ion ground configuration, to the excited level i of the same ion with a K hole, weighted by the statistical weight g_j of each j level of the ground configuration. Concerning ionization, the cross section of the process leading from the $X^{(q-n)+}$ ($n = 1, 2, 3$) ions in the ground configuration to the X^{q+} ion with a K hole, are multiplied by the statistical weight g_i of the level i, yielding the K-shell ionization cross sections $\sigma_i^{K-\text{ion},(q-n,q)}$. These cross sections are calculated with Eqs. (3.13) and (8.20) for the single and multiple ionization processes respectively. Finally, the intensity of the line corresponding to the transition of an ion with charge q and a K-shell hole from the level i to the level j is given by

$$I_{ij}^q = \hbar \omega A_{ij}^q N_i^{K,q}, \tag{8.23}$$

where $\hbar\omega$ is the transition energy, A_{ij}^q is the probability of the $i \to j$ radiative transition, and $N_i^{K,q}$ is obtained by evaluating Eq. (8.22). In order to fully reproduce an experimental spectra, all possible excitations as well as single- double- and triple- ionization processes must be included in the evaluation of Eqs. (8.1), (8.22) and (8.23). All possible processes leading from the ground configuration of He-like to N-like ions to excited states of He-like to Be-like ions, with a K hole, are shown in Fig. 8.1. De-excitation processes for the resulting excited ions are also illustrated schematically in the same figure.
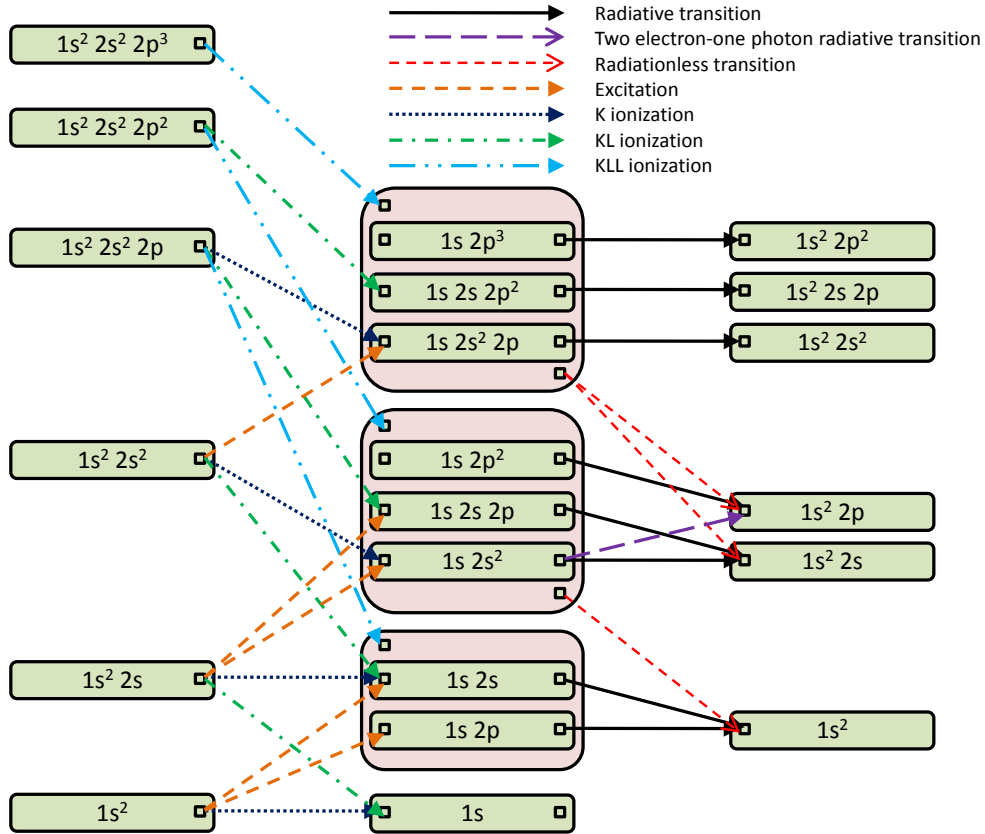
Figure 8.1: Excitation, ionization and decay processes considered in the analysis of HCI spectra. K excitation, dashed line; single K ionization, dotted line; double KL ionization, dash-dotted line; triple KLL ionization, dash-dot-dot line; radiative decay, solid line and radiationless decay, small-dash line.

8.5   Analysis of an Ar Plasma with the DCS

For metrology purposes, all the transitions measured independently were angle optimized in order to get the highest intensity of the particular line being investigated. However, in order to perform plasma diagnosis, relative intensities of transitions from several charge state Ar ions are needed. Because of the DCS geometry it is impossible to use separate single measurements of different transitions for charge state distribution calculations. For this purpose, a wide second crystal scan was performed for a fixed first crystal angle, containing several features arising from Ar^{14+} up to Ar^{16+} ions. Using the procedure described above we were able to obtain a theoretical spectrum, from which, upon comparison, we could extract iteratively the charge state distribution of the Ar ions inside the ECRIS plasma.

8.5.1 DCS Wide Spectrum

As was mentioned before, the use of a DCS with an ECRIS source is a *state of the art* way of measuring both transition energy values and also natural widths of de-excitations in HCI. However, regarding the intensity of the peaks obtained, the use of a double-flat spectrometer raises some problems. As pointed out earlier, the number of X-rays reaching the detector depends not only on the balance between the feeding mechanisms and the radiative transitions of the plasma species, but also on the geometrical settings of the DCS. The Monte Carlo ray tracing simulation code of Amaro [157] is used to estimate the intensity dependence of the angular region of the second crystal for a fixed first crystal angle. An expression which relates the normalized intensity of the radiation as a function of the second crystal angle is then obtained. In order to compare the experimental DCS spectrum with the theoretical simulated spectrum we have to multiply the theoretical spectrum with the normalized intensity angular function.

For the geometrical experimental settings, measured and optimized through a series of procedures that can be found in Amaro's PhD thesis [157], the obtained function is an hyperbole. The parameters of this function depend on the shape of the collimator between the plasma and the first crystal and on the vertical divergence of the crystals. For this particular energy region and first crystal angle, the best hyperbolic fit can be seen in Fig. 6.7 on Sec. 6.3 and has a normalized expression given by

$$I(E) = 1.04815 - 6.27647 \times 10^{-5} \sqrt{|588509 + 690026(E - 3103.89)^2|}. \tag{8.24}$$

8.5.2 Interpretation of the X-ray Spectrum Emitted by Ar ions in an ECRIS plasma

In order to analyse the DCS spectrum we have considered all radiative transitions that fell into the $[3087, 3120]$ eV energy region, which corresponds mainly to lines arising from Ar^{14+}, Ar^{15+} and Ar^{16+} ions. The required parameters for this group of transitions were obtained from Ref. [190]. The computational method for the calculation of bound state wavefunctions and radiative transition probabilities was the general relativistic MCDF method developed by Desclaux and Indelicato [50, 51]. The multiconfiguration approach is characterized by the fact that a small number of configurations can account for a large amount of correlation. All intra-shell correlation was included. Details of the method can be found, for instance, in [69, 70]. The so-called optimized level (OL) method was used to determine the wavefunction and energy for each state involved. Thus, spin-orbitals in the initial and final states for the radiative transitions are not orthogonal, since they have been optimized separately. This non-orthogonality effect is fully taken into account [178, 201], using the formalism proposed by Löwdin [202].

The length gauge has been used for all radiative transition probabilities. Radiationless transition probabilities were calculated using Desclaux's code [203]. The bound wavefunctions were generated using this code for configurations that contain one initial inner-shell vacancy while the continuum wavefunctions were obtained by solving the Dirac-Fock equations with the same atomic potential of the initial state. With this treatment, the continuum wavefunctions are made orthogonal to the initial bound state wavefunctions, thus assuring orthogonality. No orbital relaxation is included.

The continuum wavefunction is normalized to represent one electron per unit time. Altogether, energies and probabilities of 28 transitions were found to sit in the spectrum's energy range. The transitions considered in this work were the ones originating from the $1s2s$ and $1s2p$ configurations to the final configuration $1s^2$ for the He-like Ar ions, the $1s2s2p \rightarrow 1s^22s$ transitions for the Li-like ions and the $1s2s^22p \rightarrow 1s^22s^2$ and $1s2s2p^2 \rightarrow 1s^22s2p$ for the Be-like ions. The most prominent features in the spectrum are the Be-like $1s2s^22p\ ^1P_1 \rightarrow 1s^22s^2\ ^1S_0$ line labelled in Figs. 8.2 and 8.3 as 1), the relativistic M1 transition of the He-like

Ar $1s2s\ ^3S_1 \to 1s^2\ ^1S_0$ labelled as 2) and the Li-like $1s2s2p\ ^2P_{1/2,3/2} \to 1s^22s\ ^2S_{1/2}$ doublet, which corresponds to numbers 3) and 4). All of the considered processes are represented in Fig. 8.1, where all the feeding mechanisms can be also seen. As discussed before we have considered that all the ionic species are in their ground state configurations prior to the excitation/ionization mechanisms. Particularly, we have excluded the possibility of the Be-like like ions to be in the metastable states of the $1s^22s2p$ configuration because of the low lifetimes of such states compared to the collision times for excitation and ionization of the K, KL and KLL electrons. Comparing the obtained theoretical spectrum with the DCS wide spectrum (see Figs.8.2 and 8.3) we see that all of the main features are accounted for. We have used for each line a linear combination of a Lorentzian and a Gaussian distribution,

Figure 8.2: Wide scan spectrum of Ar ions in the SIMPA ECRIS plasma using a DCS. Normalized theoretical spectrum convoluted with the DCS intensity distribution, solid line; Normalized theoretical spectrum, dotted line; Experimental DCS wide spectrum, full circles.

designed to approximate a Voigt profile. Because of the very high sensitivity to the spectral shapes of the transitions measured in the DCS, every one of the main peaks seen in the spectrum was fitted independently with Voigt profiles. The obtained width parameters of the pseudo-Voigt fits were then used in the theoretical spectrum in order to better fit the overall spectrum. The simulated spectrum was normalized to the $M1$ intensity and the final DCS normalized spectrum is obtained by further multiplying the theoretical normalized spectrum with Eq. (8.24). We can immediately see from the shift in the highest peak that the calculated energy of 3091.95 eV, for the $1s2s^22p\ ^1P_1 \to 1s^22s^2\ ^1S_0$ transition, is somewhat higher than the experimental energy value of 3091.7669(38) eV. The small bump to the left of the Be-like line, labelled as 5) in Figs. 8.2 and 8.3, which corresponds to a transition energy of around 3090.2 eV, probably arising from the $1s2s2p^2\ ^1S_0 \to 1s^22s2p\ ^1P_1$, is not present in the theoretical spectrum, mainly because of the absence of excitation and K-shell ionization feeding mechanisms leading to the $1s2s2p^2$ configuration. This is due to the fact
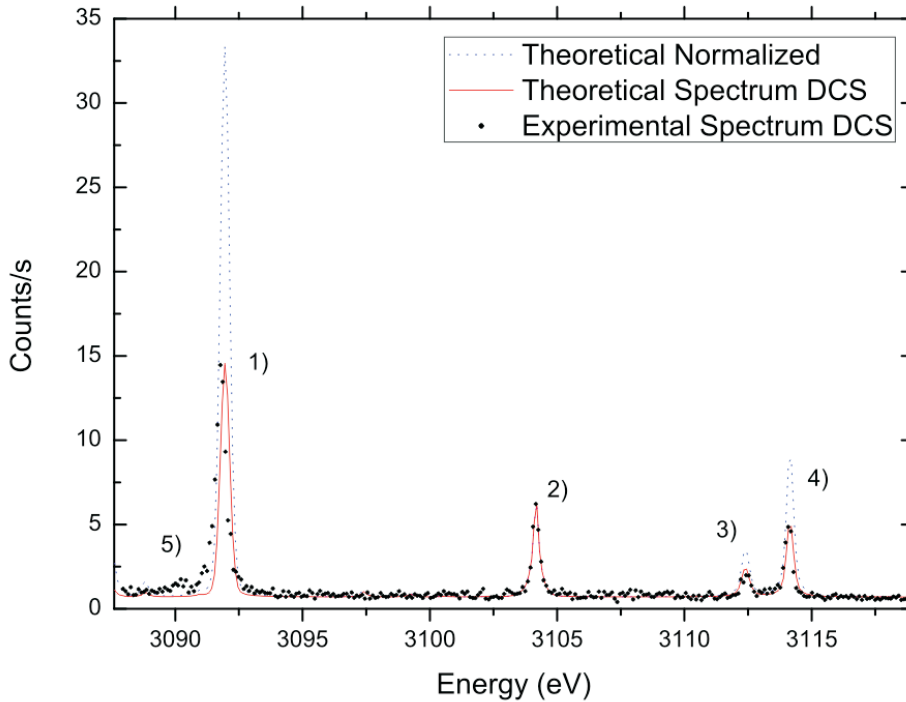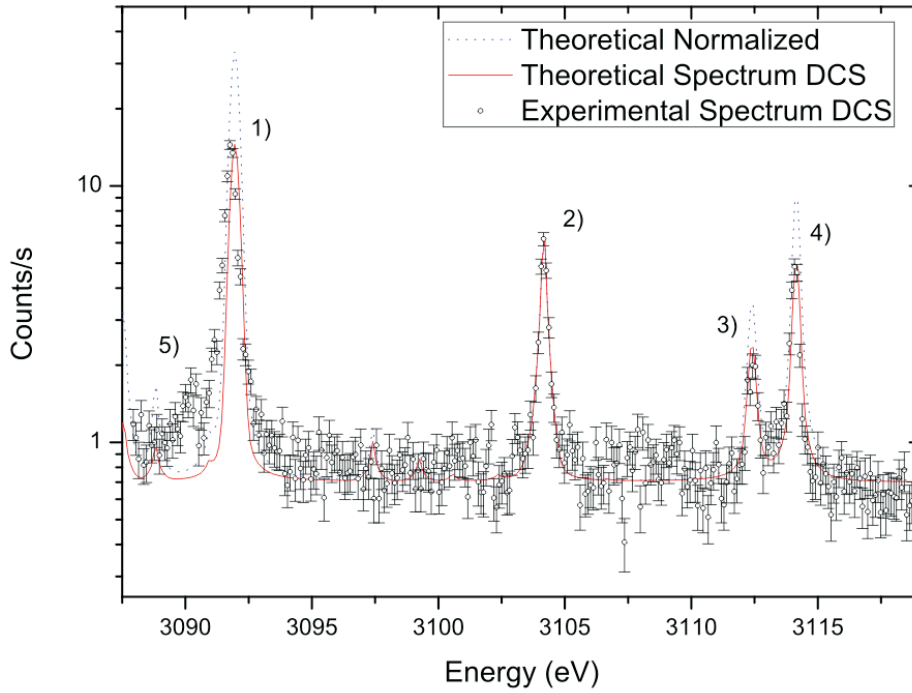
Figure 8.3: Logarithmic scale view of the DCS wide scan spectrum of Ar ions in the SIMPA ECRIS plasma. Normalized theoretical spectrum convoluted with the DCS intensity distribution, solid line; Normalized theoretical spectrum, dotted line; Experimental DCS wide spectrum, open circles.

that all starting configurations were chosen to be on the ground state. The fact that this observed line is not present on the simulated spectrum leads us to the conclusion that maybe this metastable state can live long enough to be K-shell excited or ionized. Because we don't know the ratios of the ground $1s^2 2s^2$ to the metastable $1s^2 2s 2p$ state and the ground $1s^2 2s^2 2p$ to the metastable $1s^2 2s 2p^2$ state, we are not able to calculate the excitation cross sections for the $1s^2 2s 2p \rightarrow 1s 2s 2p^2$ process nor the K-shell ionization cross section for the $1s^2 2s 2p^2 \rightarrow 1s 2s 2p^2$ process. Hence, only through double and triple ionization can this states be created, which results in a much lower intensity of the observed X-ray radiation than the states that are fed through both excitation and K, KL and KLL ionization. This feeding mechanisms play a very important role in the observation of certain decay channels. For example, although the $1s 2s\ ^3S_1 \rightarrow 1s^2\ ^1S_0$ relativistic $M1$ transition has a very low transition rate, of more than 7 orders of magnitude lower than the Li-like and Be-like lines, the fact that the $1s 2s$ configuration can be created by K-shell excitation and ionization as well as by double KL and triple KLL excitation from the ground state configurations $1s^2$, $1s^2 2s$, $1s^2 2s^2$ and $1s^2 2s^2 2p$ respectively, results in a very high intensity radiative transition. Comparing to the dipole allowed $1s 2p\ ^1P_1 \rightarrow 1s^2\ ^1S_0$ diagram line, that has a transition rate of 8 orders of magnitude higher than the $M1$ line, but can only be created by K-shell excitation from the $1s^2$ ground configuration and by triple KLL ionization from the $1s^2 2s^2 2p$ ground state configuration, the observed intensity is less than half of the relativistic $M1$ line. In the Table 8.2 we present all of the transitions that fall in the spectrum energy range. The initial and final configurations are shown, as well as the transition energies and rates and the radiative transition yields. The transition yields are calculated as the ratio of the radiative transition

87

probability to the sum of the transition probabilities of radiative and Auger de-excitations. Other decay channels such as dielectronic recombination, charge exchange and collisional de-excitation have not been included in the transition yield calculation because these processes are very rare in such cold plasmas.

Table 8.2: Energies and transition rates and yields for all of the transitions included in the simulated theoretical Ar plasma spectrum.

Ar ion charge	Initial Configuration	LSJ_i	Final Configuration	LSJ_f	Transition Energy (eV)	Transition Rate (s^{-1})	Radiative Trans. Yield
16+	1s2p	$^3P_1$	$1s^2$	$^1S_0$	3123.37	1.81×10^{12}	1.00×10^0
16+	1s2s	$^3S_1$		$^1S_0$	3104.17	4.78×10^6	1.00×10^0
15+	1s2s2p	$^2P^1_{1/2}$	$1s^22s$	$^2S_{1/2}$	3112.40	8.65×10^{13}	7.32×10^{-1}
15+		$^2P^2_{1/2}$		$^2S_{1/2}$	3125.37	1.97×10^{13}	1.65×10^{-1}
15+		$^2P^1_{3/2}$		$^2S_{1/2}$	3114.15	1.00×10^{14}	9.12×10^{-1}
15+		$^2P^2_{3/2}$		$^2S_{1/2}$	3125.9	6.77×10^{12}	5.62×10^{-2}
15+		$^4P_{1/2}$		$^2S_{1/2}$	3086.69	1.64×10^{11}	9.47×10^{-1}
15+		$^4P_{3/2}$		$^2S_{1/2}$	3087.55	4.50×10^{11}	9.83×10^{-1}
14+	$1s2s^22p$	$^1P_1$	$1s^22s^2$	$^1S_0$	3091.95	9.81×10^{13}	4.28×10^{-1}
14+	$1s2s2p^2$	$^1S_0$	$1s^22s2p$	$^1P_1$	3090.93	5.29×10^{13}	1.79×10^{-1}
14+		$^1S_0$		$^3P_1$	3119.25	4.07×10^9	1.38×10^{-5}
14+		$^1P_1$		$^1P_1$	3088.82	1.51×10^{14}	7.19×10^{-1}
14+		$^1P_1$		$^3P_2$	3115.31	7.51×10^9	3.58×10^{-5}
14+		$^1P_1$		$^3P_1$	3117.15	7.90×10^9	3.76×10^{-5}
14+		$^1P_1$		$^3P_0$	3118.48	5.37×10^{10}	2.56×10^{-4}
14+		$^1D_2$		$^3P_2$	3102.36	3.10×10^{12}	1.42×10^{-2}
14+		$^1D_2$		$^3P_1$	3104.19	1.13×10^{11}	5.20×10^{-4}
14+		$^3S_1$		$^3P_2$	3097.40	3.15×10^{13}	2.99×10^{-1}
14+		$^3S_1$		$^3P_1$	3099.24	1.41×10^{13}	1.35×10^{-1}
14+		$^3S_1$		$^3P_0$	3100.57	3.73×10^{12}	3.55×10^{-2}
14+		$^3P^2_0$		$^3P_1$	3103.80	9.38×10^{12}	5.01×10^{-2}
14+		$^3P^1_1$		$^3P_0$	3085.8	7.82×10^{13}	3.89×10^{-1}
14+		$^3P^2_1$		$^3P_2$	3103.54	1.13×10^{13}	8.92×10^{-2}
14+		$^3P^2_1$		$^3P_1$	3105.37	1.65×10^{11}	1.30×10^{-3}
14+		$^3P^2_1$		$^3P_0$	3106.7	7.14×10^{11}	5.62×10^{-3}
14+		$^3P^1_2$		$^3P_1$	3087.37	4.59×10^{12}	2.08×10^{-2}
14+		$^3D_1$		$^3P_1$	3086.07	5.39×10^{13}	3.14×10^{-1}
14+		$^3D_1$		$^3P_0$	3087.4	1.38×10^{11}	8.02×10^{-4}

From Eqs. (8.22) and (8.23) the intensities of all the transitions presented in Table 8.2 were calculated. The line intensity is a function of the feeding mechanisms and thus of the ion densities in the ground configuration, $N_0^{q'}$, where q' is the ion charge state. From the extracted current of the ion beam of the SIMPA ECRIS we obtain a charge state distribution, which is the starting point for the spectrum simulation. The ion current values were taken from the PhD thesis of Adrouche [189] and are presented in Table 8.3. It is expected that the ion currents are not completely proportional to the ion densities inside the plasma because the ions are extracted from the plasma edges and the extraction system can be optimized for a particular charge state. The ion currents for a 300 W Ar plasma in the SIMPA ECRIS were normalized to the Ar^{16+} density obtained for another ECRIS by Douysset *et al.* [6] and later to the Ar^{16+} density obtained in this work. The ionic densities calculated from the ion current are also presented in Table 8.3. With this starting parameters it is possible to obtain iteratively the set of ion densities which result in the best fit of the wide scan data points from the simulated spectrum. A final χ^2_{red} of 9.33 was obtained and the resulting set

of ionic densities are also presented in Table 8.3 for comparison with the values from the ion current data. In Fig. 8.4, the ionic densities calculated in this work are compared to the

Table 8.3: Ion current and ionic densities of the SIMPA ECRIS Ar plasma. The ion currents were taken from Ref. [189].

Charge State	Ion Current (μA)	Ion Density (cm^{-3}) Adrouche [189]	Ion Density (cm^{-3}) This work	Ion Density (cm^{-3}) Douysset [6]
11+	22	7.59×10^{16}	8.0×10^{16}	1.5×10^{16}
12+	16	5.52×10^{16}	4.0×10^{16}	1.6×10^{16}
13+	7.5	2.59×10^{16}	2.0×10^{16}	7.5×10^{15}
14+	2.5	8.62×10^{15}	9.4×10^{15}	3.1×10^{15}
15+	0.4	1.38×10^{15}	2.0×10^{15}	1.4×10^{15}
16+	0.058	2.00×10^{14}	2.0×10^{14}	2.8×10^{14}

densities obtained from the extracted ion currents for a 300 W Ar plasma by Adrouche and to the densities obtained by Douysset *et al.* for a different ECR Ar plasma. As can be seen
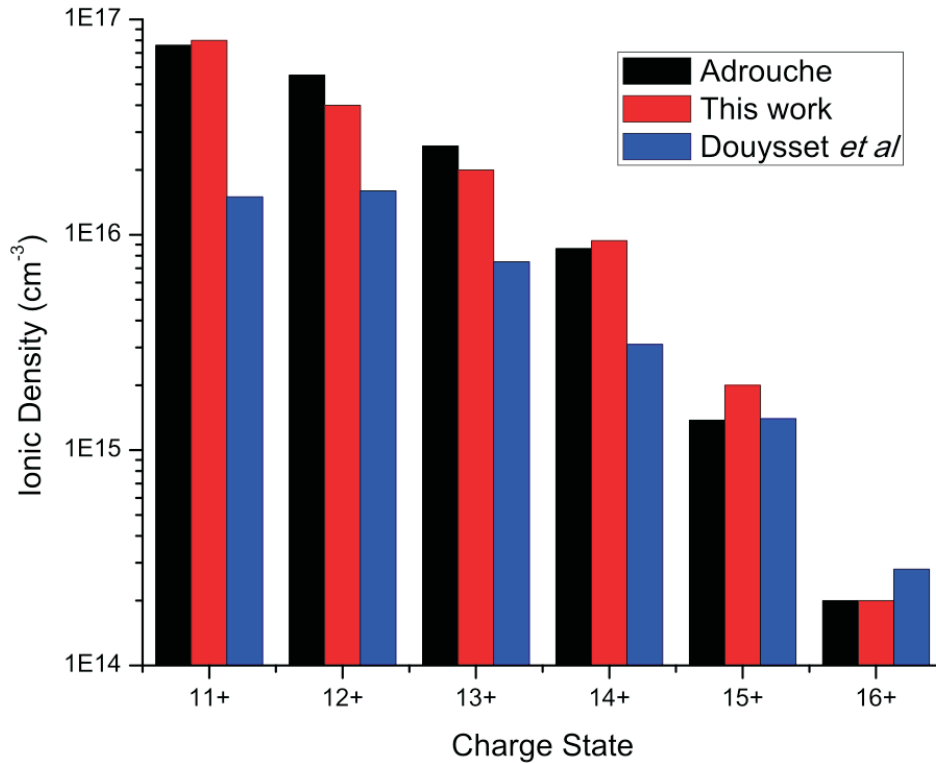

Figure 8.4: Charge state distribution of the Ar plasma. Densities obtained from the measured ion current, normalized to the He-like ion density from this work, are in black; Densities obtained in this work are in red; Densities obtained by Douysset for a different ECRIS are in blue.

in Fig. 8.4 there is a much better agreement between the CSD calculated from the extracted current and the CSD obtained in this work than with the CSD of Douysset *et al.*. The fact

that the CSD of Douysset *et al.* was measured for an Ar plasma with a different ECRIS and hence different experimental conditions, such as partial gas pressures and/or magnetic field strengths, is the probable cause for such a discrepancy. The greatest difference between the CSD calculated in this work and the one obtained from the extracted ion currents correspond to the Ar^{15+} ion, with a value of approximately 45%. For Ar^{12+} and Ar^{13+} the differences are around 30% and for Ar^{11+} and Ar^{14+} the differences are less than 10%. For applications in which the charge state distribution has to be known precisely, the CSD calculated from the extracted ion currents cannot be reliably used, albeit being a very good way to get a rough estimate.

Chapter 9

Conclusions

9.1 Conclusions

It has been shown that the double-crystal spectrometer, coupled to an electron-cyclotron-resonance ion-source can be used to perform very accurate, reference-free measurements which provide energies and widths, tied to the definition of the meter, for X-ray standard purposes. It is proven that the ECRIS has the necessary intensity to be used as a source of highly charged ion X-ray radiation for measurements with a DCS. The development of a temperature control system for both crystals lead to a 0.2 °C maximum variation of the surface temperature of the crystals, although a final temperature uncertainty of 0.5 °C has been used to account for low thermal contact and front-to-back temperature differences. This corresponds to a 0.0040 eV uncertainty or 1.29 ppm at 3.104 keV. We have measured the $1s2s\ ^3S_1 \rightarrow 1s^2\ ^1S_0$ relativistic $M1$ transition and found an energy of 3104.1605(78) eV (2.5 ppm accuracy). This value is the most accurate, reference-free measurement done for such a transition and is in good agreement with recent QED predictions. With this experiment we have established the first X-ray standard based on a narrow, symmetric line, that can be used to calibrate any instrument in this energy range to our quoted accuracy, without the problems associated with previous, X-ray tubes based standards. The use of a double-crystal spectrometer was made possible thanks to the very intense emission of the M1 transition from the ECRIS plasma, which is several orders of magnitude stronger than what can be obtained from an electron-beam ion-trap or from other highly charged ions production devices. Such high precision measurements can also enable direct tests of the QED theory in medium Z elements and can provide new X-ray standards based on narrow transitions of highly charged ions.

With the use of such a narrow line as the relativistic $M1$ we were able to probe the instrument response function as well as calculate the Doppler broadening of the ions inside the plasma which we found to be 80.5(4.6) meV. From this information we were also able to extract such parameters as the ionic temperature of the plasma and electronic densities, which were in accordance with the latest measurements done at the SIMPA ECRIS [131, 189]. We have also measured indirectly the natural width of the diagram line $1s2p\ ^1P_1 \rightarrow 1s^2\ ^1S_0$ in He-like Ar, and the obtained value of 79.08(10.40) meV is consistent with the theoretical value of 70.4 meV.

From a wide scan containing several features from He-like to Be-like Ar ions we calculated the charge state distribution of these ions inside the ECRIS plasma and compared them to the ratios of extracted ion currents. The plasma diagnosis tool has proven to be an excellent method of inferring the charge state information from the radiation emitted from the ECRIS plasma.

With this ECRIS-DCS system we can now investigate core-excited ions with 3 and 4 electrons to study correlation and Auger shifts. Thanks to the well understood line shape

of the double-crystal spectrometer, it will be possible to obtain the intrinsic width of these transitions to a few percent accuracy. This will allow the study of radiative and Auger contributions to the transition probability. In the future, with the use of higher performance ECRIS (larger plasma and higher electronic densities), improvements in the temperature controls and angle measurements accuracy of the double-crystal spectrometer [204], it will be possible to obtain X-ray energies accuracy below 1 ppm and to perform measurements on heavier elements.

Bibliography

[1] Friedlein R, Herpich S, Lehnert U, Tyrroff H, Wirth H, Zippe C and Zschornack G 1995 *Nuclear Instruments and Methods in Physics Research Section B: Beam Interactions with Materials and Atoms* **98** 585–588

[2] Lehnert U, Zippe C and Zschornack G 1996 *Hyperfine Interactions* **99** 235–241

[3] Heinzelmann C, Lehnert U, Kchler D and Zschornack G 1997 *Hyperfine Interactions* **108** 51–58

[4] Grubling P, Kuchler D, Lehnert U, Ullrich A, Werner T and Zschornack G 1998 *Review of Scientific Instruments* **69** 1167–1169

[5] John B B, Chun C L and A D Charles J 2004 *Journal of Physics D: Applied Physics* **37** R143

[6] Douysset G, Khodja H, Girard A and Briand J P 2000 *Physical Review E* **61** 3015–3022

[7] Kchler D, Ullmann F, Werner T, Zschornack G, Tyrroff H and Grbling P 2000 *Nuclear Instruments and Methods in Physics Research Section B: Beam Interactions with Materials and Atoms* **168** 566–577

[8] Martins M C, Costa A M, Santos J P, Indelicato P and Parente F 2001 *Journal of Physics B: Atomic, Molecular and Optical Physics* **34** 533

[9] Santos J P, Costa A M, Marques J P, Martins M C, Indelicato P and Parente F 2010 *Physical Review A* **82** 062516

[10] Kim Y K and Rudd M E 1994 *Physical Review A* **50** 3954–3967

[11] Bethe H 1930 *Annalen der Physik* **5** 325–400

[12] Kim Y K and Desclaux J P 2002 *Physical Review A* **66** 012708

[13] Kim Y K and Stone P M 2001 *Physical Review A* **64** 052707

[14] Kim Y K, Santos J P and Parente F 2000 *Physical Review A* **62** 052710

[15] Santos J P and et al 2003 *Journal of Physics B: Atomic, Molecular and Optical Physics* **36** 4211

[16] Davis B 1918 *Physical Review* **11** 433

[17] Rossland G 1923 *Phil. Mag.* **45**

[18] Thomas L H 1927 *Proceedings of the Cambridge Philosophical Society* **23** 829–831

[19] Bethe H 1932 *Zeitschrift fuer Physik* **76** 293–299

[20] Webster D L, Hansen W W and Duveneck F B 1933 *Physical Review* **43** 839

[21] Gryzinacuteski M 1959 *Physical Review* **115** 374

[22] Vriens L 1964 *Physics Letters* **10** 170–171

[23] Vriens L 1964 *Physics Letters* **9** 295–296

[24] Vriens L 1966 *Physical Review* **141** 88

[25] Kolbenstvedt H 1967 *Physical Review* **163** 112

[26] Lotz W 1968 *Zeitschrift Fur Physik* **216** 241–247

[27] Rudge M R H 1968 *Reviews of Modern Physics* **40** 564

[28] Inokuti M 1971 *Review of Modern Physics* **43** 297–347

[29] Bray I 1995 *Journal of Physics B: Atomic, Molecular and Optical Physics* **28** L247

[30] Bray I, Stelbovics A T, Benjamin B and Herbert W 1995 Calculation of electron scattering on hydrogenic targets *Advances In Atomic, Molecular, and Optical Physics* vol Volume 35 (Academic Press) pp 209–254 doi: DOI: 10.1016/S1049-250X(08)60164-0

[31] Bartschat K, Hudson E T, Scott M P, Burke P G and Burke V M 1996 *Physical Review A* **54** R998–R1001

[32] Baertschy M, Rescigno T N, Isaacs W A, Li X and McCurdy C W 2001 *Physical Review A* **63** 022712

[33] Segui S, Dingfelder M and Salvat F 2003 *Physical Review A* **67** 062710

[34] Riahi A and et al 2001 *Journal of Physics B: Atomic, Molecular and Optical Physics* **34** 175

[35] Patoary M A R, Uddin M A, Haque A K F, Shahjahan M, Basak A K, Talukder M R and Saha B C 2009 *Int. J. Quantum Chem.* **109** 897–906

[36] Bote D, Salvat F, Jablonski A and Powell C J 2009 *Atomic Data and Nuclear Data Tables* **95** 871–909

[37] Haque A K F and et al 2010 *Journal of Physics B: Atomic, Molecular and Optical Physics* **43** 115201

[38] Deutsch H and Mrk T D 1987 *Int. J. Mass Spectrom. Ion Process.* **79** R1–R8

[39] Uddin M A and et al 2004 *Journal of Physics B: Atomic, Molecular and Optical Physics* **37** 1909

[40] Landau L D and Lifshitz E M 1958 *Quantum Mechanics, Non-Relativistic Theory* (Oxford: Pergamon Press)

[41] Born M and Oppenheimer R 1927 *Annalen der Physik* **389** 457–484

[42] Mott N F 1930 *Proc. Roy. Soc. A* **126** 8

[43] Mott N F and Masey H S 1949 *The Theory of Atomic Collisions* (London: Oxford University Press)

[44] Wigner E P 1946 *Physical Review* **70** 606–618

[45] Wigner E P 1946 *Physical Review* **70** 15–33

[46] Burke P G 2011 *R-Matrix Theory of Atomic Collisions Application to Atomic, Molecular and Optical Processes (Springer Series on Atomic, Optical, and Plasma Physics vol 72)* (Springer)

[47] Vriens L 1969 Case studies in atomic physics vol 1 ed McDowell E W M and C M R p 335

[48] Wilson W E 1972 *Radiation Research* **49** 36–50

[49] Kim Y K 1972 *Physical Review A* **6** 666–670

[50] Desclaux J P 1975 *Computer Physics Communications* **9** 31–45

[51] Indelicato P and Desclaux J P 1990 *Physical Review A* **42** 5139

[52] Charlotte F F 1991 *Computer Physics Communications* **64** 431–454

[53] Kim Y K, Irikura K K and Ali M A 2000 *J. Res. Natl. Inst. Stand. Technol.* **105** 285–291

[54] J Santos P and Parente F 2008 *Eur. Phys. J. D* **47** 339–350

[55] Gryziski M 1965 *Physical Review* **138** A305–A321

[56] Gryziski M 1965 *Physical Review* **138** A322–A335

[57] Gryziski M 1965 *Physical Review* **138** A336–A358

[58] Quarles C A 1976 *Physical Review A* **13** 1278–1280

[59] Deutsch H, Becker K and Mrk T D 1995 *Int. J. Mass Spectrom. Ion Process.* **151** 207–217

[60] Scofield J H 1978 *Physical Review A* **18** 963

[61] Shah M B, Elliott D S and Gilbody H B 1987 *Journal of Physics B: Atomic and Molecular Physics* **20** 3501

[62] Shah M B, Elliott D S, McCallion P and Gilbody H B 1988 *J. Phys. B-At. Mol. Opt. Phys.* **21** 2751–2761

[63] Nagy P and et al 1980 *Journal of Physics B: Atomic and Molecular Physics* **13** 1249

[64] Rejoub R, Lindsay B G and Stebbings R F 2002 *Physical Review A* **65** 042713

[65] Kim Y K 2001 *Physical Review A* **64** 032713

[66] Younger S M 1981 *J. Quant. Spectrosc. Radiat. Transf.* **26** 329–337

[67] Burgess A 1964 Proceedings of the third international conference on electronic and atomic collisions *Proceedings of the Third International Conference on electronic and atomic Collisions, London* ed McDowell M R C

[68] Burgess A 1964 *Proceedings of the Symposium on Atomic Collision Processes in Plasmas, Culham*

[69] Indelicato P 1995 *Physical Review A* **51** 1132

[70] Grant I P, Quiney H M, David B and Benjamin B 1988 Foundations of the relativistic theory of atomic and molecular structure *Advances in Atomic and Molecular Physics* vol Volume 23 (Academic Press) pp 37–86 doi: DOI: 10.1016/S0065-2199(08)60105-0

[71] Casnati E and et al 1982 *Journal of Physics B: Atomic and Molecular Physics* **15** 155

[72] Guerra M, Parente F, Indelicato P and Santos J P 2012 *International Journal of Mass Spectrometry* **313** 1–7

[73] Deslattes R D, Kessler E G, Indelicato P, de Billy L, Lindroth E and Anton J 2003 *Reviews of Modern Physics* **75** 35–99

[74] Bruch R, Luken W L, Culberson J C and Chung K T 1985 *Physical Review A* **31** 503

[75] Hombourger C 1998 *Journal of Physics B: Atomic, Molecular and Optical Physics* **31** 3693

[76] Egerton R F 1975 *Philosophical Magazine* **31** 199–215

[77] Tawara H, Harrison K G and Heer F J D 1973 *Physica* **63** 351–367

[78] Hink W and Paschke H 1971 *Physical Review A* **4** 507

[79] Isaacson M 1972 *J. Chem. Phys.* **56** 1803–1812

[80] Glupe G and Mehlhorn W 1971 *Journal de Physique* **C4** 40

[81] Platten H, Schiwietz G and Nolte G 1985 *Physics Letters* **107A** 89

[82] Ishii K, Kamiya M, Sera K, Morita S, Tawara H, Oyamada M and Chu T C 1977 *Physical Review A* **15** 906

[83] Kamiya M, Kuwako A, Ishii K, Morita S and Oyamada M 1980 *Physical Review A* **22** 413

[84] Hoffmann D H H, Genz H, Lw W and Richter A 1978 *Physics Letters A* **65** 304–306

[85] Shchagin A V, Pristupa V I and Khizhnyak N A 1994 *Nucl. Instrum. Methods Phys. Res. Sect. B-Beam Interact. Mater. Atoms* **84** 9–13

[86] He F Q, Peng X F, Long X G, Luo Z M and An Z 1997 *Nucl. Instrum. Methods Phys. Res. Sect. B-Beam Interact. Mater. Atoms* **129** 445–450

[87] Jessenberger J and Hink W 1975 *Z. Phys. A.-Hadrons Nuclei* **275** 331–337

[88] An Z, Tang C H, Zhou C G and Luo Z M 2000 *J. Phys. B-At. Mol. Opt. Phys.* **33** 3677–3684

[89] Llovet X, Merlet C and Salvat F 2000 *J. Phys. B-At. Mol. Opt. Phys.* **33** 3761–3772

[90] Luo Z M, An Z, He F Q, Li T H, Long X G and Peng X F 1996 *J. Phys. B-At. Mol. Opt. Phys.* **29** 4001–4005

[91] Luo Z M, An Z, Li T H, Wang L M, Zhu Q and Xia X Y 1997 *J. Phys. B-At. Mol. Opt. Phys.* **30** 2681–2686

[92] Scholz W, Li-Scholz A, Coll, eacute, R and Preiss I L 1972 *Physical Review Letters* **29** 761

[93] Tang G H, Luo Z M, An Z and Li T H 1999 *Chin. Phys. Lett.* **16** 505–507

[94] An Z, Li T H, Wang L M, Xia X Y and Luo Z M 1996 *Physical Review A* **54** 3067

[95] Shevelko V P, Solomon A M and Vukstich V S 1991 *Phys. Scr.* **43** 158–161

[96] Middleman L M, Ford R L and Hofstadter R 1970 *Physical Review A* **2** 1429

[97] Davis D V, Mistry V D and Quarles C A 1972 *Physics Letters A* **38** 169

[98] Schneider H, Tobehn I, Ebel F and Hippler R 1993 *Physical Review Letters* **71** 2707

[99] Shima K, Nakagawa T, Umetani K and Mikumo T 1981 *Physical Review A* **24** 72

[100] Rester D H and Dance W E 1966 *Physical Review* **152** 1

[101] Kiss K, Kalman G, Palinkas J and Schlenk B 1981 *Acta Physica Academiae Scientiarum Hungaricae* **50** 97–102

[102] Schlenk B, Berenyi D, Ricz S, Valek A and Hock G 1976 *Acta Physica Academiae Scientiarum Hungaricae* **41** 159–163

[103] SeifelnaSa, Berenyi D and Bibok G 1974 *Zeitschrift Fur Physik* **267** 169–174

[104] Hubner H, Hoffmann K W and Ilgen K 1972 *Zeitschrift Fur Physik* **255** 269–280

[105] Ricz S, Schlenk B, Berenyi D, Hock G and Valek A 1977 *Acta Physica Academiae Scientiarum Hungaricae* **42** 269–271

[106] Lotz W 1970 *Zeitschrift fr Physik A Hadrons and Nuclei* **232** 101–107

[107] Hippler R, McGregor I, Aydinol M and Kleinpoppen H 1981 *Physical Review A* **23** 1730

[108] Hoffmann D H H, Brendel C, Genz H, Low W, Muller S and Ritcher A 1979 *Zeitschrift fuer Physik A: Atoms and Nuclei* **293** 187

[109] Krishnakumar E and Srivastava S K 1988 *Journal of Physics B: Atomic, Molecular and Optical Physics* **21** 1055

[110] Syage J A 1992 *Physical Review A* **46** 5666

[111] Schram B L 1966 *Physica* **32** 197–208

[112] Tinschert K and et al 1987 *Journal of Physics B: Atomic and Molecular Physics* **20** 1121

[113] Bannister M E, Guo X Q and Kojima T M 1994 *Physical Review A* **49** 4676

[114] Bannister M E, Mueller D W, Wang L J, Pindzola M S, Griffin D C and Gregory D C 1988 *Physical Review A* **38** 38

[115] Oualim E M, Duponchelle M and Defrance P 1995 *Nuclear Instruments and Methods in Physics Research Section B: Beam Interactions with Materials and Atoms* **98** 150–153

[116] Khouilid M and et al 2001 *Journal of Physics B: Atomic, Molecular and Optical Physics* **34** 1727

[117] Loch S D, Pindzola M S, Ballance C P, Griffin D C, Mitnik D M, Badnell N R, O'Mullane M G, Summers H P and Whiteford A D 2002 *Physical Review A* **66** 052708

[118] Beigman I, Defrance P and Vainshtein L 2003 *Nuclear Instruments and Methods in Physics Research Section B: Beam Interactions with Materials and Atoms* **205** 427–432

[119] Chen M H and Reed K J 1993 *Physical Review A* **47** 1874

[120] Badnell N R and Pindzola M S 1993 *Physical Review A* **47** 2937

[121] Gorczyca T W, Pindzola M S, Badnell N R and Griffin D C 1994 *Physical Review A* **49** 4682–4692

[122] Martins M C, Marques J P, Costa A M, Santos J P, Parente F, Schlesser S, Bigot E O L and Indelicato P 2009 *Physical Review A* **80** 032501

[123] Essoltani A, Proulx P, Boulos M I and Gleizes A 1990 *Journal of Analytical Atomic Spectrometry* **5**

[124] Menart J and Malik S 2002 *Journal of Physics D: Applied Physics* **35** 867

[125] Whiteford A D, Badnell N R, Ballance C P, Loch S D, OMullane M G and Summers H P 2002 *Journal of Physics B: Atomic, Molecular and Optical Physics* **35** 3729

[126] Golden L B and Sampson D H 1978 *The Astrophysical Journal Supplement Series* **38** 19–28

[127] Archer B J, Clark R E H, Fontes C J and Zhang H Gipper URL http://aphysics2.lanl.gov/cgi-bin/ION/runlanl08d.pl

[128] Peek J M and Mann J B 1977 *Physical Review A* **16** 2315

[129] Rodrigues G C, Indelicato P, Santos J P, Patt P and Parente F 2004 *Atomic Data and Nuclear Data Tables* **86** 117–233

[130] Man K F and et al 1987 *Journal of Physics B: Atomic and Molecular Physics* **20** 5865

[131] Gumberidze A, Trassinelli M, Adrouche N, Szabo C I, Indelicato P, Haranger F, Isac J M, Lamour E, Bigot E O L, Merot J, Prigent C, Rozet J P and Vernhet D 2010 *Review of Scientific Instruments* **81** 033303–10

[132] Biri S, Simons L and Hitz D 2000 *Review of Scientific Instruments* **71** 1116–1118

[133] Pras R, Lamoureux M, Girard A, Khodja H and Melin G 1998 *Review of Scientific Instruments* **69** 700–702

[134] Gaudin C, Hay L, Buzzi J M, Bacal M and Lamoureux M 1998 *Review of Scientific Instruments* **69** 890–892

[135] Leitner D, Benitez J Y, Lyneis C M, Todd D S, Ropponen T, Ropponen J, Koivisto H and Gammino S 2008 *Review of Scientific Instruments* **79** 033302–6

[136] Bacal M, Gaudin C, Bourdier A, Bruneteau J, Buzzi J M, Golovanivsky K S, Hay L, Rouille C and Schwartz L 1996 *Nature* **384** 421–421

[137] Barue C, Lamoureux M, Briand P, Girard A and Melin G 1994 *Journal of Applied Physics* **76** 2662–2670

[138] Niering M, Holzwarth R, Reichert J, Pokasov P, Udem T, Weitz M, Hnsch T W, Lemonde P, Santarelli G, Abgrall M, Laurent P, Salomon C and Clairon A 2000 *Physical Review Letters* **84** 5496–5499

[139] d Beauvoir B, Schwob C, Acef O, Jozefowski L, Hilico L, Nez F, Julien L, Clairon A and Biraben F 2000 *Eur. Phys. J. D* **12** 61–93

[140] Kandula D Z, Gohle C, Pinkert T J, Ubachs W and Eikema K S E *Physical Review Letters* **105** 063001

[141] Borbely J S, George M C, Lombardi L D, Weel M, Fitzakerley D W and Hessels E A 2009 *Physical Review A* **79** 060503

[142] Smiciklas M and Shiner D *Physical Review Letters* **105** 123001

[143] Pachucki K and Yerokhin V A *Physical Review Letters* **104** 070403

[144] Pohl R, Antognini A, o Nez F, Amaro F D, o Biraben F, o M R Cardoso J, Covita D S, Dax A, Dhawan S, Fernandes L M P, Giesen A, Graf T, Hnsch T W, Indelicato P, Julien L, Kao C Y, Knowles P, Bigot E O L, Liu Y W, Lopes J A M, Ludhova L, Monteiro C M B, o Mulhauser F, Nebel T, Rabinowitz P, dos Santos J M F, Schaller L A, Schuhmann K, Schwob C, Taqqu D, o F C A Veloso J and Kottmann F *Nature* **466** 213–216

[145] Mohr P J, Taylor B N and Newell D B 2008 *Reviews of Modern Physics* **80** 633–730

[146] Brandau C, Kozhuharov C, Mller A, Shi W, Schippers S, Bartsch T, Bhm S, Bhme C, Hoffknecht A, Knopp H, Grn N, Scheid W, Steih T, Bosch F, Franzke B, Mokler P H, Nolden F, Steck M, Sthlker T and Stachura Z 2003 *Physical Review Letters* **91** 073202

[147] Beiersdorfer P, Chen H, Thorn D B and Trbert E 2005 *Physical Review Letters* **95** 233003

[148] Beiersdorfer P *Journal of Physics B: Atomic, Molecular and Optical Physics* **43** 074032

[149] DeVore T R, Crosby D N and Myers E G 2008 *Physical Review Letters* **100** 243001

[150] Trassinelli M, Kumar A, H Beyer F, Indelicato P, Mrtin R, Reuschl R, Y Kozhedub S, Brandau C, Bruning H, Geyer S, Gumberidze A, Hess S, Jagodzinski P, Kozhuharov C, Liesen D, Spillmann U, Trotsenko S, Weber G, D Winterseak F A and Sthlker T 2009 *EPL* **87** 63001

[151] Gumberidze A, Sthlker T, Bana D, Beckert K, Beller P, Beyer H F, Bosch F, Hagmann S, Kozhuharov C, Liesen D, Nolden F, Ma X, Mokler P H, Steck M, Sierpowski D and Tashenov S 2005 *Physical Review Letters* **94** 223001

[152] Fritzsche S, Indelicato P and h Th S 2005 *Journal of Physics B: Atomic, Molecular and Optical Physics* **38** S707

[153] n Plunien G, Mller B, Greiner W and Soff G 1991 *Physical Review A* **43** 5853–5866

[154] Bruhns H, Braun J, Kubiek K, Lpez-Urrutia J R C and Ullrich J 2007 *Physical Review Letters* **99** 113001

[155] Chantler C T, Paterson D, Hudson L T, Serpa F G, Gillaspy J D and Takcs E 2000 *Physical Review A* **62** 042501

[156] Anagnostopoulos D F, Gotta D, Indelicato P and Simons L M 2003 *Physical Review Letters* **91** 240801

[157] Amaro P 2011 *Study of Forbidden Transitions in Atomic Systems* Ph.D. thesis New University of Lisbon and University Pierre and Marie Currie

Bibliography

[158] Consolino J, Geller R and Lerot C 1969 *Proc. 1st Int'l. Conf. on Ion Sources* (Saclay)

[159] Postma H 1970 *Physics Letters A* **31** 196–197

[160] Apard P, Bliman S, Geller R, Jacquot B and Jacquot C 1971 *Ptoc. 2nd Int'l. Conf. on Ion Sources* (Wien)

[161] Melin G, Bourg F, Briand P, Delaunay M, Gaudart G, Girard A, Hitz D, Klein J P, Ludwig P, Nguyen T K, Pontonnier M and Su Y 1994 *Review of Scientific Instruments* **65** 1051–1056

[162] Drentje A G 1994 *Review of Scientific Instruments* **65** 1045–1050

[163] Lyneis C M and Antaya T A 1990 *Review of Scientific Instruments* **61** 221–224

[164] Geller R 1990 *Annual Review of Nuclear and Particle Science* **40** 15–44

[165] Bieth C, Bouly J L, Curdy J C, Kantas S, Sortais P, Sole P and Vieux-Rochaz J L 2000 *Review of Scientific Instruments* **71** 899–901

[166] Beyer H F, Beyer H F, Kluge H J and Shevelko V P 1997 *X-ray radiation of highly charged ions* (Springer)

[167] Arianer J and Geller R 1981 *Annual Review of Nuclear and Particle Science* **31** 19–51

[168] Leitner D, Lyneis C M, Abbott S R, Collins D, Dwinell R D, Galloway M L, Leitner M and Todd D S 2005 *Nuclear Instruments and Methods in Physics Research Section B: Beam Interactions with Materials and Atoms* **235** 486–493

[169] Ludwig P, Bourg F, Briand P, Girard A, Melin G, Guillaume D, Seyfert P, Grassa A L, Ciavola G, Gammino S, Castro M, Chines F and Marletta S 1998 *Review of Scientific Instruments* **69** 4082–4085

[170] Gammino S, Ciavola G, Celona L, Hitz D, Girard A and Melin G 2001 *Review of Scientific Instruments* **72** 4090–4097

[171] Biri S, Simons L and Hitz D 2000 *Review of Scientific Instruments* **71** 1116–1118

[172] Hutchinson I H 2002 *Plasma Physics and Controlled Fusion* **44** 2603

[173] Schlesser S 2009 *Spectroscopie X dions trs chargs et niveaux dnergie de lhydrogne pionique* Ph.D. thesis Universite Pierre et Marie Curie (Paris VI)

[174] Kessler E G, Henins A, Nielsen L, Deslattes R D and Arif M 1994 *J. Res. Natl. Inst. Stand. Technol.* **99**

[175] d Rio M S and Dejus R J 2004 *SPIE* pp 171–174

[176] Ziegler J G and Nichols N B 1942 *Transactions of the ASME.* **64** 10

[177] Lindroth E and Salomonson S 1990 *Physical Review A* **41** 4659–4669

[178] Indelicato P 1996 *Physical Review Letters* **77** 3323–3326

[179] Stepanov S URL http://sergey.gmca.aps.anl.gov/x0h.html

[180] Lugovskaya O M and Stepanov S A 1991 *Soviet physics Crystallography* **36**

[181] Henke B L, Gullikson E M and Davis J C 1993 *Atomic Data and Nuclear Data Tables* **54** 181–342

[182] Artemyev A N, Shabaev V M, Yerokhin V A, Plunien G and Soff G 2005 *Physical Review A* **71** 062104

[183] Indelicato P, Gorveix O and Desclaux J P 1987 *Journal of Physics B: Atomic and Molecular Physics* **20** 651

[184] Indelicato P 1988 *Nuclear Instruments and Methods in Physics Research Section B: Beam Interactions with Materials and Atoms* **31** 14–20

[185] Indelicato P 1993

[186] Drake G W F 1988 *Nuclear Instruments and Methods in Physics Research Section B: Beam Interactions with Materials and Atoms* **31** 7–13

[187] Plante D R, Johnson W R and Sapirstein J 1994 *Physical Review A* **49** 3519–3530

[188] Breit G and Wigner E 1936 *Physical Review* **49** 519–531

[189] Adrouche N 2006 *Diagnostic du plasma de la source dions ECR SIMPA par spectroscopie X* Ph.D. thesis UNIVERSITE PARIS VI PIERRE ET MARIE CURIE

[190] Costa A M, Martins M C, Parente F, Santos J P and Indelicato P 2001 *Atomic Data and Nuclear Data Tables* **79** 223–239

[191] Christine M C 1985 *Nuclear Fusion* **25** 35

[192] Dory R A, Guest G E and Harris E G 1965 *Physical Review Letters* **14** 131–133

[193] Shevelko V P and Tawara H 1995 *Journal of Physics B: Atomic, Molecular and Optical Physics* **28** L589

[194] Blenger C, Defrance P, Salzborn E, Shevelko V P, Tawara H and Uskov D B 1997 *Journal of Physics B: Atomic, Molecular and Optical Physics* **30** 2667

[195] Plasma laboratory of weizmann institute of science, databases for atomic and plasma physics URL http://plasma-gate.weizmann.ac.il/DBfAPP.html

[196] Kim Y K, Irikura K K, Rudd M E, Ali M A and Stone P M Electron-impact cross sections for ionization and excitation URL http://physics.nist.gov/ionxsec

[197] Fisher V, Bernshtam V, Golten H and Maron Y 1996 *Physical Review A* **53** 2425–2432

[198] v Regemorter H 1962 *Astrophys. J.* **136**

[199] Sampson D H and Zhang H L 1992 *Physical Review A* **45** 1556–1561

[200] Cowan R D 1967 *Physical Review* **163** 54–61

[201] Indelicato P 1997 *Hyperfine Interactions* **108** 39–49

[202] Lwdin P O 1955 *Physical Review* **97** 1474–1489

[203] Santos J P, Marques J P, Parente F, Lindroth E, Indelicato P and Desclaux J P 1999 *Journal of Physics B: Atomic, Molecular and Optical Physics* **32** 2089

[204] Estler W T 1998 *J. Res. Natl. Inst. Stand. Technol.* **103**